HYDRODYNAMIC DISPERSION IN CAPILLARY FLOW OF MAGNETIC FLUIDS

Yuri Zeniti Sinzato

Master's dissertation
Mechanical Sciences

UNIVERSITY OF BRASILIA

Faculty of Technology
Department of Mechanical Engineering

UNIVERSITY OF BRASILIA
FACULTY OF TECHNOLOGY
DEPARTMENT OF MECHANICAL ENGINEERING

HYDRODYNAMIC DISPERSION IN CAPILLARY FLOW OF MAGNETIC FLUIDS

Yuri Zeniti Sinzato

Advisor: Francisco Ricardo da Cunha, Prof. Univ (ENM/ UnB)

MASTER'S DISSERTATION

PUBLICATION NUMBER: ENM.DM -

BRASÍLIA/DF: February 9, 2021

UNIVERSITY OF BRASILIA
FACULTY OF TECHNOLOGY
DEPARTMENT OF MECHANICAL ENGINEERING

Hydrodynamic Dispersion in Capillary Flow of Magnetic Fluids

Yuri Zeniti Sinzato

REPORT SUBMITTED TO THE DEPARTMENT OF MECHANICAL ENGINEERING OF THE FACULTY OF TECHNOLOGY OF THE UNIVERSITY OF BRASILIA AS A PARTIAL REQUIREMENT FOR OBTAINING THE DEGREE OF MASTER IN MECHANICAL SCIENCES.

APPROVED BY:

Francisco Ricardo da Cunha, Prof. Univ (ENM/ UnB)
(Advisor)

Adriano Possebon Rosa, Prof. Univ (ENM/ UnB)
(Internal Examiner)

Roney Leon Thompson, Prof. Univ (UFRJ)
(External Examiner)

André von Borries Lopes, Prof. Univ (ENM/ UnB)
(Surrogate Examiner)

BRASÍLIA/DF, FEBRUARY 9, 2021.

FICHA CATALOGRÁFICA

Sinzato, Y. Z.
Hydrodynamic Dispersion in Capillary Flow of Magnetic Fluids
[Distrito Federal] 2020.
xvii, 99p. (ENM/FT/UnB, Mestrado, Ciências Mecânicas, 2020.
Dissertação de Mestrado - Universidade de Brasília.
Faculdade de Tecnologia.
Departamento de Engenharia Mecânica.
Palavras-chave:
1. Ferrofluido 2. Dispersão hidrodinâmica
3. Escoamento em capilar 4. Efeito magnetovicoso
I. ENM/FT/UnB II. Título (série)

REFERÊNCIA BIBLIOGRÁFICA

Sinzato, Y. Z.(2020). Hydrodynamic Dispersion in Capillary Flow of Magnetic Fluids. Dissertação de mestrado, Publicação ENM.DM - , Departamento de Engenharia Mecânica, Universidade de Brasília, Brasília, Distrito Federal, xvii, 99p.

CESSÃO DE DIREITOS

NOME DO AUTOR: Yuri Zeniti Sinzato.

TÍTULO DA DISSERTAÇÃO DE MESTRADO: Hydrodynamic Dispersion in Capillary Flow of Magnetic Fluids.

GRAU / ANO: MESTRADO / 2020

Yuri Zeniti Sinzato

Agradecimentos

Agradeço primeiramente aos meus pais, Antonia e Florencio, pelo exemplo, carinho, educação e por apoiarem a minha formação.

Agradeço a minha namorada Bruna pela companhia, ajuda e atenção proporcionada nestes anos.

Agradeço ao meu orientador prof. Francisco que me acolheu desde o início do curso na pesquisa acadêmica e me orientou para desenvolver trabalhos com seriedade e qualidade.

Agradeço aos professores do departamento de engenharia mecânica pelo conhecimento transmitido.

Agradeço aos amigos do grupo com que dividi momentos de aprendizado e descontração: Filipe, Gesse, Victor, Marcos e, em especial, ao Igor, que me auxiliou nos resultados experimentais.

Resumo

Dispersão Hidrodinâmica em Escoamento Capilar de Fluidos Magnéticos

Autor: Yuri Zeniti Sinzato

Orientador: Francisco Ricardo da Cunha, Prof. Univ (ENM/ UnB)

Programa de Pós Graduação em Ciências Mecânicas

Brasília, Dezembro de 2020

O presente trabalho apresenta uma investigação teórica e experimental da influência do dispersão hidrodinâmica na reologia de suspensões magnéticas. Uma geometria capilar é considerada, na qual um ferrofluido diluído escoa sob a ação de um campo magnético longitudinal. Assume-se que a dispersão hidrodinâmica é originada na rugosidade ou não-esfericidade das partículas. Um nova solução assintótica é calculada para o regime de escoamentos fracos. Os resultados numéricos indicam que o fluxo dispersivo por gradiente de taxa de cisalhamento produz uma migração de partículas em direção ao centro do tubo. No caso de partículas lisas elipsoidais, dois claros regimes são identificados de acordo com os parâmetros adimensionais. Os resultados teóricos trazem esclarecimentos sobre a reologia de ferrofluidos em escoamentos quadráticos, especialmente sobre suspensões destinadas a aplicações biomédicas. Os resultados experimentais, embora não sejam conclusivos quanto à influência da dispersão hidrodinâmica, mostram que a formação e quebra de agregados é determinante para o efeito magnetoviscoso de ferrofluidos comerciais.

Palavras-chaves: Ferrofluido; Dispersão hidrodinâmica; Escoamento em capilar; Efeito magnetovicoso.

Abstract

Hydrodynamic Dispersion in Capillary Flow of Magnetic Fluids

Author: Yuri Zeniti Sinzato

Advisor: Francisco Ricardo da Cunha, Prof. Univ (ENM/ UnB)

Master in Mechanical Sciences

Brasília, December 2020

The present work performs a theoretical and experimental investigation of the influence of a shear-induced dispersion on the rheological response of a magnetic suspension. A capillary geometry is considered, in which a dilute ferrofluid flows under the action of a longitudinal applied magnetic field. The shear-induced dispersion is assumed to be originated either on the particle's rugosity or non-sphericity. A new asymptotic solution for the limit of weak flows is presented. The numerical results indicate that the dispersive flux by shear rate gradient produces a particle migration towards the center of the tube. In the case of smooth ellipsoidal particles, two clear regimes can be identified according to the non-dimensional physical parameters. The theoretical results provide useful insights into the rheology of ferrofluids in quadratic flows, especially to suspensions designed for biomedical applications. The experimental measurements, although they are not conclusive to the influence of the hydrodynamic dispersion, indicate that the formation and break-up of chains largely affect the magnetoviscous effect of commercial ferrofluids.

Key-words: Ferrofluid, hydrodynamic dispersion, capillary flow, magnetoviscous effect.

Summary

List of Figures

List of Tables

List of Abbreviations and Acronyms

FHD	Ferrohydrodynamics
MHD	Magnetohydrodynamics
MRF	Magnetorheological fluid
MVE	Magnetoviscous effect

List of Symbols

Greek symbols:

α	Local Langevin parameter
α_e	Effective local Langevin parameter
α_o	Global Langevin parameter
β	Aspect ratio
$\dot{\gamma}$	Shear rate
$\dot{\gamma}_c$	Poiseuille wall shear rate
$\dot{\gamma}_w$	Wall shear rate
δ	Uncertainty
ε	Particle rugosity
$\boldsymbol{\epsilon}$	Levi-Civita tensor
η	Dynamic viscosity
η_o	Carrier fluid viscosity
η_ϕ	Einstein's viscosity
η_r	Relative viscosity
η_w	Wall viscosity
θ	Angle
λ	Magnetic dipole interaction parameter
μ_o	Vacuum magnetic permeability
ξ	Vorticity
ρ	Density
$\boldsymbol{\sigma}$	Stress tensor
τ	Relaxation time
τ_b	Brownian rotational time
τ_n	Néel relaxation time
ν	Geometric function

ϕ_h	Hydrodynamic volume fraction
ϕ_m	Magnetic volume fraction
χ	Magnetic susceptibility
χ_e	Effective magnetic susceptibility
χ_i	Initial magnetic susceptibility
ψ_i	Geometric functions
Ω	Angular velocity

Latin symbols:

a_h	Sphere's radius or ellipsoid's minor axis (hydrodynamic volume)
a_m	Sphere's radius or ellipsoid's minor axis (magnetic core)
b_h	Ellipsoid's major axis (hydrodynamic volume)
b_m	Ellipsoid's major axis (magnetic core)
$\boldsymbol{B}$	Flux density vector
C_h, C_m	Asymptotic solution parameters
d	Capillary diameter
D_r	Rotational Brownian diffusivity
D_t	Translational Brownian diffusivity
$\boldsymbol{E}$	Deformation rate tensor
E_m	Magnetic energy
$\boldsymbol{f}$	Force on a particle
$\boldsymbol{F}$	Force on a material body
$\boldsymbol{G}$	Pressure gradient
$\boldsymbol{H}$	Magnetic field
$\boldsymbol{H}_e$	Effective field
I	Electric current
I_r	Rotational moment of inertia
$\boldsymbol{I}$	Identity tensor
$\boldsymbol{J}$	Electric current density
k	Boltzmann constant
K_s	Self-diffusivity coefficient
K_c	Down-gradient diffusivity coefficient
L	Capillary length
$\boldsymbol{L}$	Torque tensor

$\boldsymbol{\mathcal{L}}$	Langevin function
$\boldsymbol{m}$	Magnetic dipole moment
$\boldsymbol{M}$	Magnetization
n	Density number
$\hat{\boldsymbol{n}}$	Unit vector
N	Number of particles
N_v	Number of turns in the coil
p	Mechanical pressure
p_m	Magnetic pressure
$\boldsymbol{p}$	Momentum
Pe	Global Péclet number
Pe_w	Wall Péclet number
$\mathcal{P}$	Probability density function
Q	Flow rate
S	Surface of a region
$\boldsymbol{S}$	Particle *stresslet*
t	Time
$\boldsymbol{t}$	Torque on a particle
$\boldsymbol{T}$	Tensorial quantity
$\boldsymbol{u}$	Velocity
U	Average velocity
v	Volume of a particle
V	Volume of a region
W	Work
$\boldsymbol{W}$	Rotation tensor
$\boldsymbol{x}$	Position vector

Subscript:

h	Hydrodynamic
m	Magnetic
w	Wall

Coordinate systems:

x, y, z	Cartesian coordinates
r, φ, z	Cylindrical coordinates

1 Introduction

1.1 Magnetic Fluids

Magnetic fluids have attracted considerable attention during the last decades due to the possibility of controlling externally the fluid properties and motion. Successful commercial applications were found in process and exclusion seals, precision film bearings, inertia dampers, loudspeakers, among others (Raj and Moskowitz, 1990; Zahn, 2001). Studies involving biomedical applications are highly promising, such as magnetic drug delivery and hyperthermia (Lübbe et al., 2001; Alexiou et al., 2006; Al-Jamal et al., 2016). The development of new applications for magnetic fluids requires a precise understanding of its properties and behavior. However, the variety of mechanisms that are present, such as chain formation and break-up, polydispersity, or hydrodynamic dispersion, imposes a challenge to new models. Most current models are limited to equilibrium conditions or non-interacting particles. Besides, the type of flow present in the application must be considered when characterizing the fluid. Magnetic drug targeting, for example, occurs in micron-sized capillary flows. The fluid's viscosity and diffusion will deeply affect the drug delivery efficiency (Gitter and Odenbach, 2011). However, most experimental studies for magnetic fluids are conducted with rotational rheometers. The latter can not reproduce the shear-induced migration that may occur in quadratic flows. Therefore, more studies must be conducted in capillary geometries.

From the constitutive point of view, a magnetic fluid is a suspension of magnetic particles in a Newtonian aqueous or organic carrier fluid. Usually, a surfactant is added to prevent particle aggregation. Accordingly to the particle size, these fluids fall into two different categories, which differ in their stability and rheological response. Suspensions of nanometric particles are called ferrofluids, which are the focus of the present work. With a typical diameter of 10 μm, these particles are mono-domain permanent magnetic dipoles and are usually made of magnetite or cobalt (Rinaldi et al., 2005; Odenbach, 2009). The action of Brownian motion provides long term stability even at high fields. Their rheological response to applied magnetic fields is modest. If the particles are micro-sized, the suspension is classified as a magneto-rheological fluid (MRF) (Bossis et al., 2002; De Vicente et al., 2011). At this scale, the Brownian motion can not keep the particles in suspension and sedimentation will occur quickly, especially when a field is applied. To increase the stability, the particles can be coated or nanometric particles can be added to the suspension. In contrast with a ferrofluid, an MRF has the advantage of a strong rheological response to an applied field, due to the strong dipolar interaction between particles. In relation to the use, ferrofluids are preferred for magnetic seals and bearings, where stability and reliability are needed, while MRFs are used in dampers, which require strong responses and can perform a remixing between cycles.

1.2 Rheological characterization of ferrofluids

The modeling of ferrofluids combines the electromagnetism of non-conducting media with the hydrodynamics of rigid particle suspension. This field is commonly called *Ferrohydrodynamics* (FHD) (Cunha, 2012; Rosensweig, 2013). It opposes the *Magnetohydrodynamics* (MHD), which deals with the hydrodynamics of conducting fluids under the action of the Lorentz force. Great reviews on the hydrodynamics of ferrofluids were given by Rinaldi et al. (2005) and Odenbach (2009).

In the absence of an applied field, the magnetic particles are randomly oriented due to Brownian motion. Therefore, the ferrofluid behaves as an ordinary particle suspension. If an external magnetic field is applied, the magnetic particles will suffer from forces and torques, which will be transferred to the base fluid. For a dilute suspension of non-interacting spherical particles, the modified momentum equation is (Rinaldi et al., 2005)

$$\rho \frac{D\boldsymbol{u}}{Dt} = -\nabla p + \eta_o \left(1 + \frac{5}{2}\phi\right) \nabla^2 \boldsymbol{u} + \mu_o \boldsymbol{M} \cdot \nabla \boldsymbol{H} + \frac{\mu_o}{2} \nabla \times (\boldsymbol{M} \times \boldsymbol{H}) \ , \tag{1.1}$$

where ρ is the density, $\boldsymbol{u}$ is the velocity, t is the time, p is the pressures, η_o is the carrier fluid viscosity, ϕ is the particle volume fraction, μ_o is the vacuum magnetic permeability, $\boldsymbol{M}$ is the magnetization and $\boldsymbol{H}$ is the magnetic field.

The term $\boldsymbol{M} \cdot \nabla \boldsymbol{H}$ refers to the action of field gradients. This term is of most importance in phenomena such as the Rosensweig's instability (Rosensweig, 2013) or in applications such as the process of magnetic separation under the action of an external magnetic field in the capture of oil spills (Cunha and Sobral, 2004); the drag reduction in capillaries due to the effect of a magnetic field gradient in a pressure-driven flow (Rosa et al., 2016) and the behavior of a magnetic liquid-liquid interface formed between two vertical flat plates in response to vertical magnetic fields (Gontijo et al., 2016).

The term $\nabla \times (\boldsymbol{M} \times \boldsymbol{H})$, which will be the most important for this work, is non-null only when the magnetization and the magnetic field are misaligned. If the vorticity is relevant in a certain flow, the magnetic particles will tend to rotate away from the magnetic field direction. A competition will be established between the hydrodynamic torque and the restoring magnetic torque. The result is an additional viscous dissipation of the fluid, named magneto-viscous effect (MVE) (Rinaldi et al., 2005). This effect was first observed experimentally by McTague (1969).

From the rheological point of view, ferrofluids present a variety of interesting phenomena that are not yet fully understood. The most basic rheological response is the MVE under a constant shear rate experiment. Consider a simple shear between parallel plates, with an applied magnetic field H transverse to the plates. Simplifying equation (1.1), the magnetic term can be rewritten into an equivalent viscous term,

$$\frac{\mu_o M_\perp H}{2} = \eta_r \dot{\gamma} \ , \tag{1.2}$$

where $M_\perp$ is the component of the magnetization perpendicular to the applied field and $\dot{\gamma}$ is the shear rate. η_r is defined as the rotational viscosity and is a quantitative measure of the MVE.

A model that would predict the MVE could no longer consider the magnetization to be aligned with the magnetic field (*i.e.* $\boldsymbol{M} = \chi(H)\boldsymbol{H}$). The first relaxation equation for the magnetization was proposed by Shliomis (1971), based on a phenomenological extension of the Debye's equation. Shortly after, Martsenyuk et al. (1973) derived a new model from a Fokker-Planck equation, which the authors sustained that remained valid even very far from equilibrium. More recently, Felderhof (2000) and Shliomis (2001) proposed different phenomenological equations based on irreversible thermodynamics. However, all of the cited models are limited to dilute suspensions with no particle-particle interactions.

Patel et al. (2003), Bacri et al. (1995) and Schumacher et al. (2003) developed experimental measurements of the MVE and tried to validate the available theoretical models. The effective-field model of Martsenyuk et al. (1973) presented the best qualitative agreement but diverged quantitatively in all cases. In fact, even for very dilute suspensions, the measured value for the MVE was an order of magnitude higher than the predicted theoretical value.

An experimental study from Odenbach and Raj (2000) showed that large particles and agglomerates are responsible for most of the increase in the viscosity of a ferrofluid. The physical non-dimensional parameter that accounts for inter-particle interactions is

$$\lambda = \frac{\mu_o m^2}{24kTv} \ , \tag{1.3}$$

where m is the magnetic dipole moment, k is the Boltzmann constant, T is the absolute temperature and v is the particle volume. For a typical magnetite particle of 10 nm, $\lambda \sim 1$, which is not high enough so that particle-particle interactions would be relevant. However, if a diameter dispersion is considered, than a small fraction of large particles would have a high value of λ. This particles will form large aggregates, which have a much higher dissipative response when compared to the isolated particles. In fact, Odenbach and Raj (2000) verified that, if the fraction of large particle is decreased for a fixed value of ϕ, the MVE decreases accordingly. Therefore, the authors concluded that particle-particle interactions play a very important role in the rheology of ferrofluids.

A few recent kinetic models incorporate particle-particle interaction, but closed macroscopic equations are still limited to weak flows. Ilg and Hess (2003) developed the

Dynamical Mean-Field Model, which expands the model of Martsenyuk et al. (1973) allowing for weak particle-particle interactions. The macroscopic equations are derived through an expansion in ϕ and λ. This model overcomes several limitations of the previous non-interacting model. A higher MVE is predicted, along with different viscosity coefficients accordingly to the orientation of the field in relation to the flow. Also, normal stress differences can be predicted with this model. However, the dynamical mean-field model is limited to the dilute and weakly interacting regime.

In the strongly interacting regime, particle chains must be considered into the model. Zubarev and Iskakova (1995) and Ilg and Kröger (2002) presented kinetic models for a ferrofluid composed of chain aggregates. The stress tensor is obtained modeling the chains as perfect rigid spheroids. The main difficult arises from the determination of the non-equilibrium magnetization and the orientation distribution function, which are in general not known. Usually, a Stokesian dynamics simulation is required to obtain this properties. Closed form macroscopic equations are only available at limiting cases of uniaxial symmetry. Also, flow-induced structural changes are not well understood (Odenbach, 2009). Progress into the interacting and non-equilibrium regimes has been made with particle simulations (Zubarev and Iskakova, 1995; Ilg et al., 2006; Rosa et al., 2017; Rosa and Cunha, 2019, 2020; Cunha et al., 2020).

Apart from the MVE, ferrofluids presents other very rich non-Newtonian behaviors. Bacri et al. (1995) discovered that ferrofluids may present "negative" viscosity in pipe flow under an oscillatory magnetic field at a certain frequency range. In fact, there is a decrease in the suspension viscosity due to the conversion of electromagnetic energy to mechanical work. Odenbach et al. (1999) verified the existence of normal stress difference in ferrofluids using reduced gravity experiments.

1.3 Hydrodynamic dispersion

Rigid particle suspension may present a non-uniform concentration profile when subjected to a shear rate gradient. This mechanism, called *hydrodynamic* or *shear-induced dispersion*, differs from the classical Brownian diffusion since its origins are on the irreversible interactions between particles in a suspension. Therefore, this is not a random process, but rather a deterministic fluctuation induced by a shear. This effect is highly sensitive to irreversibilities such as surface roughness (Cunha and Hinch, 1996), contact forces (Drazer et al., 2002), magnetic interactions (Roure and Cunha, 2018), three-particles interactions (Wang et al., 1998), inertia (Subramanian and Brady, 2006), electric charge (Breedveld and Levine, 2003), non-sphericity (Lopez and Graham, 2007), shape deformation (Hudson, 2003; Lac and Barthès-Biesel, 2008), among others.

Eckstein et al. (1977) were the first to verify and measure this phenomenon. The physical origins and scaling arguments were later clarified in Leighton and Acrivos (1987a,b);

Acrivos et al. (1992). Experiments demonstrated that the diffusivity on dilute suspensions scales with $\dot{\gamma}a^2$, where $\dot{\gamma}$ is the shear rate and a is the particle's radius (Leighton and Acrivos, 1987a). The dependence on the particle's volume fraction ϕ changes accordingly to the type of particle interaction. Two-body collisions result in a diffusivity proportional to ϕ, while multi-body collisions result in a higher-order dependence.

The determination of the diffusivity coefficient presents the main difficulty to the study of this phenomenon. The experimental studies from Leighton and Acrivos (1987a), Zarraga and Leighton Jr (2002) and Eckstein et al. (1977) measured values an order of magnitude higher than the theoretical ones but with a high scatter of data. Cunha and Hinch (1996) developed a model to determined the self and down-gradient diffusivities in a suspension of rough spheres. More recently, Roure and Cunha (2018) extended their theory for suspensions of magnetic particles with dipole interaction.

Shear-induced dispersion plays a very important role in the flow of a suspension. A settled bed can be remixed with a simple shear flow. On the other hand, a shear rate gradient can produced a particle segregation and a change in the apparent viscosity of the suspension. The higher collision frequency in a high shear region will induce a particle migration towards the low shear region. Phillips et al. (1992) proposed a constitutive equation for the particle flux in concentrated suspension. Modifications to this equations were later proposed by Krishnan et al. (1996) and Kim et al. (2008). An experimental work by Koh et al. (1994) verified that a non-uniform concentration profile is formed in quadratic shear flows. Alvariño et al. (2015) applied the model from Cunha and Hinch (1996) to investigate the thermal properties of nanofluids. Yet, no study in the literature considered the shear-induced dispersion to the flow of magnetic fluids.

1.4 Objectives

The present work conducts a theoretical and experimental investigation of the flow of a dilute ferrofluid in a capillary tube under the action of an applied magnetic field. The main objective is to study the influence of a shear-induced dispersion on the magnetoviscous effect. The flow is assumed laminar and fully developed, so that inertial and convective terms are not important. The applied magnetic field is uniform and longitudinal. The shear-induced dispersion is assumed to be originated on the particle's rugosity or non-sphericity. Magnetic inter-particles forces are neglected. The specific objectives of the present work are:

- Write the system governing equations in a non-dimensional form and identify the non-dimensional physical parameters;
- Solve the one-dimensional governing system using a radial discretization of the domain and an integration routine for the differential equations;

- Using a pertubation method, obtain asymptotic solutions for limiting cases of the non-dimensional physical parameters;
- Obtain theoretical predictions of the volume fraction profile, the magnetization profile, and the viscosity for two models: a suspension of rough spherical particles and a suspension of smooth spheroidal particles.
- Evaluate the influence of the diffusivity coefficient and the particle's rugosity or non-sphericity on the rheological response of the ferrofluid;
- Measure the viscosity of a commercial ferrofluid under the action of an applied field using a capillary viscometer setup and a rotational rheometer;
- Compare the theoretical and experimental results and identify the ranges of validity of the theoretical models.

2 Theory of Magnetic Fluids Hydrodynamics

The description of the physical behavior of magnetic fluids flow is settled on the fundamental laws of continuum mechanics and electromagnetism. Although valid to any kind of flow and material, these balance equations are not sufficient to fully describe the hydrodynamics. Therefore, additional equations, named constitutive equations, are needed to complete the description. These equations are based on empirical observations or fundamental hypothesis about the nature of a given material. In this chapter, the balance equations of the continuum mechanics and the electromagnetism are stated. After, constitutive models for the stress tensor, the magnetization of a magnetic fluid and the particle flux are presented.

2.1 Balance equations of the continuum mechanics

In this section, the balance equations of the fluid mechanics are derived from the continuum mechanic's laws of mass and momentum conservation. The law of energy conservation is not relevant to this problem.

2.1.1 Mass balance equation

Consider a material body with a density ρ and a volume V. The mass conservation principle states that the time variation of the mass is null in a reference frame moving with the body,

$$\frac{d}{dt}\int_{V(t)} \rho dV = 0 \; . \tag{2.1}$$

where $\boldsymbol{u}$ is the fluid's velocity. Applying the Reynolds Transport Theorem (Aris, 2012) in equation (2.1) results that

$$\int_{V(t)} \frac{\partial \rho}{\partial t} dV + \int_{\partial V(t)} \rho \boldsymbol{u} \cdot \hat{\boldsymbol{n}} dS = 0 \; . \tag{2.2}$$

Using the divergence theorem (Aris, 2012), the surface integral can be transformed into a volume integral,

$$\int_{V(t)} \frac{\partial \rho}{\partial t} dV + \int_{V(t)} \nabla \cdot (\rho \boldsymbol{u}) dV = 0 \ . \tag{2.3}$$

Since the volume V is arbitrary, the localization theorem (Aris, 2012) allows the mass conservation equation to be written in a differential form,

$$\frac{\partial \rho}{\partial t} + \nabla \cdot (\rho \boldsymbol{u}) = 0 \ , \tag{2.4}$$

also called continuity equation. If the density is constant and uniform, this equation can be simplified into the form

$$\nabla \cdot \boldsymbol{u} = 0 \ . \tag{2.5}$$

2.1.2 Diffusion equation

The diffusion equation is a particular case of the mass balance equation when the fluid has more than one component and no chemical reactions occur. Consider the equation (2.4) applied only for the component i,

$$\frac{\partial \rho_i}{\partial t} + \nabla \cdot (\rho_i \boldsymbol{v}_i) = 0 \ , \tag{2.6}$$

where ρ_i and $\boldsymbol{v}_i$ are the density and velocity of the component i. The component's density can be written as $\rho_i = \phi_i \rho_m$, where ϕ_i is component's volume fraction and ρ_m is the density of pure material i. Therefore,

$$\frac{\partial \phi_i}{\partial t} + \nabla \cdot (\phi_i \boldsymbol{v}_i) = 0 \ . \tag{2.7}$$

Equation (2.7) is manipulated so that the mean fluid velocity $\boldsymbol{u}$[1] appears,

$$\frac{\partial \phi_i}{\partial t} + \nabla \cdot (\phi_i \boldsymbol{v}_i - \phi_i \boldsymbol{u} + \phi_i \boldsymbol{u}) = 0 \ . \tag{2.8}$$

This equation is rearranged in the form,

$$\frac{D\phi_i}{Dt} + \phi_i \nabla \cdot \boldsymbol{u} = -\nabla \cdot (\phi_i \boldsymbol{v}_i - \phi_i \boldsymbol{u}) \ . \tag{2.9}$$

where $D/Dt = \partial/\partial t + \boldsymbol{u} \cdot \nabla$ is the material derivative in the Lagrangian frame. We define the volumetric flux of the component i as $\boldsymbol{N}_i = \phi_i(\boldsymbol{v}_i - \boldsymbol{u})$. If the incompressibility condition (2.5) is valid and the suspension has only one particulate phase, than the equation (2.9) can be simplified to

$$\frac{D\phi}{Dt} = -\nabla \cdot \boldsymbol{N} \ . \tag{2.10}$$

---

[1] The mean fluid velocity is defined as $\boldsymbol{u} = \Sigma \rho_i \boldsymbol{v}_i / \Sigma \rho_i$

2.1.3 Momentum balance equation

Accordingly to the momentum conservation equation, written in the form of the Newton's second law, the material time derivative of the momentum equates the net force on the body,

$$\frac{d}{dt}\int_{V(t)} \rho \boldsymbol{u} dV = \boldsymbol{F} \ . \tag{2.11}$$

The net force on the body can be divided in terms of the body force density $\boldsymbol{b}$ and the stress tensor $\boldsymbol{\sigma}$,

$$\boldsymbol{F} = \int_{V(t)} \rho \boldsymbol{b} dV + \int_{\partial V(t)} \hat{\boldsymbol{n}} \cdot \boldsymbol{\sigma} dS \ . \tag{2.12}$$

Substituting the equation (2.12) in (2.11) and applying the the Reynolds' transport and the divergence theorems results that

$$\int_{V(t)} \frac{\partial}{\partial t}(\rho \boldsymbol{u}) dV + \int_{V(t)} \nabla \cdot (\rho \boldsymbol{u}\boldsymbol{u}) dV = \int_{V(t)} \rho \boldsymbol{b} dV + \int_{V(t)} \nabla \cdot \boldsymbol{\sigma} dV \ . \tag{2.13}$$

Again, the localization theorem allows to rewrite the momentum conservation equation in the differential form,

$$\frac{\partial}{\partial t}(\rho \boldsymbol{u}) + \nabla \cdot (\rho \boldsymbol{u}\boldsymbol{u}) = \rho \boldsymbol{b} + \nabla \cdot \boldsymbol{\sigma} \ . \tag{2.14}$$

Using the equation (2.4) to simplify the equation (2.14) the Cauchy equation is obtained,

$$\rho \frac{D\boldsymbol{u}}{Dt} = \rho \boldsymbol{b} + \nabla \cdot \boldsymbol{\sigma} \ . \tag{2.15}$$

2.2 Magnetostatics

In this section, we present the main quantities and equations of electromagnetism in the regime of Ferrohydrodynamics, *i.e.*, in the absence of free charge and electric currents. In the sequence, the magnetic force and torque acting upon a magnetic dipole are derived. Here, all equations are presented in the SI unit system, thus they may differ in the form from those presented in the CGS system.

2.2.1 Maxwell's equations

The electromagnetism is governed by the four Maxwell's equations, which relate the main electric and magnetic quantities. In FHD, the magnetic fluid is non-conducting and there is no action of external electric fields. Therefore, all of the electric quantities are null and the electricity Gauss' law and the Faraday's law are not relevant (Cunha, 2012; Grant and Phillips, 2013). Only the magnetism Gauss' law and the Ampère's law are relevant in FHD, which are derived as follows.

The two fundamental magnetic quantities are the flux density vector $\boldsymbol{B}$ and the magnetic field $\boldsymbol{H}$. In general, $\boldsymbol{B}$ is chosen as the most fundamental quantity due to its generality. It can be defined from the Biot-Savart law for a electric current $\boldsymbol{I}$ over a circuit C,

$$\boldsymbol{B} = \frac{\mu_o}{4\pi} \oint_C \frac{\boldsymbol{I} \times \boldsymbol{r}}{r^3} dl \ , \tag{2.16}$$

where $\boldsymbol{r}$ is the position vector between the field point and the differential line element dl. The magnetism Gauss' law is a direct consequence of the absence of magnetic monopoles, and says that the flux of $\boldsymbol{B}$ over a closed surface S is null,

$$\int_S \boldsymbol{B} \cdot \hat{\boldsymbol{n}} dS = 0 \ , \tag{2.17}$$

where $\hat{\boldsymbol{n}}$ is a unit vector associated with the surface element dS and oriented outwards. Applying the divergence theorem and the localization theorem to equation (2.17) allows to obtain its differential form,

$$\nabla \cdot \boldsymbol{B} = 0 \ . \tag{2.18}$$

The magnetic field $\boldsymbol{H}$ can be defined from the flux density $\boldsymbol{B}$, by the relation

$$\boldsymbol{H} = \frac{\boldsymbol{B}}{\mu_o} - \boldsymbol{M} \ , \tag{2.19}$$

where μ_o is the vacuum magnetic permeability and $\boldsymbol{M}$ is the material magnetization. This quantity requires a constitutive model and will be discussed in section 2.4.

In stationary electric circuits, the Ampère's law postulates that the magnetic field's circulation on closed path C equals the electric current passing through a surface S limited by C,

$$\oint_C \boldsymbol{H} \cdot \boldsymbol{dl} = \int_S \boldsymbol{J} \cdot \hat{\boldsymbol{n}} dS \ . \tag{2.20}$$

Applying the Stokes theorem for a closed path integral, results that

$$\int_S (\nabla \times \boldsymbol{H}) \cdot \hat{\boldsymbol{n}} dS = \int_S \boldsymbol{J} \cdot \hat{\boldsymbol{n}} dS \ . \tag{2.21}$$

Applying the localization theorem, the Ampère's law can be written in a differential form,

$$\nabla \times \boldsymbol{H} = \boldsymbol{J} \ . \tag{2.22}$$

In FHD there are no electric currents on the fluid. Therefore, the Ampère's law reduces to

$$\nabla \times \boldsymbol{H} = 0 \ , \tag{2.23}$$

Equations (2.18) and (2.23) are the fundamental electromagnetic equations in FHD (Rosensweig, 2013). From the integral form of these equations, the magnetic boundary conditions between two different media can be derived. Consider a Gaussian surface S between the media 1 and 2, according to Figure 2.1. Applying the magnetism Gauss' law (2.17) in the integral form results that

$$\int_S \boldsymbol{B} \cdot \hat{\boldsymbol{n}} dS = S(B_{1n} - B_{2n}) = 0 \ . \tag{2.24}$$

Since the surface S is arbitrary, the localization theorem can be applied. The resulting

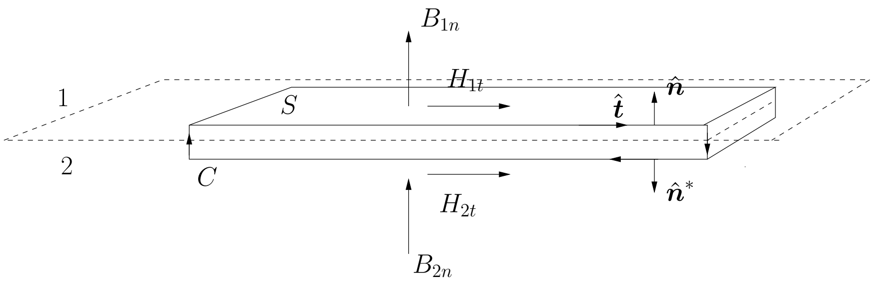

Figure 2.1 – Boundary conditions for the magnetic field and the flux density field.

boundary condition is the continuity of the normal component of $\boldsymbol{B}$,

$$\hat{\boldsymbol{n}} \cdot (\boldsymbol{B}_1 - \boldsymbol{B}_2) = 0 \ . \tag{2.25}$$

Now, shall we consider a closed path C parallel to the border, according to Figure 2.1. From the integral form of the Ampère's law 2.20, the magnetic field satisfy the following relation:

$$\oint_C \boldsymbol{H} \cdot \boldsymbol{dl} = l(H_{1t} - H_{2t}) = 0 \ . \tag{2.26}$$

Again, applying the localization theorem, we obtain the boundary condition of continuity of the tangential component of $\boldsymbol{H}$,

$$\hat{\boldsymbol{n}} \times (\boldsymbol{H}_1 - \boldsymbol{H}_2) = \boldsymbol{0} \ . \tag{2.27}$$

2.2.2 Force and torque upon a magnetic particle

Consider a magnetic point particle, with a fixed magnetic dipole moment $\boldsymbol{m}$ under the action of a external magnetic field $\boldsymbol{H}$. The dipole moment can be defined by a electric current I in a small loop of area A, such that

$$\boldsymbol{m} = IA\hat{\boldsymbol{n}} \ , \tag{2.28}$$

where $\hat{\boldsymbol{n}}$ is a unit vector normal to the loop and oriented accordingly to the right-rand convention. Shall we evaluate the force and torque on the magnetic dipole using the virtual work method. The potential energy associated with the particle is (Schwartz, 1972)

$$E_m = -\mu_o \boldsymbol{H} \cdot \boldsymbol{m} \ . \tag{2.29}$$

Consider a virtual angular displacement $\delta\boldsymbol{\theta}$ over the particle. The energy variation associated with rotation is,

$$\delta E_m = \delta(-\mu_o \boldsymbol{H} \cdot \boldsymbol{m}) = \mu_o(\boldsymbol{H} \times \boldsymbol{m}) \cdot \delta\boldsymbol{\theta} \ . \tag{2.30}$$

The virtual work exerted by the magnetic torque $\boldsymbol{t}_m$ on the particle must balance its potential energy variation:

$$\boldsymbol{t}_m \cdot \delta\boldsymbol{\theta} + \mu_o(\boldsymbol{H} \times \boldsymbol{m}) \cdot \delta\boldsymbol{\theta} = 0 \ . \tag{2.31}$$

Therefore, the expression for the magnetic torque on a dipole is

$$\boldsymbol{t}_m = \mu_o \boldsymbol{m} \times \boldsymbol{H} \ . \tag{2.32}$$

Now, consider a virtual spatial displacement $\delta\boldsymbol{x}$ over the particle. In this case, the potential energy variation is

$$\delta E_m = \delta(-\mu_o \boldsymbol{H} \cdot \boldsymbol{m}) = -\mu_o \nabla(\boldsymbol{H} \cdot \boldsymbol{m}) \cdot \delta\boldsymbol{x} \ . \tag{2.33}$$

Again, the virtual work exerted by the magnetic force $\boldsymbol{f}_m$ on the particle must balance its potential energy variation,

$$-\boldsymbol{f}_m \cdot \delta\boldsymbol{x} = -\mu_o \nabla(\boldsymbol{H} \cdot \boldsymbol{m}) \cdot \delta\boldsymbol{x} \ . \tag{2.34}$$

We may conclude that

$$\boldsymbol{f}_m = \mu_o \nabla(\boldsymbol{H} \cdot \boldsymbol{m}) \ . \tag{2.35}$$

Since the magnetic dipole is invariant to a spatial translation, the expression can be simplified to

$$\boldsymbol{f}_m = \mu_o \boldsymbol{m} \cdot \nabla\boldsymbol{H} \ . \tag{2.36}$$

2.3 Formal principles for constitutive equations

The balance equations of continuum mechanics and electromagnetism are derived from conservation principles, thus these equations are material independent. Nevertheless, these equations do not describe completely a physical system, and additional expressions are necessary. Called constitutive equations, they must be based on experimental observations or theoretical models of a given material. Truesdell (1992) proposed a set of principles that a *good* constitutive equation must follow (in order to be valid over a wide range of flow conditions):

- *Principle of Determinism*: A given tensorial quantity $\boldsymbol{T}$ of a material particle $\boldsymbol{X}$ must be determined by its motion history $\boldsymbol{x}^t$:

  $$\boldsymbol{T}(\boldsymbol{X}, t) = \mathfrak{F}(\boldsymbol{x}^t; \boldsymbol{X}, t) \ , \tag{2.37}$$

  where $\mathfrak{F}$ is a functional ;

- *Principle of Local Action*: For some neighborhood $N(\boldsymbol{X})$ of a particle $\boldsymbol{X}$, the motion of particle $\boldsymbol{Z}$ outside of $N(\boldsymbol{X})$ can be disregarded in the evaluation of the quantity $\boldsymbol{T}$ associated with $\boldsymbol{X}$;

- *Principle of Material Frame-Indifference*: A constitutive equation must be invariant under changes of frame of reference. In other words, the material quantities must be objective, *i.e.*, obey the following transformation rule,

$$\begin{cases} a' = a & \text{(scalar)}, \\ \boldsymbol{b}' = \boldsymbol{Q}\cdot\boldsymbol{b} & \text{(vector)}, \\ \boldsymbol{T}' = \boldsymbol{Q}\cdot\boldsymbol{T}\cdot\boldsymbol{Q}^T & \text{(tensor)}, \end{cases} \tag{2.38}$$

where $\boldsymbol{Q}$ is a ortogonal tensor associated with a change of reference, and $'$ indicates the value of the quantity in another reference frame.

2.4 Magnetization relaxation equation

2.4.1 Magnetization definition

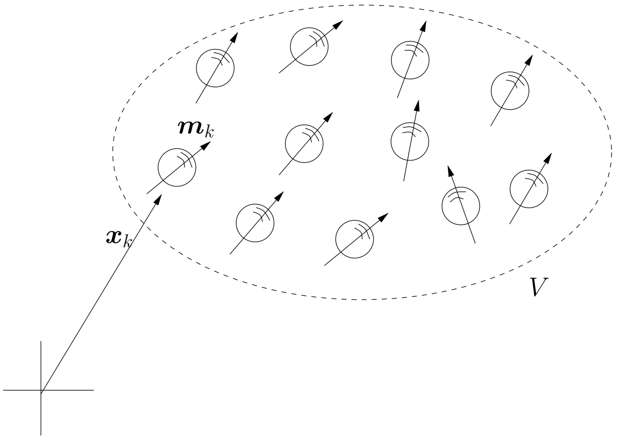

Figure 2.2 – Suspension of magnetic particles.

The magnetization is a macroscopic quantity that measures the degree of polarization on a magnetizable continuum media (Cunha, 2012). Although every material presents some degree of polarization, ferromagnetic materials such as iron, cobalt, and nickel can intensify the applied field some hundreds of times. The magnetization is defined as the magnetic dipole moment per unit volume at a characteristic region $\delta V'$ (Schwartz, 1972):

$$\boldsymbol{M} = \frac{\delta \boldsymbol{m}}{\delta V'} \tag{2.39}$$

In a particle suspension, three typical scales can be addressed: the atomic scale, the particle's scale, and the suspension continuum scale. The first one is out of the scope of this work. At the particle scale, the solid material can be considered as uniform, so that the particle's magnetic dipole moment $\boldsymbol{m}$ and solid phase magnetization $\boldsymbol{M}_d$ are related by

$$\boldsymbol{m} = v_m \boldsymbol{M}_d \ , \tag{2.40}$$

where v_m is the volume of the particle's magnetic core. For mono-domain particles (*i.e.* ferrofluids), the intensity of the solid magnetization M_d is simply the material's saturation magnetization.

In order to define the magnetization at the suspension continuum scale, a volume V containing a sufficiently large number N of particles must be considered, represented in Figure 2.2. Each particle has a fixed magnetic dipole moment $\boldsymbol{m}_k$ of intensity m and the same volume v_m (*i.e.* mono-disperse suspension). If the moment distribution is statistically homogeneous and independent of V, then the local magnetization $\boldsymbol{M}$ can be defined by the following volumetric average:

$$\boldsymbol{M} = \frac{1}{V}\int_V d\boldsymbol{m} \ , \tag{2.41}$$

where $d\boldsymbol{m}$ is the dipole moment associated with a differential element dV. The total volume V is composed of the carrier fluid volume V_f, which has no magnetic moment, and the volume of each particles.

$$\boldsymbol{M} = \frac{1}{V}\int_{V_f} d\boldsymbol{m} + \frac{1}{V}\sum_{k=1}^{N}\int_{v_k} d\boldsymbol{m} = \frac{1}{V}\sum_{k=1}^{N}\boldsymbol{m}_k \ . \tag{2.42}$$

The mean magnetic moment $\overline{\boldsymbol{m}}$ is defined by

$$\overline{\boldsymbol{m}} = \frac{1}{N}\sum_{k=1}^{N}\boldsymbol{m}_k \ . \tag{2.43}$$

Combining equations (2.42) and (2.43) results that:

$$\boldsymbol{M} = \frac{N}{V}\overline{\boldsymbol{m}} \ . \tag{2.44}$$

The ratio N/V is defined as the density number n, being equal to ratio between the particle's magnetic volume fraction ϕ_m and the magnetic volume. Therefore,

$$\boldsymbol{M} = n\overline{\boldsymbol{m}} = \frac{\phi_m}{v_m}\overline{\boldsymbol{m}} \ . \tag{2.45}$$

2.4.2 Equilibrium magnetization

For a ferrofluid in the absence of an applied field, the magnetic dipoles of the particles are randomly oriented due to the thermal agitation, producing a null magnetization. When an external field $\boldsymbol{H}$ is applied, the dipoles will produce a net magnetization in the field orientation, whose intensity will increase with the applied field until saturation is obtained. Rosensweig (2013) obtained an expression for the equilibrium condition based on Langevin's theory for paramagnetism. From equation (2.30), the work required to rotate a dipole from the field direction to an angle θ is

$$W = mH(1 - \cos\theta) \ . \tag{2.46}$$

The distribution function $\mathcal{P}(\theta)$ of the dipole orientation is given by

$$\mathcal{P}(\theta) = \frac{e^{-\dfrac{W}{kT}}\sin(\theta)}{\displaystyle\int_0^{\pi} e^{-\dfrac{W}{kT}}\sin(\theta)d\theta} \ , \tag{2.47}$$

where k the Boltzmann's constant, T is the absolute temperature. The mean magnetic moment is given by

$$\overline{\boldsymbol{m}} = \hat{\boldsymbol{e}}_H \int_0^\pi (m \cos\theta)\mathcal{P}(\theta) d\theta \ . \tag{2.48}$$

Solving this integral results that

$$\overline{\boldsymbol{m}} = m\mathcal{L}(\alpha)\hat{\boldsymbol{e}}_H \ , \tag{2.49}$$

where $\mathcal{L}(\alpha)$ is the Langevin function, given by

$$\mathcal{L}(\alpha) = \coth(\alpha) - \frac{1}{\alpha} \ . \tag{2.50}$$

The local Langevin parameter α is defined by

$$\alpha = \frac{\mu_o m H}{kT} \ . \tag{2.51}$$

It represents the ratio between the magnetic force and Brownian force. Substituting equations (2.49) and (2.40) in (2.45) results that the equilibrium magnetization $\boldsymbol{M}_o$ of the suspension is

$$\boldsymbol{M}_o = \phi_m M_d \mathcal{L}(\alpha)\hat{\boldsymbol{e}}_H \ . \tag{2.52}$$

In the limit of $\alpha \to \infty$, the Langevin function goes to $\mathcal{L}(\alpha) \to 1$. Therefore, the saturation magnetization M_s of the fluid is

$$M_s = \phi_m M_d \ . \tag{2.53}$$

The expression (2.52) can be rewritten as a superparamagnetic relation between the equilibrium magnetization and the magnetic field,

$$\boldsymbol{M}_o = \chi(H)\boldsymbol{H} \ , \tag{2.54}$$

where $\chi(H)$ is the magnetic susceptibility of the fluid. In the limit of $\alpha \to 0$, the Langevin function can be approximated by $\mathcal{L}(\alpha) \approx \alpha/3$. Therefore, the Langevin initial susceptibility can be defined as

$$\chi_i = \frac{\mu_0 m M_s}{3kT} \ . \tag{2.55}$$

2.4.3 Magnetization relaxation equation

Consider a reference frame that moves and rotates with the average position and orientation of the magnetic particles. If a small deviation from the equilibrium condition is present, the magnetization will relax via a Debye equation (Shliomis, 1971):

$$\frac{\partial \boldsymbol{M}}{\partial t} = \frac{1}{\tau}\left(\boldsymbol{M}_o - \boldsymbol{M}\right) \ , \tag{2.56}$$

whose solution is an exponential decay and τ is the relaxation time. The magnetic dipole can rotate by two main mechanisms. The first is the internal slip of atomic spins with no particle rotation. Its characteristic time is the Néel time τ_n, defined as (Rinaldi et al., 2005)

$$\tau_n = \tau_o e^{\frac{K v_m}{kT}} \ , \tag{2.57}$$

where K and τ_o are material constants. The other rotation mechanism is the rotational Brownian diffusion of the particle itself. The Brownian rotational time τ_b for a spherical particle is given by

$$\tau_b = \frac{3\eta_o v_h}{kT} \ , \tag{2.58}$$

Here, v_h is the particle's hydrodynamic volume (*i.e.* the magnetic core's volume v_m plus the surfactant layer) and η_o is the carrier fluid viscosity (Brady and Bossis, 1988). The relaxation time relates to the rotational Brownian diffusivity D_r by $\tau_b = 1/2D_r$. The total magnetization relaxation time is a harmonic mean of the Néel and Brownian times,

$$\tau = \frac{\tau_n \tau_b}{\tau_n + \tau_b} \ . \tag{2.59}$$

The main rotation mechanism will be that with the smallest relaxation time. The Néel time scales with $\tau_n \propto \exp(v_m)$ while the Brownian time scales with $\tau_b \propto v_h$. Therefore, for particles larger than a certain critical length (yet not large enough to be multi-domain), $\tau_b \ll \tau_n$. Most commercial ferrofluids have a mean magnetic diameter of 10 nm, which satisfy this condition. Therefore, we shall consider the magnetic dipole to be fixed in the particle and the relaxation time as simply the Brownian rotational time, $\tau = \tau_b$.

In order to be a valid constitutive equation, the expression (2.56) must satisfy the *MFI* principles describe in section 2.3. The right-hand side of the equation is already an objective quantity. The partial time derivative, however, must be substituted by an objective derivative. Since our reference system translates and rotates with the mean particle position and orientation, the appropriate derivative is a co-rotative derivative for a vector:

$$\frac{\mathfrak{D}\boldsymbol{M}}{\mathfrak{D}t} = \frac{\partial \boldsymbol{M}}{\partial t} + \boldsymbol{u} \cdot \nabla \boldsymbol{M} + \boldsymbol{M} \times \overline{\boldsymbol{\Omega}} \ , \tag{2.60}$$

where $\overline{\boldsymbol{\Omega}}$ is the mean particle angular velocity. Applying the derivate (2.60) in the equation (2.56) results that

$$\frac{\partial \boldsymbol{M}}{\partial t} + \boldsymbol{u} \cdot \nabla \boldsymbol{M} + \boldsymbol{M} \times \overline{\boldsymbol{\Omega}} = \frac{1}{\tau_m} \left(\boldsymbol{M}_o - \boldsymbol{M} \right) \ , \tag{2.61}$$

To evaluate the mean particle angular velocity, we start from the torque's balance equation for a single magnetic particle:

$$I_r \frac{d\boldsymbol{\Omega}}{dt} = \boldsymbol{t}_h + \boldsymbol{t}_m + \boldsymbol{t}_b + \boldsymbol{t}_{di} \ , \tag{2.62}$$

Here, I_r is the particle's angular moment of inertia, $\boldsymbol{\Omega}$ is the particle's angular velocity and $\boldsymbol{t}_h$, $\boldsymbol{t}_m$, $\boldsymbol{t}_b$, $\boldsymbol{t}_d$ are respectively the hydrodynamic, magnetic, Brownian and dipolar torques. The hydrodynamic torque acting on a sphere is given by the second Fáxen law,

$$\boldsymbol{t}_h = 6\eta_o v_h \left(\frac{1}{2} \boldsymbol{\xi} - \boldsymbol{\Omega} \right) \ , \tag{2.63}$$

where $\boldsymbol{\xi}$ is fluid vorticity evaluated at the particle's center. If the dipolar interaction parameter λ is sufficiently small, the dipolar interactions can be neglected. Also, for nano-sized particles, the particle's inertia is not relevant for the torque balance. Therefore, equation (2.62) reduces to

$$6\eta_o v_h \left(\frac{1}{2}\boldsymbol{\xi} - \boldsymbol{\Omega}\right) + \mu_o \boldsymbol{m} \times \boldsymbol{H} + \boldsymbol{t}_b = \boldsymbol{0} \ , \tag{2.64}$$

Applying a volumetric average gives

$$6\eta_o v_h \left(\frac{1}{2}\boldsymbol{\xi} - \overline{\boldsymbol{\Omega}}\right) + \mu_o \overline{\boldsymbol{m}} \times \boldsymbol{H} + \overline{\boldsymbol{t}}_b = \boldsymbol{0} \ , \tag{2.65}$$

The Brownian torque is a stochastic process whose average is null. Therefore, the mean particle rotation is

$$\overline{\boldsymbol{\Omega}} = \frac{1}{2}\boldsymbol{\xi} + \frac{\mu_o}{6\eta_o v_h}\overline{\boldsymbol{m}} \times \boldsymbol{H} \ . \tag{2.66}$$

Applying equations (2.66) and (2.45) in (2.61) results in the relaxation equation obtained by Shliomis (1971),

$$\frac{D\boldsymbol{M}}{Dt} = \frac{1}{2}\boldsymbol{\xi} \times \boldsymbol{M} - \frac{\mu_o}{6\eta_o \phi_h}\boldsymbol{M} \times (\boldsymbol{M} \times \boldsymbol{H}) + \frac{1}{\tau}(\boldsymbol{M}_o - \boldsymbol{M}) \ , \tag{2.67}$$

where, $\phi_h = n v_h$ is the hydrodynamic volume fraction. This equation is limited to low shear rates and slowly varying applied magnetic fields, since the Debye relation (2.56) is limited to a small deviation from equilibrium. A new equation that can overcome the shear rate limitation was proposed in a recent paper by Shliomis (2001). A new variable, called the effective field $\boldsymbol{H}_e$, is introduced. It is related to the local magnetization by

$$\boldsymbol{M} = \chi_e \boldsymbol{H}_e \ , \tag{2.68}$$

where $\chi_e = \chi(H_e)$ is the susceptiblity evaluated for the effective field. In the equilibrium condition, the effective field equates the magnetic field, $\boldsymbol{H}_e = \boldsymbol{H}$. Similarly to the magnetization, this quantity relaxation is described by a Debye equation,

$$\frac{\partial \boldsymbol{H}_e}{\partial t} = \frac{1}{\tau}(\boldsymbol{H} - \boldsymbol{H}_e) \ , \tag{2.69}$$

in a reference frame fixed on the particles. Proceeding in the same way as the magnetization, the relaxation equation in the Eulerian frame is (Shliomis, 2001)

$$\frac{D\boldsymbol{H}_e}{Dt} = \frac{1}{2}\boldsymbol{\xi} \times \boldsymbol{H}_e - \frac{\mu_o}{6\eta_o \phi_h}\boldsymbol{H}_e \times (\boldsymbol{M} \times \boldsymbol{H}) - \frac{1}{\tau}(\boldsymbol{H}_e - \boldsymbol{H}) \ . \tag{2.70}$$

This equation presents good results even for large shear rates and will be adopted in this work. For rapidly oscillating magnetic fields this equations does not model well the ferrofluids. Nevertheless, such conditions are out of the scope of this work. Felderhof (2000) proposed a similar phenomenological equation, but it is less accepted in the literature. More general equations were derived from a Fokker-Plank model by Martsenyuk et al. (1973) and Müller and Liu (2002). However, their complexity makes them rather inconvenient to handle.

We propose a modification of the equation (2.70) to account for prolate particles. Consider that the particles are spheroids with a hydrodynamic major axis b_h and a hydrodynamic minor axis a_h and that the dipole moment is fixed on the major axis direction. The Fáxen law (2.70) for an spheroid with the major axis rotating in the shear plane is (Jeffery, 1922)

$$\boldsymbol{t}_h = 6\eta_o v_h \psi_o(\beta)\left(\frac{1}{2}\boldsymbol{\xi}_o - \boldsymbol{\Omega}\right) . \tag{2.71}$$

The geometric function $\psi_0(\beta)$, given on the Appendix B, depends on the spheroid's aspect ratio $\beta = b_h/a_h$. The hydrodynamic volume for such particle is $v_h = 4\pi a_h^2 b_h/3$. Also, the rotational relaxation time also must be correct to $\tau = \psi_0(\beta)3\eta_o v_h/kT$. Applying these corrections to the derivation of the equation (2.70) results that

$$\frac{D\boldsymbol{H}_e}{Dt} = \frac{1}{2}\boldsymbol{\xi} \times \boldsymbol{H}_e - \frac{\mu_o}{6\eta_o \phi_h \psi_0(\beta)}\boldsymbol{H}_e \times (\boldsymbol{M} \times \boldsymbol{H}) - \frac{1}{\tau}(\boldsymbol{H}_e - \boldsymbol{H}) . \tag{2.72}$$

The correction of the magnetization evolution equation for spheroidal particles was first discussed by Martsenyuk et al. (1973) and later implemented by Ilg and Kröger (2002) in a Fokker-Plank model.

2.5 Magnetic fluid stress tensor

The complete description of the hydrodynamics of magnetic fluids requires the balance equations (2.5) and (2.15), as well as a constitutive model for the stress tensor. This model is still a matter of great discussion since it is very difficult to take into account all of the mechanisms that are present in a real ferrofluid (poli-dispersibility, dipolar and hydrodynamic interactions, aggregate shape and breakup). The equivalent stress tensor $\langle\sigma\rangle$ for a suspension of particles is given by the ensemble average of the local stress tensor. If the suspension is statistically homogeneous, this average can be substituted by a volumetric mean over a volume V with a number of particles N sufficiently large (Barthès-Biesel, 2012):

$$\overline{\boldsymbol{\sigma}} = \frac{1}{V}\int_V \boldsymbol{\sigma} dV . \tag{2.73}$$

The volume V is divided in the Newtonian fluid fraction V_f and the volume of each particle v_k.

$$\overline{\boldsymbol{\sigma}} = \frac{1}{V}\int_{V_f} \boldsymbol{\sigma} dV + \frac{1}{V}\sum_{k=1}^{N}\int_{v_k} \boldsymbol{\sigma} dV . \tag{2.74}$$

For the Newtonian fluid phase, the stress tensor is given by $\boldsymbol{\sigma} = -p\boldsymbol{I} + 2\eta_o\boldsymbol{E}$, where $\boldsymbol{E}$ is the deformation rate tensor. Working out the expression for the integral in V_f results that

$$\frac{1}{V}\int_{V_f} \boldsymbol{\sigma} dV = -\overline{p}\boldsymbol{I} + 2\eta_o\overline{\boldsymbol{E}} - \frac{\eta_o}{V}\sum_{k=1}^{N}\int_{s_k}(\boldsymbol{u}\hat{\boldsymbol{n}} + \hat{\boldsymbol{n}}\boldsymbol{u})\, dS + \frac{1}{V}\sum_{k=1}^{N}\int_{v_k} p\boldsymbol{I} dV , \tag{2.75}$$

where $\overline{p}$ and $\overline{\boldsymbol{E}}$ are the volumetric means of p and $\boldsymbol{E}$. The surface integral of the term $(\boldsymbol{u}\hat{\boldsymbol{n}} + \hat{\boldsymbol{n}}\boldsymbol{u})$ is null for particles performing rigid body motion. The integral of the pressure over the particulate phase is an isotropic term that has no influence on the rheology. For an incompressible fluid and particle phases, the pressure is defined over within an arbitrary constant and this integral can be chosen equal to zero. To calculate the particulate phase contribution to the stress tensor, we must consider the particles to be in Stokes flow (*i.e.*, the particle's Reynold's number $\to 0$). In this condition and in the absence of body forces, the moment equation reduces to $\nabla\cdot\boldsymbol{\sigma} = \mathbf{0}$ [2]. Using of the identity, $\boldsymbol{\sigma} = [\nabla\cdot(\boldsymbol{\sigma}\boldsymbol{x})]^T - \boldsymbol{x}(\nabla\cdot\boldsymbol{\sigma})$, the integral over the particulate volume is written as,

$$\int_{v_k} \boldsymbol{\sigma} dV = \int_{v_k} [\nabla\cdot(\boldsymbol{\sigma}\boldsymbol{x})]^T dV \ . \tag{2.76}$$

With the divergence theorem, the volume integral is written as a surface integral,

$$\int_{v_k} \boldsymbol{\sigma} dV = \int_{s_k} \boldsymbol{x}(\hat{\boldsymbol{n}}\cdot\boldsymbol{\sigma}) dS \ . \tag{2.77}$$

The left side of the equation (2.77) is named as the particle's hydrodynamic dipole. Its symmetric part is the particle *stresslet* $\boldsymbol{S}$, and its antisymmetric part is the torque tensor or *rotlet* $\boldsymbol{L}$. Introducing the expressions (2.75) and (2.77) into the equation (2.74) results that the equivalent stress tensor for the suspension is,

$$\overline{\boldsymbol{\sigma}} = -\overline{p}\boldsymbol{I} + 2\eta_o\overline{\boldsymbol{E}} + \overline{\boldsymbol{S}} + \overline{\boldsymbol{L}} \ , \tag{2.78}$$

where $\overline{\boldsymbol{S}} = n\langle\boldsymbol{S}\rangle$ and $\overline{\boldsymbol{L}} = n\langle\boldsymbol{L}\rangle$, and $\langle\ \rangle$ denotes the ensemble average. The most basic model for the *stresslet* is that of a non-interacting, mono-disperse, dilute suspension of spherical particles. A non-interacting model for a magnetic suspension requires, besides of a small volume fraction, that the dipolar interaction parameter be small (typically $\lambda < 1$). In this case, both hydrodynamic and magnetic particle-particle interactions can be neglected. The *stresslet* in this case is simply equal to that of a dilute suspension of non-magnetic spheres (Barthès-Biesel, 2012)

$$\overline{\boldsymbol{S}} = 5\eta_o\phi_h\overline{\boldsymbol{E}} \ . \tag{2.79}$$

The torque tensor relates to the hydrodynamic torque on the particle by $\boldsymbol{L} = \boldsymbol{\epsilon}\cdot\boldsymbol{t}_h/2$. Using the torque balance (2.64) and averaging the expression, the resulting mean torque tensor is:

$$\overline{\boldsymbol{L}} = \frac{\mu_o}{2}(\boldsymbol{HM} - \boldsymbol{MH}) \ . \tag{2.80}$$

The resulting stress tensor for magnetic spherical particles is

$$\overline{\boldsymbol{\sigma}} = -\overline{p}\boldsymbol{I} + 2\eta_\phi\overline{\boldsymbol{E}} + \frac{\mu_o}{2}(\boldsymbol{HM} - \boldsymbol{MH}) \ , \tag{2.81}$$

where $\eta_\phi = (1 + 2.5\phi_h)\eta_o$ is the equivalent Einstein's viscosity. The stress tensor for spheroidal magnetic particles was proposed by Kröger and Sellers (1995) based on the calculations of Brenner and Condiff (1974). The torque tensor remains equal to the

---

[2] The Kelvin force and the gravitational force can be treated separately and superimposed to the homogeneous stress tensor.

expression for perfect spheres. The main difference arises from the *stresslet*, which is given by,

$$\overline{\boldsymbol{S}} = 5\eta_o\phi_h \Big[\psi_1(\beta)\overline{\boldsymbol{E}} + \psi_2(\beta)\left(\overline{\boldsymbol{E}}\cdot\langle\hat{\boldsymbol{n}}\hat{\boldsymbol{n}}\rangle + \langle\hat{\boldsymbol{n}}\hat{\boldsymbol{n}}\rangle\cdot\overline{\boldsymbol{E}}\right) + \psi_3(\beta)\overline{\boldsymbol{E}} : \langle\hat{\boldsymbol{n}}\hat{\boldsymbol{n}}\hat{\boldsymbol{n}}\hat{\boldsymbol{n}}\rangle + \\ \psi_4(\beta)\left(\overline{\boldsymbol{W}}\cdot\langle\hat{\boldsymbol{n}}\hat{\boldsymbol{n}}\rangle - \langle\hat{\boldsymbol{n}}\hat{\boldsymbol{n}}\rangle\cdot\overline{\boldsymbol{W}}\right)\Big] \ . \tag{2.82}$$

where $\overline{\boldsymbol{W}}$ is the rotation tensor. The geometric functions $\psi_i(\beta)$ depend only on the spheroid aspect ratio β and are given in the Appendix B. The stresslet is a function of the dipole orientation $\hat{\boldsymbol{n}} = \boldsymbol{m}/m$, which is fixed on the major axis. In general, the orientation distribution is not known. However, if the Effective-Field Approximation is applied, the order moments of the dipole orientation can be recovered from the solution of the effective field $\boldsymbol{H}_e$. This approximation is the same one applied by Martsenyuk et al. (1973) and Shliomis (2001), and it holds for slowly varying applied magnetic fields. If the aspect ratio β is set to 1, the stress tensor for spherical particles is recovered.

Additionally to the effect of the *stresslet* and the torque tensor, the magnetic particle can also be subjected to a magnetic force in the presence a field gradient. In equilibrium ($\boldsymbol{u} = \boldsymbol{0}$), the Cauchy equation (2.15) in the fluid region surrounding a single point particle at the position $\boldsymbol{x}_k$ is

$$-\nabla p + \boldsymbol{f}_m\delta(\boldsymbol{x}_k) = \boldsymbol{0} \ , \tag{2.83}$$

where $\boldsymbol{f}_m$ is given by equation (2.36). Now, taking the volumetric mean over a sufficiently large number of particles results that

$$\nabla\overline{p} - \mu_o\boldsymbol{M}\cdot\nabla\boldsymbol{H} = \boldsymbol{0} \ . \tag{2.84}$$

The magnetic term can be written as a gradient,

$$\nabla\overline{p} - \nabla\left(\mu_o\int_H \boldsymbol{M}\cdot d\boldsymbol{H}\right) = \boldsymbol{0} \ . \tag{2.85}$$

Therefore, the magnetic body force can be incorporated into the stress tensor as a magnetic pressure define as,

$$p_m = -\mu_o\int_H \boldsymbol{M}\cdot d\boldsymbol{H} \ , \tag{2.86}$$

so that the pressure term in equation (2.78) is now rewritten as $\overline{p} = p + p_m$.

Substituting the equivalent stress tensor (2.78) in the Cauchy's equation (2.15) results in the modified Navier-Stokes equation for a non-interacting ferrofluid,

$$\rho\frac{D\boldsymbol{u}}{Dt} = -\nabla p + \eta_o\nabla^2\boldsymbol{u} + \nabla\cdot\overline{\boldsymbol{S}} + \frac{\mu_o}{2}\nabla\times(\boldsymbol{M}\times\boldsymbol{H}) + \mu_o\boldsymbol{M}\cdot\nabla\boldsymbol{H} \ . \tag{2.87}$$

The left side of the this equation and the first two terms of the right side correspond to the conventional Navier-Stokes equation for Newtonian fluids. Three aditional terms modify this equation to that into in account the magnetic effects. The first magnetic term $\nabla\cdot\overline{\boldsymbol{S}}$ corresponds to the *stresslet* generate by the spherical or spheroidal particles, and is implicitly dependent on the magnetization. The second magnetic term $\mu_o \nabla \times (\boldsymbol{M} \times \boldsymbol{H})/2$ is related to the magnetic torques acting on the particles, and is non-null when there is a misalignment between the magnetic field and the magnetization. The third magnetic term, $\mu_o \boldsymbol{M} \cdot \nabla \boldsymbol{H}$, called Kelvin body force, is related to the magnetic forces acting on the particles, and is non-null when there is a magnetic field gradient. In this work, we investigate the effects of a uniform applied magnetic field in a flow with vorticity effects. Therefore, the latter magnetic term will not be relevant.

2.6 Shear-induced dispersion equation

The diffusive flux is a macroscopic quantity that results from the fluctuating motion of particles in a suspension. The most basic fluctuation mechanism is the Brownian motion, which is the a consequence of the thermal excitation of the surrounding fluid molecules that randomly collide with the particles. But this mechanism has a negligible influence on large particles. Nevertheless, these particles may still present a stochastic movement due to irreversible collisions between particles. These collisions are induced by a shear flow, thus the flux that arises from this mechanism is called *shear-induced dispersion*, or *hydrodynamic dispersion*. The basic constitutive equation for the particle flux is given by Fick's law,

$$\boldsymbol{N} = -\boldsymbol{D}_c \cdot \nabla \phi \ , \tag{2.88}$$

where $\boldsymbol{D}_c$ is the down-gradient diffusivity tensor. $\boldsymbol{D}_c$ is a positive definite tensor, therefore, the diffusive flux is oriented against the concentration gradient. However, there can be a particle flux towards regions of higher concentration if there is a shear rate gradient or a streamline curvature. This flux is termed particle migration and is also a consequence of the shear-induced particles collisions.

2.6.1 Brownian diffusion

The Brownian motion arises from the interaction of the particles with the surrounding fluid molecules, therefore it is more significant in small particles (typically up to 1 μm of diameter). If the movement $\boldsymbol{X}(t)$ of such particle in a quiescent fluid was tracked, the average displacement $\langle \boldsymbol{X} \rangle$ would be null, but the variance of the displacement would be positive. The self-diffusivity $\boldsymbol{D}_s$ is a measure of this second order moment, (Brady and Bossis, 1988)

$$\boldsymbol{D}_s = \frac{1}{2}\frac{\partial}{\partial t}\left\langle \boldsymbol{X}^2 \right\rangle \ . \tag{2.89}$$

Since the Brownian movement is independent of particle-particle interactions, the self-diffusivity is equal to the gradient diffusivity in the Fick's law (2.88). This process is also isotropic, so that $\boldsymbol{D}_s = D_t \boldsymbol{I}$, where D_t is the translational Brownian diffusivity, given by

(Russel et al., 1991)

$$D_t = \frac{kT}{6\pi\eta_o a_h} \ , \tag{2.90}$$

where a_h is the particle hydrodynamic radius. The translational and rotational Brownian diffusivities, D_t and D_r, are related by $D_t/D_r = 4a_h^2/3$.

2.6.2 Irreversible interactions between particles

A large particle ($> 1\mu$m) has a negligible Brownian motion and therefore it would not present a random motion if it were isolated. In order to observe a stochastic motion, it is necessary to consider irreversible particle-particle interactions. Two perfectly smooth spheres in creeping flow present reversible trajectories when they collide. This implies that a particle retains its original streamline even after many collisions. However, many factors such as surface roughness, deformable or non-spherical particles, magnetic dipole force, and three-particle collisions can produce a memory loss in the trajectory. At the dilute regime, the shear-induced diffusivity scales with $\dot{\gamma}a_h^2\phi_h$, since both the shear rate intensity and the particle concentration will increase the collision frequency. At concentrated suspensions, a non-linear dependence with ϕ_h is expected. For example, three-particle interactions will lid to a diffusivity that scales with ϕ_h^2. However, experiments show that these higher-order corrections are negligible for dilute and semi-dilute suspensions (Zarraga and Leighton Jr, 2002).

The self-diffusivity is not equal to the down-gradient diffusivity in the case of shear-induced dispersion, due to the influence of the concentration gradient in the particle flux. Cunha and Hinch (1996) found out that the relation between the diffusivities is

$$\boldsymbol{D}_c = 2\boldsymbol{D}_s + \boldsymbol{D}_f \ , \tag{2.91}$$

where $\boldsymbol{D}_f$ is a flux contribution. $\boldsymbol{D}_c$ is an order of magnitude larger than $\boldsymbol{D}_s$. Also, the shear-induced dispersion is an anisotropic phenomena. The diffusivity in the velocity gradient direction is about 5 times larger than the vorticity direction.

2.6.3 Constitutive equation for the shear-induced particle flux

The first constitutive equation for the shear-induced dispersion flux was proposed by Phillips et al. (1992) based on the scaling arguments of Leighton and Acrivos (1987b). They considered a suspension of mono-dispersed particles in which the shear-induced dispersion arises only from two-body interactions. The collision frequency of a particle scales with $\dot{\gamma}\phi_h$. Each collision produces a displacement of order a_h, therefore the migration velocity of a single particle will scale with $a_h\dot{\gamma}\phi_h$. The flux of particles will be proportional to the variation in the migration velocity over a distance a_h and to the volume fraction of particles,

$$\boldsymbol{N}_c = -K_c a_h^2 \phi_h \nabla(\dot{\gamma}\phi_h) \ , \tag{2.92}$$

where K_c is the down-gradient diffusivity coefficient and the minus sign indicates that the flux occurs from regions of high to low collision rate. This flux can be divided into two components,

$$\boldsymbol{N}_c = -K_c a_h^2 \phi_h^2 \nabla\dot{\gamma} - K_c a_h^2 \dot{\gamma}\phi_h \nabla\phi_h \ . \tag{2.93}$$

The first term is the hydrodynamic migration by gradient of shear rate and is oriented from regions of high to low shear. The second term is the hydrodynamic dispersion by gradient of concentration and is oriented from regions of high to low concentration. These fluxes will often be in opposite directions, but share the same diffusivity coefficient K_c since they arise from the same mechanism. Another flux mechanism appears due to viscosity gradients in the suspension. This gradient produces a change in the particle doublet's center of rotation and a consequent particle displacement. Again, the collision frequency scales with $\dot{\gamma}\phi_h$, but the particle's flux is proportional to the relative viscosity variation $a_h(\nabla\eta)/\eta$,

$$\boldsymbol{N}_\eta = -K_\eta a_h^2 \dot{\gamma}\phi_h^2 \frac{\nabla\eta_\phi}{\eta_\phi} \ , \tag{2.94}$$

where K_η is the viscosity gradient diffusivity coefficient. Since the suspension's viscosity is a function η_ϕ of the particle's volume fraction, the hydrodynamic dispersion by viscosity gradient can be written in terms of the concentration gradient,

$$\boldsymbol{N}_\eta = -K_\eta a_h^2 \dot{\gamma}\phi_h^2 \frac{1}{\eta_\phi}\frac{d\eta_\phi}{d\phi_h} \nabla\phi_h \ . \tag{2.95}$$

Substituting the shear-induced fluxes (2.93, 2.95) and the Brownian flux (2.88) in the diffusion equation (2.10) results in the constitutive equation proposed by Phillips et al. (1992),

$$\frac{D\phi_h}{Dt} = -\nabla\cdot\left[-\frac{kT}{6\pi\eta_o a_h}\nabla\phi_h - K_c a_h^2\phi_h^2\nabla\dot{\gamma} - K_c a_h^2\dot{\gamma}\phi_h\nabla\phi_h - K_\eta\frac{a_h^2\dot{\gamma}\phi_h^2}{\eta_\phi}\frac{d\eta_\phi}{d\phi_h}\nabla\phi_h\right] \ . \tag{2.96}$$

This equation considers an isotropic diffusion and should be used only in unidirectional flows since experiments show that the shear-induced dispersion is highly anisotropic. A modification of the Phillips et al. (1992) equation was proposed by Krishnan et al. (1996) to take into account a curvature-induced migration flux, which is particularly important in Couette and parallel-plate geometries. However, for capillary flow, this additional term has no influence and can be omitted. In the case of spheroidal particles, we assume the hypothesis that equation (2.96) to be valid if a_h is substituted by the equivalent radius of a sphere with the same volume of the spheroid.

2.6.4 Estimates of the down-gradient diffusivity

The determination of the hydrodynamic down-gradient diffusivity is a difficult task, especially in experimental studies. The variety of interaction mechanisms and the difficulty to control the particle's parameters are the main limitations. Cunha and Hinch (1996) numerically calculated the self and the down-gradient diffusivities for dilute suspensions of rough spheres. For a small surface rugosity ε ($< 10^{-3}$), they obtained an exact correlation for the diffusivity coefficient,

$$K_c = \delta^4(\varepsilon) = \varepsilon^{0.4374}(\ln(1/\varepsilon) + 1.347)^{-0.7012} \ , \tag{2.97}$$

where $\delta(\varepsilon)$ is the streamline displacement associated with the collision between particles of rugosity ε. For values of $\varepsilon > 10^{-3}$, they obtained numerically an approximate correlation of

$$K_c \approx 2.2\varepsilon \ . \tag{2.98}$$

Roure and Cunha (2018) obtained similar results for smooth particles with magnetic dipole interaction. They found that the self-diffusivity is proportional to $\delta^4(\varepsilon)$ if ε is substituted by $Mn^{-5/4}$, where Mn is the ratio between hydrodynamic and magnetic forces. In fact, the theoretical prediction (2.97) can be extended to any small parameter associated with an irreversible particle interaction.

Experimental measurements of the self and the down-gradient diffusivity coefficients presented relatively large values, showing that the shear-induced diffusion must have significant influence on flows with shear gradient. Phillips et al. (1992) obtained a value of $K_c = 0.41$ for the down-gradient diffusivity coefficient in Couette flow. Biemfohr et al. (1993) found for the self-diffusivity coefficient a value of $K_s = 0.023$ with spheroidal particles, while Zarraga and Leighton Jr (2002) obtained a value of $K_s = 0.035$ for nearly smooth spheres. Leighton and Acrivos (1987a) obtained a experimental correlation of $K_s = 0.5\phi_h$ considering only three particles interactions. As for the viscosity gradient diffusivity, Phillips et al. (1992) obtained a diffusivity ratio of $K_c/K_\eta = 0.66$.

The diffusivity coefficients for ferrofluid are particularly difficult to measure since the nanometric particles are too small to be tracked and neither their surface roughness can be characterized. Nevertheless, the diffusivity coefficient can be estimated using the model from Cunha and Hinch (1996). Cryogenic electron microscopy studies by Klokkenburg et al. (2006) show that magnetite nano-particles are very irregular and non-spherical. This is a consequence of the co-precipitation method usually used to produce these particles (Charles, 2002). The particles' size and shape were analyzed from the microscopy images of Klokkenburg et al. (2006), as shown in Figure 2.3. An average aspect ratio of 1.16 is observed for these particles. This value corresponds to an equivalent rugosity of $\varepsilon = 0.16$. Extrapolating the numerical results from Cunha and Hinch (1996), we obtain for the down-gradient diffusivity a value of $K_c = 0.35$. No correlation of the down-gradient diffusivity for non-spherical particles is available in the literature. Nevertheless, the estimative from Cunha and Hinch (1996) model gives a value very close to the experimental measurement of Phillips et al. (1992). Furthermore, the formation of aggregates (Butter et al., 2003) or the use of prismatic particles (Bae et al., 2018) may increase the diffusivity coefficient.

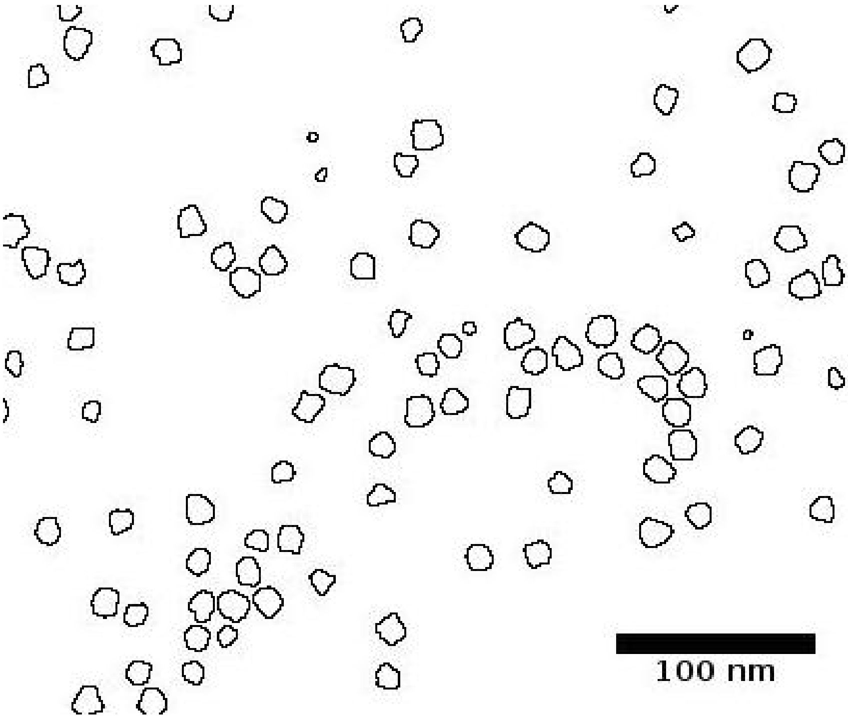

Figure 2.3 – Contours of nanometric magnetite particles. Mean diameter of 12.7 nm and mean roundness coefficient of 0.86. Adapted from cryogenic electron microscopy studies by Klokkenburg et al. (2006).

3 Capillary tube rheology

3.1 Rheology overview

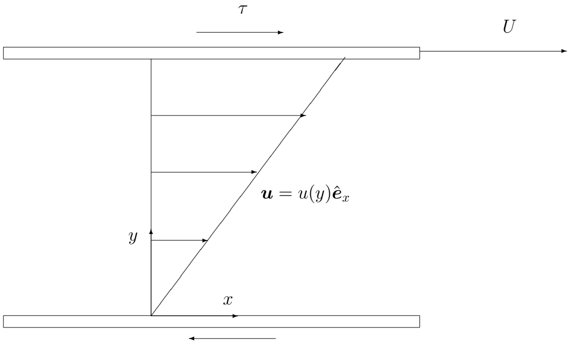

Figure 3.1 – Simple shear between two parallel plates.

Accordingly to Barnes et al. (1989), rheology is the study of deformation and flow of matter. The most basic fluid flow is that in between two shearing parallel plates, as in Figure 3.1. The fluid in the gap will create a resistance to the movement of the plates. For simple fluids, such as water or glycerin, the applied shear stress σ_{yx} will be proportional to the shear rate $\dot{\gamma} = du/dy$,

$$\sigma_{yx} = \eta\dot{\gamma} \ . \tag{3.1}$$

The proportionality parameter η is defined as the dynamic viscosity. For Newtonian fluids, η is independent of the shear rate. However, the main focus of rheology is on non-Newtonian fluids, whose viscosity may vary not only with the shear rate but also with other parameters such as the deformation history and an applied electric or magnetic field. These complex behaviors are a consequence of the fluid's structure, which commonly contains solid particles, drops, or polymers.

An essential sub-area of rheology is the rheometry. It studies the material behavior in reference flows such as the simple shear, oscillatory shear, extensional flow, and capillary flow. Constitutive models can be easily validated in such simple flows and rheometrical material functions can be experimentally measured. As a consequence, rheometry allows for the modeling of industrial processes.

3.2 Capillary flow

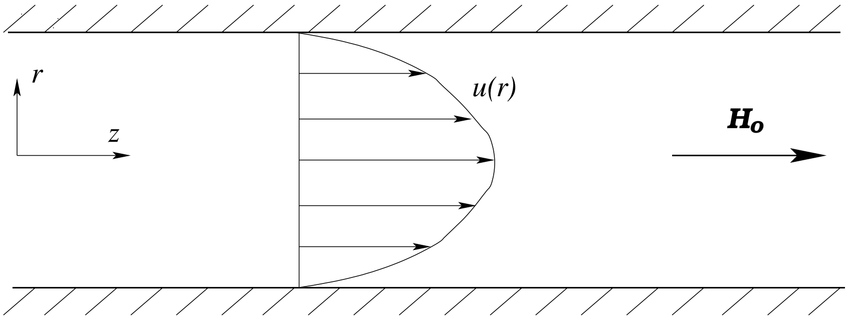

Figure 3.2 – Capillary flow of a magnetic fluid under an applied magnetic field in the velocity direction.

This work focus on the rheometry of magnetic fluids in capillary flow, as in Figure 3.2. This flow is classified as a *pressure-driven flow*, *i.e.*, the source of motion is a pressure gradient. Since there is a shear rate gradient along the radial axis, the magnetic fluid viscosity may also vary.

3.2.1 Unidirectional flow hypothesis

In a capillary tube, under specific conditions, the inertia terms can be neglected and the flow can be treated as unidirectional. We shall obtain the necessary conditions using scaling arguments. The continuity equation (2.5) in axisymmetric coordinates is

$$\frac{1}{r}\frac{\partial(ru_r)}{\partial r}+\frac{\partial u_z}{\partial z}=0\ . \tag{3.2}$$

The typical scales for u_z, r and z are respectively U, the mean velocity, d, the tube diameter, and L, the tube length. From the equation (3.2), the typical length for u_r is

$$u_r\sim U\frac{d}{L}\ . \tag{3.3}$$

If the aspect ratio is sufficiently large ($L/d\gg 1$), the radial velocity is negligible and the flow can be treated as unidirectional. Now, consider the longitudinal component of the Navier-Stokes equation (2.87) without magnetic or transient terms,

$$\rho u_r\frac{\partial u_z}{\partial r}+\rho u_z\frac{\partial u_z}{\partial z}=-\frac{\partial p}{\partial z}+\eta_o\left(\frac{\partial^2 u_z}{\partial r^2}+\frac{1}{r}\frac{\partial u_z}{\partial r}\right)\ . \tag{3.4}$$

The left side of the equation, the convective term, scales with $\rho U^2/L$, while the right side, the diffusive term, scales with $\eta_o U/d^2$. Therefore, the convective term can be neglected if

$$\frac{\rho U^2}{L}<<\frac{\eta_o U}{d^2}\ . \tag{3.5}$$

Rearranging the expression, the unidirectionality condition for the capillary flow is obtained.

$$Re_d \left(\frac{d}{L}\right) << 1 \ , \tag{3.6}$$

where $Re_d = \rho U d/\eta_o$ is the Reynolds number with respect to the tube diameter.

3.2.2 Hagen-Poiseuille law

The canonical flow for a capillary tube is that for a Newtonian fluid in which the condition (3.6) is satisfied. In this flow, the pressure gradient and the flow rate are related by the Hagen-Poiseuille law, which is derived in this section. The force balance in a cylindrical element of differential length dz and radius r is

$$2\pi r \sigma_{rz} dz = -(\pi r^2) dp \Rightarrow \sigma_{rz} = \frac{r}{2} G \ , \tag{3.7}$$

where σ_{rz} is the shear stress at the lateral boundary and $G = -dp/dz$ is the pressure gradient. At the tube wall ($r = d/2$), the shear stress σ_w is

$$\sigma_w = \frac{d}{4} G \ . \tag{3.8}$$

In a capillary flow, the shear rate $\dot{\gamma}$ is given by

$$\dot{\gamma} = -\frac{du_z}{dr} \ . \tag{3.9}$$

The flow rate is evaluated by the integral of the longitudinal velocity,

$$Q = \int_0^{d/2} u_z (2\pi r) dr \ . \tag{3.10}$$

Using integration by parts, the expression (3.10) can be rewritten as

$$Q = \pi \left[u_z r^2 \right]_0^{d/2} - \pi \int_{u_c}^{u_w} r^2 du_z \ . \tag{3.11}$$

The non-slip condition at the wall imposes that $u_z(r = d/2) = 0$. Using the equation (3.9), the integral variable is substituted from u_z to r,

$$Q = \pi \int_0^{d/2} r^2 \dot{\gamma} dr \ . \tag{3.12}$$

Combining the relation (3.1) with (3.7), the shear can be rewritten as

$$\dot{\gamma} = \frac{r}{2\eta} G \ . \tag{3.13}$$

Substituting (3.13) in (3.12) and solving the integral results in the Hagen-Poiseuille law

$$Q = \frac{\pi d^4}{128\eta} G \ . \tag{3.14}$$

Although this equation is only valid for Newtonian fluids, it can be used to define a mean viscosity coefficient for non-Newtonian fluids, named the relative viscosity η_r,

$$\eta_r = \frac{\pi d^4}{128 Q} G \ . \tag{3.15}$$

3.2.3 Weissenberg-Rabinowitsch relation

Non-Newtonian fluids have a non-linear relation between the shear stress and the shear rate. If this relation is not known, the velocity profile in the tube can not be solved. Nevertheless, it still possible to calculate the wall shear rate from the pressure gradient and the flow rate. Combining equations (3.7) and (3.8) the radial coordinate can be rewritten in terms of the shear rate,

$$r = \frac{d}{2}\frac{\sigma_{rz}}{\sigma_w} \Rightarrow dr = \frac{d}{2\sigma_w} d\sigma_{rz} \ . \tag{3.16}$$

Applying this variable change to equation (3.12) results that

$$Q = \frac{\pi d^3}{8\sigma_w^3}\int_0^{\sigma_w} \sigma_{rz}^2 \dot{\gamma} d\sigma_{rz} \ . \tag{3.17}$$

Differentiating this expression with respect to σ_w, and evaluating the expression at $r = d/2$, we obtain an expression for the wall shear rate $\dot{\gamma_w}$,

$$\dot{\gamma_w} = \dot{\gamma}(r = d/2) = \frac{1}{\sigma_w^2}\frac{d}{d\sigma_w}\left(\frac{8\sigma_{rz}^3 Q}{\pi d^3}\right) \ . \tag{3.18}$$

The relation (3.8) is used to introduce the pressure gradient in the expression. After some manipulation, the Weissenberg-Rabinowitsch relation (Bird et al., 1987) for the wall shear rate is obtained,

$$\dot{\gamma_w} = \frac{8Q}{\pi d^3}\left(3 + \frac{d\ln|Q|}{d\ln|\Delta p|}\right) \ . \tag{3.19}$$

where $\Delta p = GL$. This relation is important for experimental measurements, since it allows to evaluate the wall shear rate from a Δp *versus* Q plot. Associated with the expression (3.8), the wall viscosity can be calculated by

$$\eta_w = \frac{\sigma_w}{\dot{\gamma_w}} \ , \tag{3.20}$$

3.3 Modeling of ferrofluid hydrodynamics in capillary flow

In this work, we investigate the flow of ferrofluids in a capillary tube of diameter d under the action of an external longitudinal magnetic field, $\boldsymbol{H_o} = H_o\hat{\boldsymbol{e}}_z$, accordingly to Figure 3.2. The main quantity of focus is the viscosity change due to the magnetoviscous effect and the shear-induced particle migration. The flow is assumed unidirectional, axisymmetric, permanent with no longitudinal gradient of the magnetic field. Therefore, inertial and convective terms can be neglected, and the velocity field is denoted as $\boldsymbol{u} = u(r)\hat{\boldsymbol{e}}_z$.

3.3.1 Magnetostatics

Firstly, the magnetic boundary conditions are specified. The boundary condition (2.25) for $\boldsymbol{B}$ imposes that

$$B_{ext,r} = B_{int,r} \ \Rightarrow \ H_r = -M_r \ , \text{for } r = \frac{d}{2} \ . \tag{3.21}$$

For the magnetic field $\boldsymbol{H}$, the boundary condition 2.27 imposes that

$$H_{ext,t} = H_{int,t} \;\Rightarrow\; H_z = H_o \text{ , for } r = \frac{d}{2} \; . \tag{3.22}$$

Now, the magnetostatics equations are specified for the interior region of the tube. The equation (2.18) in cylindrical coordinates (r,φ,z) is

$$\frac{1}{r}\frac{\partial}{\partial r}(rB_r) + \frac{1}{r}\frac{\partial B_\varphi}{\partial \varphi} + \frac{\partial B_z}{\partial z} = 0 \; . \tag{3.23}$$

Since there is no angular or longitudinal field variation, the equation reduces to

$$H_r = -M_r \text{ , for } r < \frac{d}{2} \; . \tag{3.24}$$

Although the external applied field is uniform and purely longitudinal, there can still be radial field gradient inside the tube. Now, consider the φ-component of the equation (2.23),

$$\frac{\partial H_r}{\partial z} - \frac{\partial H_z}{\partial r} = 0 \; . \tag{3.25}$$

Combined with the boundary condition (3.22), this equation results that

$$H_z = H_o \text{ , for } r < \frac{d}{2} \; . \tag{3.26}$$

3.3.2 Magnetization relaxation equation

The relaxation equation (2.72) without the convective and transient terms has its r and z-components written as,

$$\begin{cases} \dfrac{1}{2}\dot{\gamma}H_{ez} - \dfrac{1}{\tau}(H_{er} - H_r) - \dfrac{\mu_o}{6\eta_o\phi_h\psi_0}(M_rH_{ez}H_o - H_rH_{ez}M_z) = 0 \; , \\ -\dfrac{1}{2}\dot{\gamma}H_{er} - \dfrac{1}{\tau}(H_{ez} - H_o) - \dfrac{\mu_o}{6\eta_o\phi_h\psi_0}(M_zH_{er}H_r - H_zH_{er}M_r) = 0 \; . \end{cases} \tag{3.27}$$

Applying the equations (2.68), (3.24) and (3.26), results that

$$\begin{cases} \dfrac{1}{2}\dot{\gamma}H_{ez} - \dfrac{1}{\tau}H_{er}(1+\chi_e) - \dfrac{\mu_o}{6\eta_o\phi_h\psi_0}\chi_eH_{er}H_{ez}[H_o + \chi_eH_{ez}] = 0 \; , \\ -\dfrac{1}{2}\dot{\gamma}H_{er} - \dfrac{1}{\tau}(H_{ez} - H_o) + \dfrac{\mu_o}{6\eta_o\phi_h\psi_0}\chi_eH_{er}^2[H_o + \chi_eH_{ez}] = 0 \; . \end{cases} \tag{3.28}$$

3.3.3 Modified Navier-Stokes equation

Firstly, we shall analyze the r-component of the equation (2.87),

$$-\frac{\partial p}{\partial r} + \mu_oM_r\frac{\partial H_r}{\partial r} = 0 \; . \tag{3.29}$$

Only the radial pressure gradient and the Kelvin force terms are present. Defining a modified pressure $\tilde{p}$ given by

$$\tilde{p} = p + \frac{\mu_oM_r^2}{2} \; , \tag{3.30}$$

the equation (3.29) can be rewritten as

$$-\frac{\partial \tilde{p}}{\partial r} = 0 \ . \tag{3.31}$$

Therefore, $\tilde{p}$ is a function only of the z-coordinate and equation (3.31) does not inflict on the hydrodynamics of the problem. In this case, the pressure gradient G is

$$G = -\frac{d\tilde{p}}{dz} = -\frac{\partial p}{\partial z} \ . \tag{3.32}$$

Now we write the z-component of the equation (2.87),

$$G - \frac{1}{r}\frac{\partial}{\partial r}\left(\eta_o r\dot{\gamma} + r\overline{S}_{rz}\right) - \frac{\mu_o}{2}\frac{1}{r}\frac{\partial}{\partial r}\left(rM_rH_z - rH_rM_z\right) = 0 \ . \tag{3.33}$$

Applying the equations (2.68), (3.24) and (3.26), results that

$$G - \frac{1}{r}\frac{\partial}{\partial r}\left(\eta_o r\dot{\gamma} + r\overline{S}_{rz}\right) - \frac{\mu_o}{2}\frac{1}{r}\frac{\partial}{\partial r}\left(r\chi_e H_{er}H_o + r\chi_e^2 H_{er}H_{ez}\right) = 0 \ . \tag{3.34}$$

This equation can be simplified multiplying by r and integrating over this coordinate.

$$\frac{rG}{2} - \eta_o\dot{\gamma} - \overline{S}_{rz} - \frac{\mu_o}{2}\chi_e H_{er}\left(H_o + \chi_e H_{ez}\right) = 0 \ . \tag{3.35}$$

3.3.4 Diffusion equation

The diffusion equation (2.96) in axisymmetric coordinates and without convective terms is

$$\frac{1}{r}\frac{\partial}{\partial r}\left[\frac{2kT}{9\eta_o v_h}\frac{\partial \phi_h}{\partial r} + \phi_h^2 K_c\frac{\partial \dot{\gamma}}{\partial r} + \phi_h\dot{\gamma}K_c\frac{\partial \phi_h}{\partial r} + \phi_h^2\dot{\gamma}K_\eta\frac{1}{\eta_\phi}\frac{\partial \eta_\phi}{\partial r}\right] = 0 \ . \tag{3.36}$$

Again, this equation can be simplified multiplying by r and integrating over this coordinate.

$$\frac{2kT}{9\eta_o v_h}\frac{d\phi_h}{dr} + \phi_h^2 K_c\frac{d\dot{\gamma}}{dr} + \phi_h\dot{\gamma}K_c\frac{d\phi_h}{dr} + \phi_h^2\dot{\gamma}K_\eta\frac{1}{\eta_\phi}\frac{d\eta_\phi}{d\phi_h}\frac{d\phi_h}{dr} = 0 \ . \tag{3.37}$$

3.3.5 Boundary and integral conditions

Complementary to the balance equations (3.35),(3.28) and (3.37), three boundary or integral conditions are necessary to obtain a well-posed system. The first condition is the non-slip at the tube wall,

$$u\left(r = \frac{d}{2}\right) = 0 \ , \tag{3.38}$$

Since the mean velocity is an imposed parameter, the velocity field must satisfy the mean velocity defition,

$$\overline{u} = \frac{4}{\pi d^2}\int_0^{\frac{d}{2}} u(r)2\pi r dr. \tag{3.39}$$

The same integral conditions is applied to the mean volume fraction,

$$\overline{\phi}_h = \frac{4}{\pi d^2}\int_0^{\frac{d}{2}} \phi_h(r)2\pi r dr. \tag{3.40}$$

3.4 Non-dimensional governing equations

In order to identify the main physical parameters of the problem, the governing equations are made non-dimensional. In a capillary flow, the typical length is the tube diameter d, while the typical velocity is the mean value U. For the magnetization and the magnetic field, the typical scales are the fluid's saturation magnetization (for the homogeneous volume fraction) M_s and the applied field H_o, respectively. Since the flow is assumed unidirectional (see section 3.2.1), the typical pressure gradient scale is the viscous scale $\eta_o U/d^2$. For the shear rate, the typical scale is chosen as the Poiseuille wall shear rate $\dot{\gamma}_c = 8U/d$. The typical viscosity scale is the carrier fluid viscosity η_o. Using these typical scales, the non-dimensional variables (denoted with an $*$) are defined as

$$G^* = \frac{Gd^2}{\eta_o U} \ ; \ \eta^* = \frac{\eta}{\eta_o} \ ; \ r^* = \frac{r}{d} \ ; \ \dot{\gamma}^* = \frac{\dot{\gamma} d}{8U} \ ; \ u^* = \frac{u}{U} \ ; \ \boldsymbol{M}^* = \frac{\boldsymbol{M}}{M_s} \ ; \ \boldsymbol{H}_e^* = \frac{\boldsymbol{H}_e}{H_o} \ . \tag{3.41}$$

The volume fraction, the magnetic susceptibility, the diffusivity coefficient, and the aspect ratio are already non-dimensional quantities.

3.4.1 Spherical particles

Applying the non-dimensional variables (3.41) to equations (3.35),(3.28) and (3.37) results in the following non-dimensional governing system for spherical particles (omitting the $*$),

$$\begin{cases} Gr - 16(1+2.5\phi_h)\dot{\gamma} - 8\dfrac{\phi_h \alpha_o^2}{Pe}\dfrac{\chi_e}{\chi_i} H_{er}(1+\chi_e H_{ez}) = 0 \ , \\ \dot{\gamma} H_{ez} - \dfrac{2}{Pe}(1+\chi_e)H_{er} - \dfrac{\alpha_o^2}{3Pe}\dfrac{\chi_e}{\chi_i} H_{er}H_{ez}(1+\chi_e H_{ez}) = 0 \ , \\ \dot{\gamma} H_{er} - \dfrac{2}{Pe}(1-H_{ez}) - \dfrac{\alpha_o^2}{3Pe}\dfrac{\chi_e}{\chi_i} H_{er}^2(1+\chi_e H_{ez}) = 0 \ , \\ \left(\dfrac{2}{3Pe} + K_c\phi_h\dot{\gamma} + \dfrac{K_\eta \phi_h^2 \dot{\gamma}}{\eta_\phi}\dfrac{d\eta_\phi}{d\phi_h}\right)\dfrac{d\phi_h}{dr} + \phi_h^2 K_c \dfrac{d\dot{\gamma}}{dr} = 0 \ , \\ \dfrac{du}{dr} = -8\dot{\gamma} \ . \end{cases} \tag{3.42}$$

Notice that the shear rate definition (3.9) must also be made non-dimensional, and it corresponds to the 5-th equation of the governing system (3.42). The non-dimensional boundary and integral conditions are

$$\begin{cases} u\left(\dfrac{1}{2}\right) = 0 \ , \\ 1 = 8\displaystyle\int_0^{1/2} ur \ dr \ , \\ \overline{\phi}_h = 8\displaystyle\int_0^{1/2} \phi_h r \ dr \ . \end{cases} \tag{3.43}$$

The physical non-dimensional parameters identified in the system (3.42) are the Péclet number Pe and the global Langevin parameter α_o. The Péclet number represents the ratio between the Brownian and convective time scales, and is defined by

$$Pe = \frac{4\pi\eta_o a_h^3 \dot{\gamma}_c}{kT} \ . \tag{3.44}$$

Most parameters in the Péclet definition are either physical constants or determined by the ferrofluid sample, except for the shear rate, that can be more easily controlled. Therefore, the Péclet number can be interpreted as a non-dimensional measure of the shear rate intensity. The Péclet number is a global parameter,*i.e.* it does not depend on the r-coordinate. Since in a capillary flow the shear rate varies in the radial direction, the convective time scale changes. It is possible to define a local Péclet number, given by

$$Pe_l(r) = Pe\dot{\gamma}(r) \ . \tag{3.45}$$

Evaluating the local Péclet number at the tube wall, we define the wall Péclet number,

$$Pe_w = Pe\dot{\gamma}_w \ , \tag{3.46}$$

where $\dot{\gamma}_w$ is the non-dimensional wall shear rate.

The second non-dimensional physical parameter in the system (3.42) is the global Langevin parameter α_o, defined by

$$\alpha_o = \frac{\mu_o m H_o}{kT} = \frac{4\mu_o \pi a_m^3 M_d H_o}{3kT} \ . \tag{3.47}$$

Again, the only easily controllable parameter is the applied magnetic field intensity, therefore α_o is a non-dimensional measure of the field intensity. The effective local (r-dependent) Langevin number, $\alpha_e(r)$, is related to the global parameter by

$$\alpha_e(r) = \alpha_o H_e(r) \ . \tag{3.48}$$

The magnetic susceptibility for the effective field, χ_e, can be written in terms of the local magnetic volume fraction ϕ_m, the local effective Langevin parameter α_e and the dipole interaction parameter λ,

$$\chi_e = \frac{24\phi_m \lambda \mathcal{L}(\alpha_e)}{\alpha_o H_e} \ . \tag{3.49}$$

The initial Langevin susceptibility is given by

$$\chi_i = 8\phi_m \lambda \ . \tag{3.50}$$

The hydrodynamic and magnetic volume fractions are variables and may vary locally. However, they are related by a fixed ratio $\phi_m/\phi_h = \overline{\phi}_m/\overline{\phi}_h$. The dipolar interaction parameter is defined by

$$\lambda = \frac{\mu_o \pi a_m^3 M_d^2}{18kT} \ , \tag{3.51}$$

and is the ratio between magnetic dipole forces and the Brownian force. This parameter is a function exclusively of the particle's characteristics. Therefore, it is more convenient to consider λ as an input parameter, rather than χ_i. The dipolar interaction parameter must be kept small ($\lambda \leq 1$) so that inter-particle magnetic forces can be neglected.

The parameters α_o, Pe and λ scale with the particle's volume, since they are all related to Brownian forces. Therefore, it is clear that the particle's size can greatly change the rheological characteristics of a ferrofluid.

From equations (3.15) and (3.20), the non-dimensional relative and wall viscosity are (omitting the $*$).

$$\eta_r = \frac{G}{32} \ , \tag{3.52}$$

and

$$\eta_w = \frac{\eta_r}{\dot{\gamma}_w} \ , \tag{3.53}$$

3.4.2 Ellipsoidal particles

Now, we develop the non-dimensional governing system for spheroidal particles. The magnetic dipole $\boldsymbol{m}$ is fixed on the major axis orientation of the particle. The dipole-dipole particle interactions are neglected. The spheroids have a fixed hydrodynamic (magnetic) minor axis a_h (a_m) equal to the radius of the spheres, and a major axis $b_h = a_h\beta$ ($b_m = a_m\beta$). In this case, the volume of the spheroid is proportional to β. As a consequence, the effective local Langevin parameter is scaled by β with respect to the value for spheres,

$$\alpha_e(r) = \alpha_o \beta H_e(r) \ . \tag{3.54}$$

The global non-dimensional numbers (Pe, α_o, λ) are still defined by the expressions (3.44),(3.47), and (3.51), so that they remain independent of β. The down-gradient diffusivity K_c is calculated with the correlations (2.97) and (2.98), with $\varepsilon = \beta - 1$ being an equivalent rugosity. Although the spheroid volume scales with β, the density number scales with $1/\beta$ to keep the mean hydrodynamic and magnetic volume fractions, $\overline{\phi}_h$ and $\overline{\phi}_m$, independent of β. The non-dimensional governing system for spheroidal particles is

$$\begin{cases} Gr - 16\dot{\gamma} + 16\overline{S}_{rz} - 8\dfrac{\phi_h \alpha_o^2}{Pe}\dfrac{\chi_e}{\chi_i} H_{er}(1 + \chi_e H_{ez}) = 0 \ , \\ \psi_0 \dot{\gamma} H_{ez} - \dfrac{2}{Pe}\dfrac{1 + \chi_e}{\beta} H_{er} - \dfrac{\alpha_o^2}{3Pe}\dfrac{\chi_e}{\chi_i} H_{er} H_{ez}(1 + \chi_e H_{ez}) = 0 \ , \\ \psi_0 \dot{\gamma} H_{er} - \dfrac{2}{Pe}\dfrac{1 - H_{ez}}{\beta} - \dfrac{\alpha_o^2}{3Pe}\dfrac{\chi_e}{\chi_i} H_{er}^2 (1 + \chi_e H_{ez}) = 0 \ , \\ \left(\dfrac{2}{3Pe\beta} + K_c \phi_h \dot{\gamma} + \dfrac{K_\eta \phi_h^2 \dot{\gamma}}{\eta_\phi}\dfrac{d\eta_\phi}{d\phi_h} \right) \dfrac{d\phi_h}{dr} + \phi_h^2 K_c \dfrac{d\dot{\gamma}}{dr} = 0 \ , \\ \dfrac{du}{dr} = -8\dot{\gamma} \ , \\ \overline{S}_{rz} = -\dfrac{5\phi_h \dot{\gamma}}{2} \left[\psi_1 + \psi_2(\langle n_z n_z \rangle + \langle n_r n_r \rangle) + 2\psi_3 \langle n_r n_z n_r n_z \rangle + \psi_4(\langle n_z n_z \rangle - \langle n_r n_r \rangle) \right] \ . \end{cases} \tag{3.55}$$

The boundary and integral conditions (4.2) remain unchanged. The expressions for the order moments are given in the Appendix B and are a function of α_e.

The table (1) summarizes the physical non-dimensional parameters definitions.

Table 1 – Physical non-dimensional parameters

Parameter	**Definition**
Global Langevin parameter	$\alpha_o = \dfrac{4\mu_o \pi a_m^3 M_d H_o}{3kT}$
Péclet number	$Pe = \dfrac{4\pi\eta_o a_h^3 \dot{\gamma}_c}{kT}$
Mean magnetic volume fraction	$\overline{\phi}_m = \overline{n} v_m$
Mean hydrodynamic volume fraction	$\overline{\phi}_h = \overline{n} v_h$
Dipolar interaction parameter	$\lambda = \dfrac{\mu_o \pi a_m^3 M_d^2}{18kT}$
Langevin initial susceptibility*	$\chi_i = 8\phi_m \lambda$

*The Langevin initial susceptibility is not an independent parameter, but rather a function of the previous parameters.

4 Numerical Procedure

The numerical procedure used to solve the adopted models will be discussed in this chapter. The sets of governing equations for the model of rough spheres and of spheroids have the same structure. Therefore, the procedure for both models is identical and will be explained only for the first model,

$$\begin{cases} Gr - 16(1+2.5\phi_h)\dot{\gamma} - 8\dfrac{\phi_h \alpha_o^2}{Pe}\dfrac{\chi_e}{\chi_i}H_{er}(1+\chi_e H_{ez}) = 0 \ , \\ \dot{\gamma}H_{ez} - \dfrac{2}{Pe}(1+\chi_e)H_{er} - \dfrac{\alpha_o^2}{3Pe}\dfrac{\chi_e}{\chi_i}H_{er}H_{ez}(1+\chi_e H_{ez}) = 0 \ , \\ \dot{\gamma}H_{er} - \dfrac{2}{Pe}(1-H_{ez}) - \dfrac{\alpha_o^2}{3Pe}\dfrac{\chi_e}{\chi_i}H_{er}^2(1+\chi_e H_{ez}) = 0 \ , \\ \left(\dfrac{2}{3Pe} + K_c\phi_h\dot{\gamma} + \dfrac{K_\eta \phi_h^2 \dot{\gamma}}{\eta_\phi}\dfrac{d\eta_\phi}{d\phi_h}\right)\dfrac{d\phi_h}{dr} + \phi_h^2 K_c \dfrac{d\dot{\gamma}}{dr} = 0 \ , \\ \dfrac{du}{dr} = -8\dot{\gamma} \ . \end{cases} \tag{4.1}$$

This system is one-dimensional, stationary, first order and non linear. The space dependent variables are $u(r)$, $\dot{\gamma}(r)$, $\phi_h(r)$, $H_{er}(r)$ and $H_{ez}(r)$, while G is a global variable. Only the first derivatives of u, $\dot{\gamma}$, ϕ_h are present, thus requiring three additional boundary or integral conditions to obtain a well-posed problem. This conditions are

$$\begin{cases} u\left(\dfrac{1}{2}\right) = 0 \ , \\ 1 = 8\displaystyle\int_0^{1/2} ur \ dr \ , \\ \bar{\phi}_h = 8\displaystyle\int_0^{1/2} \phi_h r \ dr \ . \end{cases} \tag{4.2}$$

A numerical scheme was developed in order to solve the governing. It consists of a combination of two Newton-Raphson methods for non-linear algebraic systems, a second order Euler method and a trapezoidal integration. The procedure is described in the following sections.

4.1 Initial guess and domain discretization

Firstly, the spatial domain ($0 \leq r \leq 0.5$) is discretized into N intervals, which leads to a sequence $\{r_i\}$ of $N+1$ points. Then, an initial guess for G and the wall volume fraction ϕ_{hw} are given. This values are set as $G = 32(1 + 2.5\bar{\phi}_h)$ and $\phi_{hw} = \bar{\phi}_h$, which is the solution in the limits of $Pe = 0$ and $\alpha_o = 0$.

4.2 First Newton-Raphson method for the effective field components and the shear rate

The first three equations of the system (4.1) are non linear algebraic equations. If the values of G and ϕ_h are given, this equations can be solved for H_{er}, H_{ez} and $\dot{\gamma}$, for a fixed point r. This is done via a Newton-Raphson method for non linear systems. The variables array $\boldsymbol{x}$ is

$$\boldsymbol{x} = [\dot{\gamma}\ H_{er}\ H_{ez}] \ , \tag{4.3}$$

and the system solution is the rot of the functions array $\boldsymbol{f}(\boldsymbol{x})$, *i.e.*,

$$\boldsymbol{f}(\boldsymbol{x}) = \boldsymbol{0} \ . \tag{4.4}$$

Here, $\boldsymbol{f}(\boldsymbol{x}) = (f_1(\boldsymbol{x})\ f_2(\boldsymbol{x})\ f_3(\boldsymbol{x}))$ is given by the first three equations of the system (4.1):

$$\begin{cases} f_1(\boldsymbol{x}) = Gr - 16(1 + 2.5\phi_h)\dot{\gamma} - 24\dfrac{\phi_h \alpha_o}{Pe}\dfrac{\mathcal{L}(\alpha_o H_e)H_{er}}{H_e}(1 + \chi_e H_{ez}) \ , \\ f_2(\boldsymbol{x}) = \dot{\gamma}H_{ez} - \dfrac{2}{Pe}(1 + \chi_e)H_{er} - \dfrac{\alpha_o}{Pe}\dfrac{\mathcal{L}(\alpha_o H_e)H_{er}H_{ez}}{H_e}(1 + \chi_e H_{ez}) \ , \\ f_3(\boldsymbol{x}) = \dot{\gamma}H_{er} - \dfrac{2}{Pe}(1 - H_{ez}) - \dfrac{\alpha_o}{Pe}\dfrac{\mathcal{L}(\alpha_o H_e)H_{er}^2}{H_e}(1 + \chi_e H_{ez}) \ . \end{cases} \tag{4.5}$$

The initial guess for the variables array $\boldsymbol{x}_o$ is set as a parabolic velocity profile $\dot{\gamma} = 2r$ and the equilibrium effective field $H_{er} = 0$ and $H_{ez} = 1$. The Newton-Raphson method is based on the following linear approximation,

$$\boldsymbol{f}(\boldsymbol{x}') \approx \boldsymbol{f}(\boldsymbol{x}_o) + \boldsymbol{J}(\boldsymbol{x}_o) \cdot (\boldsymbol{x}' - \boldsymbol{x}_o) \ , \tag{4.6}$$

where $\boldsymbol{J}(\boldsymbol{x})$ is the Jacobian matrix of $\boldsymbol{f}(\boldsymbol{x})$. If $\boldsymbol{f}(\boldsymbol{x}')$ is set equal 0, then a correction $\boldsymbol{\Delta x}$ can be calculated via the linear system:

$$\boldsymbol{J}(\boldsymbol{x}_k) \cdot \boldsymbol{\Delta x} = -\boldsymbol{f}(\boldsymbol{x}_k) \ , \tag{4.7}$$

and the following step is given by

$$\boldsymbol{x}_{k+1} = \boldsymbol{x}_k + \boldsymbol{\Delta x} \ . \tag{4.8}$$

The 3x3 linear system (4.7) is solved analytically. The process is repeated iteratively until the correction is smaller than a tolerance,

$$m\acute{a}x|\boldsymbol{\Delta x}| < \frac{10^{-2}}{N} \ . \tag{4.9}$$

4.3 Euler method

At the wall $r = 0.5$, the velocity and the volume fraction are defined by the boundary condition $u(0.5) = 0$ and the initial guess $\phi_h(0.5) = \phi_{hw}$. The velocity and volume fraction profiles can be calculated from the differential equations in the system (4.1) using a second-order Euler method. This differential equations can be rewritten as:

$$\begin{cases} \dfrac{d\phi_h}{dr} = f_1\left(\phi_h\right) = -\phi_h^2 K_c \dfrac{d\dot{\gamma}}{dr}\left(\dfrac{2}{3Pe} + K_c\phi_h\dot{\gamma} + \dfrac{K_\eta \phi_h^2 \dot{\gamma}}{\eta_\phi}\dfrac{d\eta_\phi}{d\phi_h}\right)^{-1} \;, \\ \dfrac{du}{dr} = f_2(\phi_h) = -8\dot{\gamma} \;. \end{cases} \tag{4.10}$$

The values for the shear rate $\dot{\gamma}$ are calculated using the first Newton-Raphson method described in the preceding section, which requires as input values only ϕ_h and G. The derivative of the shear rate is calculated using a differential increment over a small step of $0.1h$:

$$\frac{d\dot{\gamma}}{dr}(r_i) = \frac{\dot{\gamma}(r_i + 0.1h) - \dot{\gamma}(r_i)}{0.1h} \;, \tag{4.11}$$

where $h = r_{i+1} - r_i$ is the interval length. Starting from the wall, the velocity and the volume fraction are calculated at each domain point r_i using the following iterative procedure:

$$\begin{cases} \phi_h' = \phi_h[i+1] - hf_1(\phi_h[i+1]) \;, \\ \phi_h[i] = \phi_h[i+1] - h(f_1(\phi_h[i+1]) + f_1(\phi_h'))/2 \;, \\ u[i] = u[i+1] - h(f_2(\phi_h[i+1]) + f_2(\phi_h'))/2 \;. \end{cases} \tag{4.12}$$

4.4 Second Newton-Raphson method for the pressure gradient and wall volume fraction

Once the velocity and volume fraction profiles have been computed, the integral conditions 4.2 must be verified and the values for G and ϕ_{hw} must be corrected. This is done using a second Newton-Raphson method, with the variable array given by

$$\boldsymbol{x} = [G \; \phi_{hw}] \;, \tag{4.13}$$

and the function array given by

$$\begin{cases} f_1(\boldsymbol{x}) = 1 - 8\displaystyle\int_0^{1/2} ur \; dr \;, \\ f_2(\boldsymbol{x}) = \bar{\phi}_h - 8\displaystyle\int_0^{1/2} \phi_h r \; dr \;. \end{cases} \tag{4.14}$$

The integrals are computed using a trapezoidal scheme. The system's root provides the correct values for G and ϕ_{hw}.

4.5 Convergence of domain discretization

In order to set the number of intervals in the domain discretization, a convergence diagram was plotted in Figure 4.1. The relative viscosity was calculated for various domain discretizations and fixed moderate values for the non-dimensional parameters. For $N \geq 500$, no variation higher than 10^{-6} was observed for the viscosity. Therefore, the value $N = 500$ was set as the default for the simulations in this work.

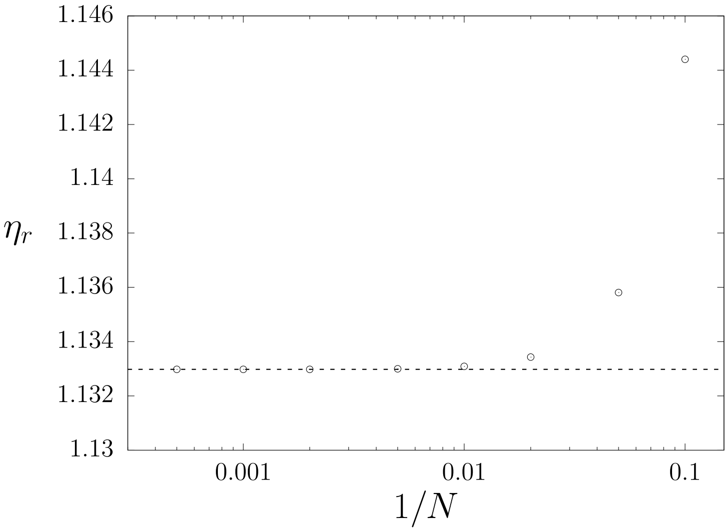

Figure 4.1 – Relative viscosity as a function of the inverse of the number of intervals in the domain. $\alpha_o = 1$, $Pe = 1$, $\lambda = 1$, $K_c = 1$, $K_\eta = 1$, $\bar{\phi}_h = \bar{\phi}_m = 0.05$.

4.6 Numerical scheme

A summary is presented in table 2. The scheme was implemented in Fortran 90, with an user interface on Python for post-processing.

Table 2 – Numerical scheme.

```
1 -  Initial guess for $G$, $\phi_{hw}$
2 -  i = N
3 -  $[u(r_i)\ \dot{\gamma}(r_i)\ \phi_h(r_i)\ H_{er}(r_i)\ H_{ez}(r_i)] \leftarrow$ Newton-Raphson
4 -  $[u(r_{i-1})\ \dot{\gamma}(r_{i-1})\ \phi_h(r_{i-1})] \leftarrow$ Euler
5 -  $i \leftarrow i - 1$
6 -  Back to Step 3 until $i = 0$
7 -  $[\bar{u}\ \bar{\phi}_h] \leftarrow$ Trapezoidal integration
8 -  If integral conditions is satisfied, go to step 11
9 -  $[G_{k+1}\ \phi_{hw,k+1}] \leftarrow$ Newton-Raphson
10 - k $\leftarrow k + 1$
11 - $\eta_r/\eta_o \leftarrow G/32$
12 - $\eta_w \leftarrow \tau_w/\dot{\gamma}_w$
13 - END
```

5 Numerical Resuts and Asymptotic Solutions

In this chapter, we present the numerical results for the magnetoviscous effect in the capillary flow, as well as the magnetization and volume fraction profiles. Two models are investigated: one suspension composed of rough spherical particles and another composed of smooth spheroids. The influence of the physical non-dimensional parameters, the diffusivity coefficients, and the mean volume fraction are investigated. A regular perturbation method is used to obtain asymptotic solutions for spherical particles in the limits of low and high Péclet number without hydrodynamic dispersion, and in the limit of low Péclet with hydrodynamic dispersion. These asymptotic solutions are used to validate the numerical results. In this chapter, the relative viscosity increase is denoted as $\Delta\eta_r = \eta_r - (1 + 2.5\overline{\phi}_h)$ and represents the increase with respect to the ordinary homogeneous suspension of spheres ($\alpha_o = Pe = \beta - 1 = 0$).

5.1 Validation of results for spherical particles in the absence of hydrodynamic dispersion

The numerical investigation of the magnetoviscous effect of a homogeneous suspension made of non-interacting magnetic spherical particles is well known in the literature. For a constant Péclet number, an increase in the applied field produces an increase of the relative viscosity with respect to the ordinary suspension's viscosity, as presented in the Figure 5.1. The global Langevin parameter α_o represents the ratio of magnetic to Brownian forces. With a higher value of α_o, more particles will be aligned with the field and thus contribute to the viscous dissipation. The relative viscosity increases until the fluid saturates and no further increment occurs.

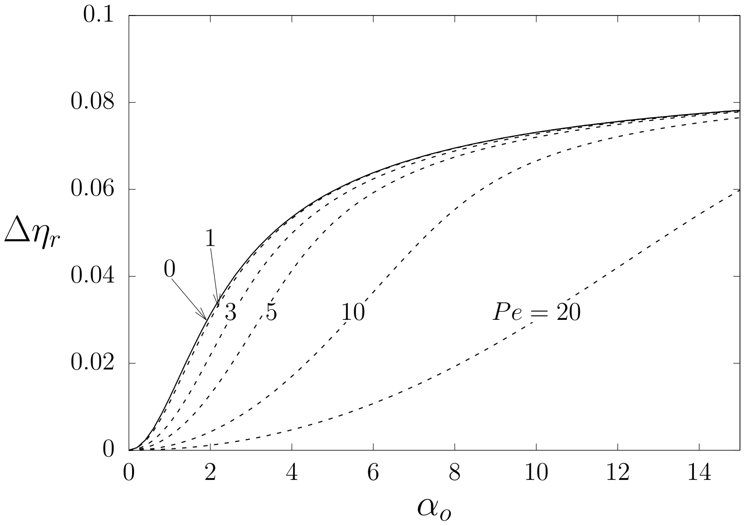

Figure 5.1 – Relative viscosity increase as a function of the global Langevin parameter for various values of Pe without hydrodynamic dispersion. $\lambda = 1$, $\overline{\phi}_h = \overline{\phi}_m = 0.05$, $K_c = 0$.

For a fixed value of α_o, a strong shear-thinning effect is observed with an increase in the Péclet number. In this condition, the hydrodynamic torque outcomes the magnetic one, causing a viscous dissipation reduction. Figure 5.2 shows the relative viscosity increase as a function of the Péclet number.

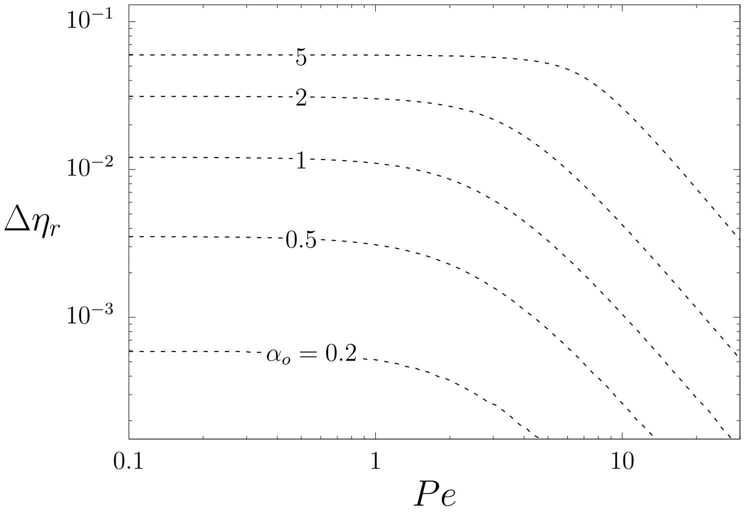

Figure 5.2 – Relative viscosity increase as a function of the Péclet number for various values of α_o without hydrodynamic dispersion. $\lambda = 1$, $\overline{\phi}_h = \overline{\phi}_m = 0.05$, $K_c = 0$.

5.1.1 Asymptotic solutions

The set of governing equations (3.42) does not have an analytical solution for the whole range of parameters. Nevertheless, asymptotic solutions were calculated in Sinzato and Cunha (2020) for the regimes of very low or very high Péclet number and no hydrodynamic dispersion. Obtained from a regular perturbation method (Hinch, 1991), these solutions provide a validation for the numerical results. These asymptotic solutions are derived as follows, with a few differences of notation in relation to calculations in Sinzato and Cunha (2020).

Consider the set of governing equations (3.42) in the absence of hydrodynamic dispersion.

$$\begin{cases} Gr - 16(1+2.5\phi_h)\dot{\gamma} - 8\dfrac{\phi_h\alpha_o^2}{Pe}\dfrac{\chi_e}{\chi_i}H_{er}(1+\chi_e H_{ez}) = 0 \ , \\ \dot{\gamma}H_{ez} - \dfrac{2}{Pe}(1+\chi_e)H_{er} - \dfrac{\alpha_o^2}{3Pe}\dfrac{\chi_e}{\chi_i}H_{er}H_{ez}(1+\chi_e H_{ez}) = 0 \ , \\ \dot{\gamma}H_{er} - \dfrac{2}{Pe}(1-H_{ez}) - \dfrac{\alpha_o^2}{3Pe}\dfrac{\chi_e}{\chi_i}H_{er}^2(1+\chi_e H_{ez}) = 0 \ , \\ \dfrac{du}{dr} = -8\dot{\gamma} \ . \end{cases} \tag{5.1}$$

In the limit of $Pe = 0$, the solution for this system is:

$$\begin{cases} H_{er}(r) = 0 \ , \\ H_{ez}(r) = 1 \ . \end{cases} \tag{5.2}$$

Assuming that $H_{er} \sim Pe$, we may propose a rescaling: $H_{er} = \tilde{H}_{er}Pe$. Rewriting the system (5.1), results that:

$$\begin{cases} Gr - 16(1+2.5\phi_h)\dot{\gamma} - 8\phi_h\alpha_o^2\dfrac{\chi_e}{\chi_i}\tilde{H}_{er}(1+\chi_e H_{ez}) = 0 \ , \\ \dot{\gamma}H_{ez} - 2(1+\chi_e)\tilde{H}_{er} - \dfrac{\alpha_o^2}{3}\dfrac{\chi_e}{\chi_i}\tilde{H}_{er}H_{ez}(1+\chi_e H_{ez}) = 0 \ , \\ Pe^2\left[\dot{\gamma}\tilde{H}_{er} - \dfrac{\alpha_o^2}{3}\dfrac{\chi_e}{\chi_i}\tilde{H}_{er}^2(1+\chi_e H_{ez})\right] - 2(1-H_{ez}) = 0 \ , \\ \dfrac{du}{dr} = -8\dot{\gamma} \ . \end{cases} \tag{5.3}$$

Notice in the 3$^{\text{rd}}$ equation of the system (5.3) the presence of the non-dimensional parameter $\epsilon = Pe^2$. If this parameter is sufficiently small ($\epsilon \ll 1$), then the variables may be written as a polynomial expansion of ϵ.

$$\begin{cases} G = G_0 + \epsilon G_1 + \mathcal{O}(\epsilon^2) \ , \\ u = u_0 + \epsilon u_1 + \mathcal{O}(\epsilon^2) \ , \\ \dot{\gamma} = \dot{\gamma}_0 + \epsilon\dot{\gamma}_1 + \mathcal{O}(\epsilon^2) \ , \\ \tilde{H}_{er} = \tilde{H}_{er0} + \epsilon\tilde{H}_{er1} + \mathcal{O}(\epsilon^2) \ , \\ H_{ez} = H_{ez0} + \epsilon H_{ez1} + \mathcal{O}(\epsilon^2) \ . \end{cases} \tag{5.4}$$

Applying these expansions in the system (5.3) and equating the polynomial coefficients, we obtain a system for each set of variables (order ϵ^0: (G_0,u_0,$\dot{\gamma}_0$,$\tilde{H}_{er0}$,H_{ez0}) and order ϵ^1:(G_1,u_1,$\dot{\gamma}_1$,$\tilde{H}_{er1}$,H_{ez1})). Also, the boundary and integral conditions must be rewritten for each set of variables:

$$\begin{cases} u_0\left(\dfrac{1}{2}\right) = u_1\left(\dfrac{1}{2}\right) = 0 \ , \\ 8\displaystyle\int_0^{\frac{1}{2}} u_0(r) r dr = 1 \ , \ 8\displaystyle\int_0^{\frac{1}{2}} u_1(r) r dr = 0 \ . \end{cases} \tag{5.5}$$

We simplify the effective susceptibility as $\chi_e \approx \chi_o \equiv \chi_e(\alpha_o)$. Solving the systems of order ϵ^0 and ϵ^1, the resulting solutions are:

$$\begin{cases} H_{er}(r) = Pe\dfrac{6\chi_i r}{(1+\chi_o)(6\chi_i+\alpha_o^2\chi_o)} + \mathcal{O}(Pe^3) \ , \\ H_{ez}(r) = 1 - Pe^2\dfrac{36\chi_i^2 r^2}{(1+\chi_o)(6\chi_i+\alpha_o^2\chi_o)^2} + \mathcal{O}(Pe^4) \ , \\ G = 32(1+2.5\overline{\phi}_h) + 48\dfrac{\overline{\phi}_h\alpha_o^2\chi_o}{(6\chi_i+\alpha_o^2\chi_o)} - 8Pe^2\dfrac{\overline{\phi}_h\alpha_o^2(6\chi_i)^3(1+2\chi_o)}{(6\chi_i+\alpha_o^2\chi_o)^4(1+\chi_o)^2} + \mathcal{O}(Pe^4) \ , \\ \dot{\gamma}(r) = 2r + Pe^2\dfrac{\overline{\phi}_h\alpha_o^2(6\chi_i)^3(1+2\chi_o)(6r^3-r)}{(6\chi_i+\alpha_o^2\chi_o)^3(1+\chi_o)^2(2(1+2.5\overline{\phi}_h)(6\chi_i+\alpha_o^2\chi_o)+3\overline{\phi}_h\alpha_o^2\chi_o)} + \mathcal{O}(Pe^4) \ . \end{cases} \tag{5.6}$$

From equation (3.52), the relative viscosity asymptotic solution in the limit of low Pe is

$$\eta_r = \eta_\phi + \eta_s - Pe^2 C_m + \mathcal{O}(Pe^4) \ , \tag{5.7}$$

where $\eta_\phi = 1 + 2.5\overline{\phi}_h$ and η_s is the viscosity increase predicted by Shliomis (1971) for $Pe = 0$, given by,

$$\eta_s = \frac{3}{2}\frac{\overline{\phi}_h\alpha_o^2\chi_o}{(6\chi_i+\alpha_o^2\chi_o)} \ , \tag{5.8}$$

and C_m is the correction order $\mathcal{O}(Pe^2)$, given by

$$C_m = \frac{\overline{\phi}_h\alpha_o^2}{24}\frac{\chi_o}{\chi_i}\left(\frac{6\chi_i}{6\chi_i+\alpha_o^2\chi_o}\right)^4\frac{1+2\chi_o}{(1+\chi_o)^2} \ . \tag{5.9}$$

Figure 5.3 presents a comparison between the numerical and analytical solutions for the relative viscosity in the region of low Péclet number. There is an agreement between the results up to $Pe = 1.5$, with less than 5 % of difference.

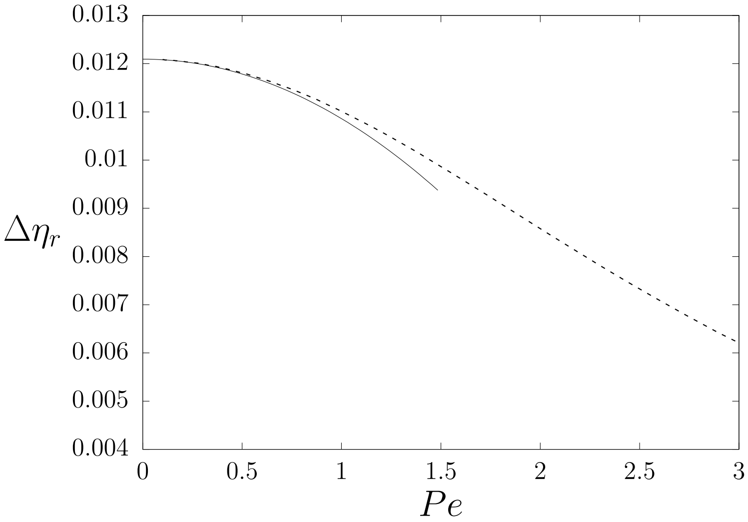

Figure 5.3 – Relative viscosity in the asymptotic limit of the low Peclet number. - - - Numerical results, —— Asymptotic solution (5.7). $\alpha_o = 1$, $\lambda = 1$, $\overline{\phi}_h = \overline{\phi}_m = 0.05$, $K_c = 0$.

In a similar manner, an asymptotic solution for large Péclet numbers was obtained. In the limit of $Pe^{-1} = 0$, the solution for the system (5.1) is

$$\begin{cases} H_{er}(r) = 0 \ , \\ H_{ez}(r) = 0 \ , \\ G = 32(1 + 2.5\overline{\phi}_h) \ , \\ \dot{\gamma}(r) = 2r \ . \end{cases} \tag{5.10}$$

Assuming that $H_{er} \sim Pe^{-1}$, we may propose a rescaling: $H_{er} = \tilde{H}_{er} Pe^{-1}$. Rewriting the system 5.1, results that:

$$\begin{cases} Gr - 16(1 + 2.5\phi_h)\dot{\gamma} - Pe^{-2} 8\phi_h \alpha_o^2 \dfrac{\chi_e}{\chi_i} \tilde{H}_{er}(1 + \chi_e H_{ez}) = 0 \ , \\ \dot{\gamma} H_{ez} - Pe^{-2}\left[2(1+\chi_e)\tilde{H}_{er} + \dfrac{\alpha_o^2}{3}\dfrac{\chi_e}{\chi_i}\tilde{H}_{er} H_{ez}(1 + \chi_e H_{ez})\right] = 0 \ , \\ \dot{\gamma}\tilde{H}_{er} - 2(1 - H_{ez}) - Pe^{-2}\dfrac{\alpha_o^2}{3}\dfrac{\chi_e}{\chi_i}\tilde{H}_{er}^2(1 + \chi_e H_{ez}) = 0 \ , \\ \dfrac{du}{dr} = -8\dot{\gamma} \ . \end{cases} \tag{5.11}$$

Notice the presence of the non-dimensional parameter $\epsilon = Pe^{-2}$. Again, if $\epsilon \ll 1$, a polynomial expansion in the form (5.4) can be applied. The effective susceptibility can be approximated as $\chi_e = \chi_i$, since its correction does not contribute to the systems of order ϵ^0 and ϵ^1. These systems are solved in combination with the boundary conditions

5.5, providing the following solutions:

$$\begin{cases} H_{er}(r) = \dfrac{1}{r} Pe^{-1} + \mathcal{O}(Pe^{-3}) \ , \\ H_{ez}(r) = \dfrac{1+\chi_i}{r^2} Pe^{-2} + \mathcal{O}(Pe^{-4}) \ , \\ G = 32(1+2.5\overline{\phi}_h) + 64\overline{\phi}_h \alpha_o^2 Pe^{-2} + \mathcal{O}(Pe^{-4}) \ , \\ \dot{\gamma}(r) = 2r + \dfrac{\overline{\phi}_h \alpha_o^2}{1+2.5\overline{\phi}_h} \left(4r - \dfrac{1}{2r}\right) Pe^{-2} + \mathcal{O}(Pe^{-4}) \ . \end{cases} \tag{5.12}$$

The relative viscosity in the limit of high Pe is:

$$\eta_r = \eta_\phi + 2\overline{\phi}_h \alpha_o^2 Pe^{-2} + \mathcal{O}(Pe^{-4}) \ . \tag{5.13}$$

Figure 5.4 presents a comparison between the numerical and analytical solutions in the region of high Péclet number. There is an agreement up to 5 % for values higher than $Pe = 5$.

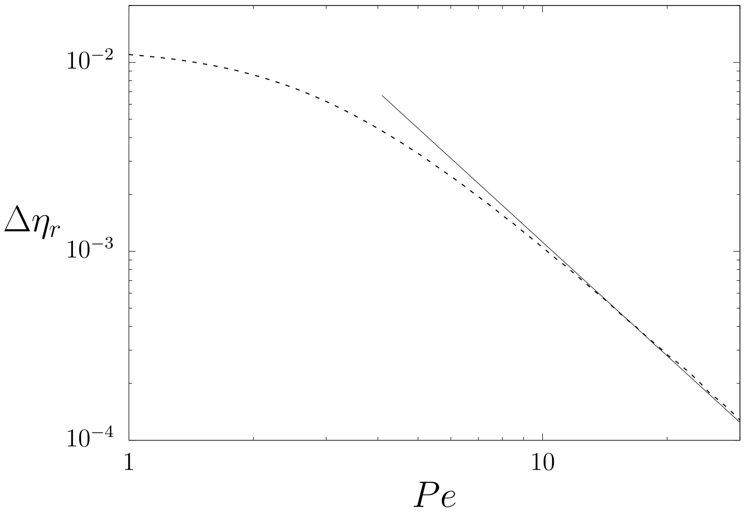

Figure 5.4 – Relative viscosity in the asymptotic limit of the high Peclet number.- - - Numerical results, —— Asymptotic solution (5.13). $\alpha_o = 1$, $\lambda = 1$, $\overline{\phi}_h = \overline{\phi}_m = 0.05$, $K_c = 0$.

The previous asymptotic solutions can also be rewritten for the wall viscosity η_w. In this case, it is more convenient to express these solutions as a function of the wall Péclet number, Pe_w, instead of the global value. Using the definition (3.46) and working the expressions (5.6) and (5.12) results that the solution in the limit of $Pe_w \ll 1$ is:

$$\eta_w = \eta_\phi + \eta_s - Pe_w^2 \frac{3C_m}{2} + \mathcal{O}(Pe_w^4) \ , \tag{5.14}$$

and the solution in the limit of $Pe_w \gg 1$ is:

$$\eta_w = \eta_\phi + \overline{\phi}_h \alpha_o^2 Pe_w^{-2} + \mathcal{O}(Pe_w^{-4}) \ . \tag{5.15}$$

5.1.2 Magnetization profiles

From the asymptotic solutions for the effective field, the non-dimensional magnetization components are calculated as

$$\begin{cases} M_r(r) = \dfrac{\alpha_o \chi_e(r)}{24\overline{\phi}_m \lambda} H_{er}(r) \ , \\ M_z(r) = \dfrac{\alpha_o \chi_e(r)}{24\overline{\phi}_m \lambda} H_{ez}(r) \ . \end{cases} \tag{5.16}$$

Figure 5.5 presents a comparison between the numerical results and the asymptotic solutions. Although the global Péclet number is fairly high, both low and high asymptotic solutions have good agreements with the numerical results in certain regions. Since the shear rate $\dot{\gamma}$ scales with r, the local Péclet number, $Pe_l = Pe\dot{\gamma}$, varies from 0 at the tube

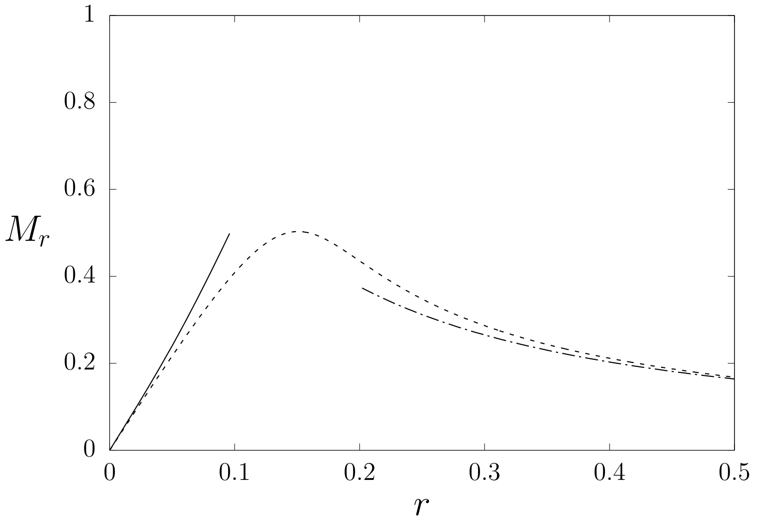

(a)

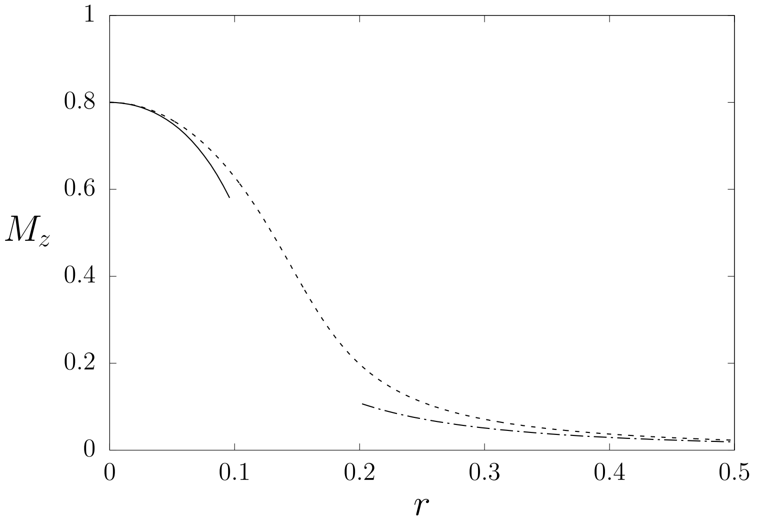

(b)

Figure 5.5 – (a) Radial and (b) axial magnetization profiles. - - - Numerical results, —— Low Péclet and $- \cdot - \cdot -$ High Péclet asymptotic solutions. $\alpha_o = 5$, $Pe = 20$, $\lambda = 1$, $\overline{\phi}_h = \overline{\phi}_m = 0.05$, $K_c = 0$.

center to Pe_w at the wall. Close to the center, the hydrodynamic torque is small compared to the magnetic torque, therefore the low Pe asymptotic solution agrees with the numerical profile. On the other hand, the vorticity effects prevails near the wall and the high Pe asymptotic solution has a better agreement in this region.

5.2 Model for spherical particles with hydrodynamic dispersion effects

In this section, the effects of the shear-induced dispersion in a suspension of magnetic spheres is investigated, as given by the system (3.42). The change in the volume fraction profile, the magnetization profiles, and the viscosity increase are analyzed as a function of the non-dimensional parameters. We consider the down-gradient diffusivity K_c as an independent parameter, whose origin is in the particles rugosity. For the ratio between the diffusivity coefficients, the experimental prediction by Phillips et al. (1992) gives $K_c/K_\eta = 0.66$.

5.2.1 Comparison between diffusive terms

$$\boldsymbol{N}^* = \underbrace{-\frac{2}{3Pe}\nabla\phi_h}_{\mathrm{I}} \underbrace{-\phi_h^2 K_c \nabla\dot{\gamma}}_{\mathrm{II}} \underbrace{-\phi_h\dot{\gamma}K_c\nabla\phi_h}_{\mathrm{III}} \underbrace{-\phi_h^2\dot{\gamma}K_\eta\frac{1}{\eta_\phi}\frac{d\eta_\phi}{d\phi_h}\nabla\phi_h}_{\mathrm{IV}} \ . \tag{5.17}$$

The volume fraction profile is influenced by four non-dimensional flux terms, as shown in equation (5.17): the Brownian diffusive flux (I), the hydrodynamic migration by gradient of shear rate(II), the hydrodynamic dispersion by gradient of volume fraction(III) and hydrodynamic dispersion by gradient of viscosity(IV). Only the gradient of shear rate migration term produces a segregation in the volume fraction profile, while the other three terms homogenize the suspension. Therefore, at a developed profile, the term II should be balanced by the terms I, III and IV. Figure 5.6 presents the magnitude of the flux evaluated at the wall as a function of the mean magnetic volume fraction. Applying a scaling in the diffusive terms, we notice that the Brownian flux (I) scales with $\overline{\phi}_h$, the gradient of shear rate migration (II) and the gradient of concentration dispersion (III) scale with $\overline{\phi}_h^2$ and the gradient of viscosity dispersion (IV) scales with $\overline{\phi}_h^3$. Therefore, at low concentrations, the Brownian flux dominates, as can be seen in Figure 5.6. At moderate concentrations, the shear rate gradient migration and concentration gradient dispersion prevail in the flux balance. The viscosity gradient dispersion has almost no influence for low concentration and only a small influence for moderate values. On the other hand, this term is very relevant at highly concentrated suspensions, which are out of the scope of this work (see Phillips et al. (1992)).

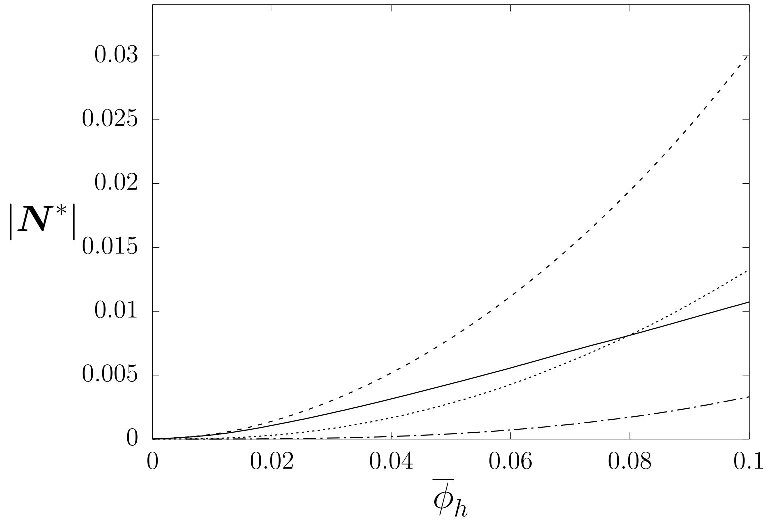

Figure 5.6 – Non-dimensional flux terms at the wall as a function of the mean hydrodynamic volume fraction. —- Brownian diffusion (I), − − − Shear gradient migration (II) ; · · · Concentration gradient dispersion (III); · − · Viscosity gradient dispersion (IV). $\alpha_o = 5$, $Pe = 5$, $\lambda = 1$, $\overline{\phi}_h/\overline{\phi}_m = 1$, $K_c = 2$, $K_c/K_\eta = 0.66$.

5.2.2 Volume fraction profiles

The main effect of the hydrodynamic dispersion is the segregation in the volume fraction profile, as can be seen on Figure 5.7. At null K_c, the profile is uniform. With increasing values of K_c, the suspension becomes more concentrated at the center of the tube, and more diluted at the wall. This result is expected since the particles will migrate away from the high shear region at the wall.

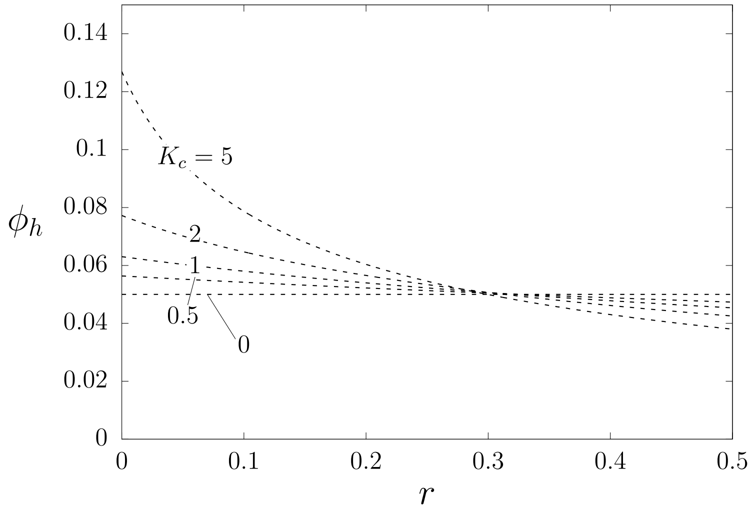

Figure 5.7 – Hydrodynamic volume fraction profile for various values of K_c. $Pe = 5$, $\alpha_o = 5$,$\lambda = 1$, $\overline{\phi}_m = \overline{\phi}_h = 0.05$, $K_c/K_\eta = 0.66$.

The importance of each diffusive flux term can also be seen in the volume fraction profile. Figure 5.8 presents the volume fraction profile if only some of the flux terms were considered in the model. If only the Brownian diffusion is present, the profile is uniform, as expected. Including the shear rate gradient migration term, a large particle segregation is observed. The addition of the concentration gradient dispersion term diminishes the migration effect. The viscosity gradient term has almost no influence in the profile, since it is significant only at very high concentration.

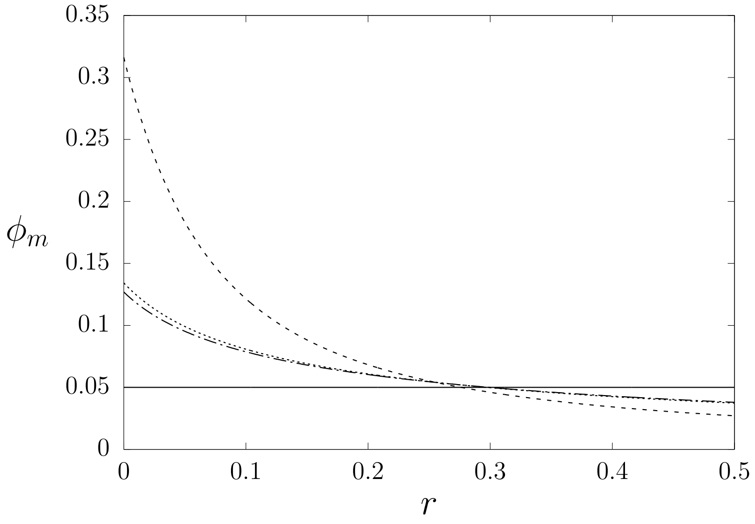

Figure 5.8 – Magnetic volume fraction profile for various conditions of diffusive terms: —- only term I, − − − only terms I and II; · · · only terms I,II and III; · − · all diffusive terms. $Pe = 5$, $\alpha_o = 5$,$\lambda = 1$, $\overline{\phi}_m = \overline{\phi}_h = 0.05$, $K_c = 2$, $K_c/K_\eta = 0.66$.

5.2.3 Magnetization profiles

The magnetization profiles are implicitly dependent on the volume fraction profiles, since the magnetic susceptibility is proportional to ϕ_m. For non-null values of K_c, the magnetization increases at the center and decreases at the wall with respect to the $K_c = 0$ case. Figure 5.9 presents the magnetization components profiles for various values of K_c.

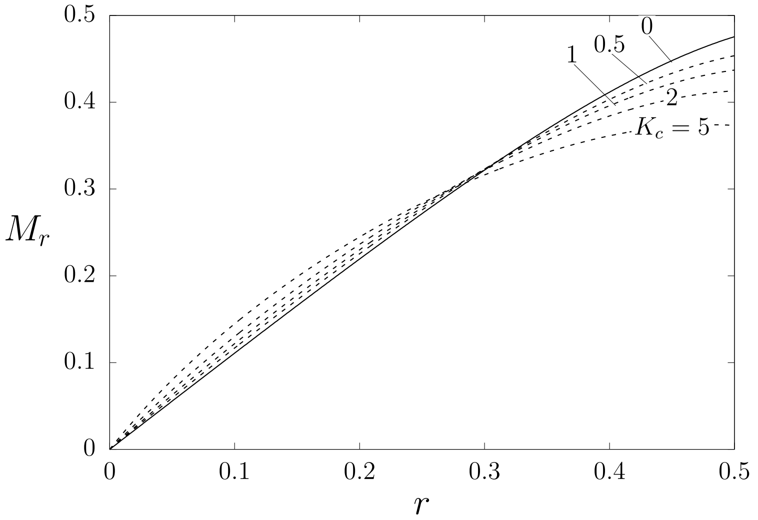

(a)

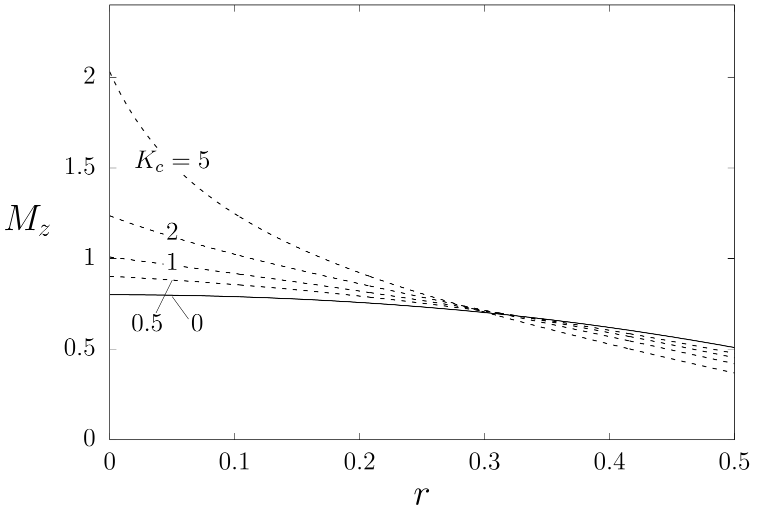

(b)

Figure 5.9 – (a) Radial and (b) axial magnetization components profiles for various values of K_c. $Pe = 5$, $\alpha_o = 5$,$\lambda = 1$, $\overline{\phi}_m = \overline{\phi}_h = 0.05$, $K_c/K_\eta = 0.66$.

5.2.4 Velocity profile

The reference velocity profile for a Newtonian fluid in capillary flow is a parabolic, or quadratic, curve. In the case a ferrofluid with a non-uniform concentration, the suspension viscosity will vary throughout the tube. Thus, the velocity profile will no longer be parabolic. Figure 5.10 presents the velocity profile for moderate values of the non-dimensional parameters and the diffusivity coefficient. A small deviation from the parabolic profile is observed, with the maximum difference being at the center (maximum velocity). At this position, the particle concentration and and the magnetoviscous effect are higher, thus generating a more viscous suspension compared to the wall. As a consequence, the shape of the profile is flattened at the center.

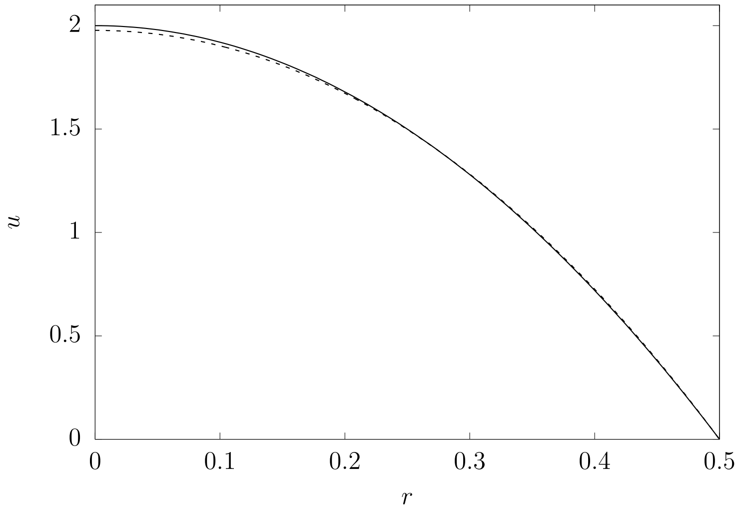

Figure 5.10 – Velocity profile. - - - Numerical results, —— Parabolic profile. $\alpha_o = 5$, $Pe = 5$, $\lambda = 1$, $\overline{\phi}_h = \overline{\phi}_m = 0.05$, $K_c = 2$.

Although the velocity profile for a ferrofluid in capillary flow is not strictly parabolic, we still use the term *quadratic* to describe this flow since it is the reference condition and the deviations are small.

5.2.5 Magnetoviscous effect

In the absence of hydrodynamic dispersion, the volume fraction is uniform throughout the tube and the minimum value of viscosity is the ordinary suspension's viscosity for the mean volume fraction. If the shear induced dispersion is present, the particles will migrate away from the wall, and the viscosity may reach values bellow $\eta_\phi(\overline{\phi}_h)$. This occurs because the suspension becomes very dilute at the wall.

The hydrodynamic dispersion produces a nearly uniform reduction in the viscosity for the whole range of α_o, as can be seen in Figure 5.11. The increase in K_c reduces the relative viscosity, since the suspension becomes more dilute at the wall. The Figure 5.11 suggests that the diffusivity coefficient K_c and the global Langevin parameter α_o have independent effects on the viscosity, neither increasing or attenuating each other. This occurs because the applied field does not affect the concentration distribution and the diffusivity coefficient (or implicitly the rugosity) does not inflict in the torque balance of the particles. The effect of the diffusivity coefficient can be seen on the inset of Figure 5.11, which displays the saturation limit ($\alpha_o \to \infty$) of the relative viscosity increase with respect to K_c.

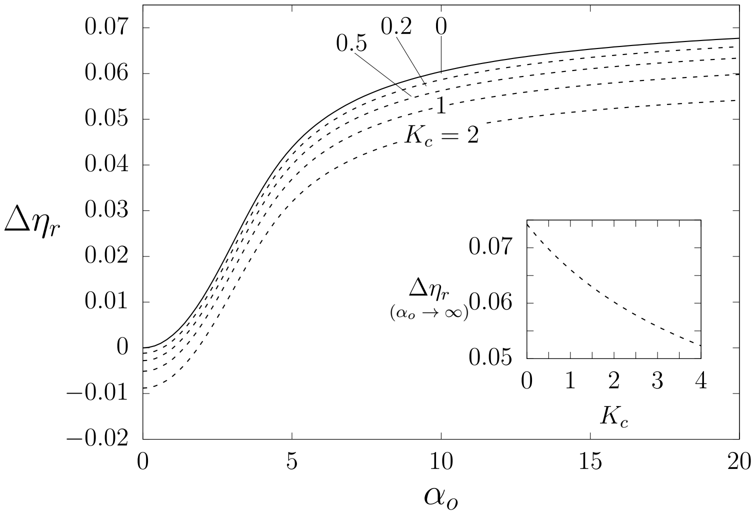

Figure 5.11 – Relative viscosity increase as a function of the effective field parameter for various values of K_c. *Inset:* Saturation limit of the relative viscosity increase with respect to the diffusivity coefficient. $Pe = 5$,$\lambda = 1$, $\overline{\phi}_m = \overline{\phi}_h = 0.05$, $K_c/K_\eta = 0.66$.

5.2.6 Shear-thinning effect

Figure 5.12 presents the relative viscosity increase with respect to the Péclet number for various values of K_c. As the K_c increases, the shear-thinning effect becomes stronger due to the reduction of volume fraction near the wall. At $Pe = 0$, the volume fraction is homogeneous for any value of K_c and the viscosity is dependent only on the applied field. The Figure 5.12 shows that the Péclet number simultaneously affects the hydrodynamic dispersion and the magnetoviscous effect. For constant values of α_o and K_c, a high value of Pe implies that the vorticity effects are much stronger than the Brownian motion. Therefore, the Brownian motion can not compensate the particle segregation imposed by the shear-induced dispersion. Also, a large Péclet number implies that the hydrodynamic torque overcomes the magnetic torque on the particles, thus intensifying the shear-thinning effect.

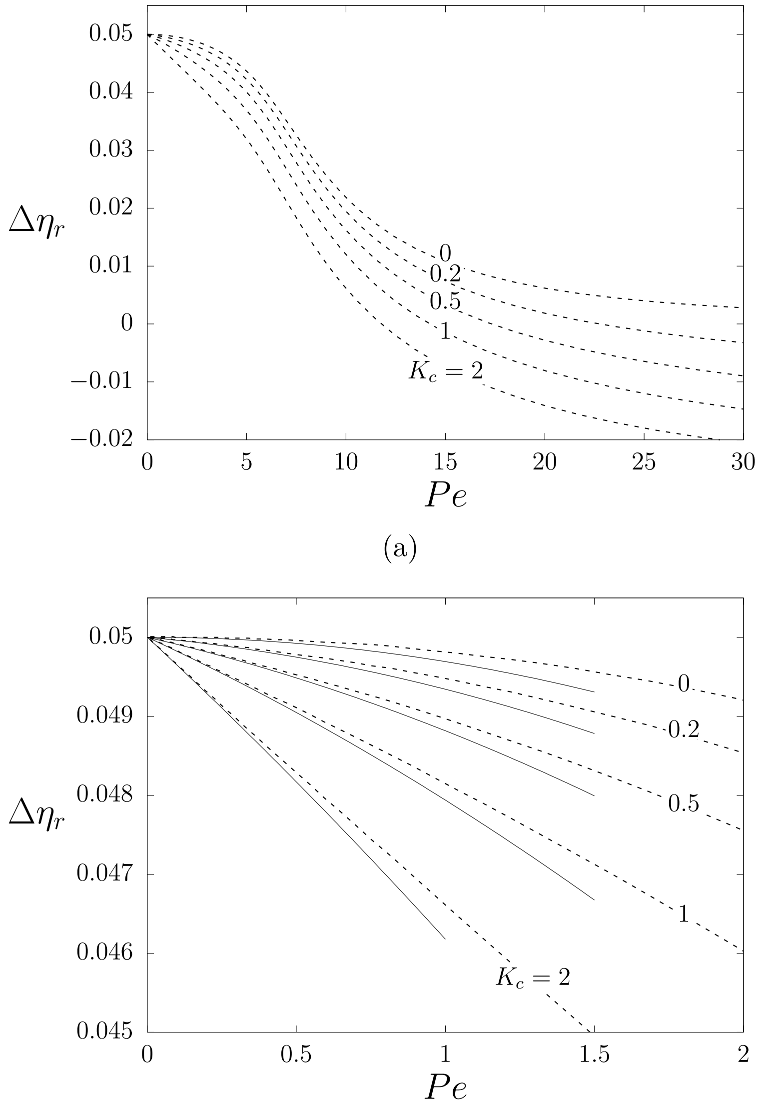

(a)

(b)

Figure 5.12 – (a) Relative viscosity increase as a function of the Peclet number for various values of K_c. (b) Asymptotic solution (continuous line) for low Péclet number, equation (5.19). $\alpha_o = 5$,$\lambda = 1$, $\overline{\phi}_m = \overline{\phi}_h = 0.05$, $K_c/K_\eta = 0.66$.

5.2.7 Low Péclet number asymptotic solution

In similar manner to the case without hydrodynamic dispersion, a new asymptotic solution in limit of low Péclet number was obtained, now considering the presence of hydrodynamic dispersion. A few simplifications are considered in order to obtain a more concise solution:

- The viscosity gradient diffusion is neglected, since this mechanism has little influence for dilute suspensions;
- In the diffusion equation, the shear rate profile is set to $\dot{\gamma} = 2r$ (Newtonian fluid profile). This simplification allows to decouple the diffusion equation from the rest

of the system. The error associated is small, since the numerical simulations show a maximum deviation of 2% from the Newtonian profile;

- The magnetic susceptibility is assumed as the value for the global Langevin parameter and the mean volume fraction, $\chi_e = \chi_o \equiv \chi_e(\alpha_o, \overline{\phi}_m)$. Again, the error associated is less than 2% in the low Péclet number region.

The simplified governing system is

$$\begin{cases} Gr - 16(1+2.5\phi_h)\dot{\gamma} - 8\dfrac{\phi_h\alpha_o^2}{Pe}\dfrac{\chi_o}{\chi_i}H_{er}(1+\chi_e H_{ez}) = 0 \ , \\ \dot{\gamma}H_{ez} - \dfrac{2}{Pe}(1+\chi_o)H_{er} - \dfrac{\alpha_o^2}{3Pe}\dfrac{\chi_o}{\chi_i}H_{er}H_{ez}(1+\chi_o H_{ez}) = 0 \ , \\ \dot{\gamma}H_{er} - \dfrac{2}{Pe}(1-H_{ez}) - \dfrac{\alpha_o^2}{3Pe}\dfrac{\chi_o}{\chi_i}H_{er}^2(1+\chi_o H_{ez}) = 0 \ , \\ \left(\dfrac{2}{3Pe} + K_c\phi_h 2r\right)\dfrac{d\phi_h}{dr} + 2\phi_h^2 K_c = 0 \ , \\ \dfrac{du}{dr} = -8\dot{\gamma} \ . \end{cases} \tag{5.18}$$

Consider an polynomial expansion of the system variables in $\epsilon = Pe$, with $Pe \ll 1$. Asymptotic solutions up to order Pe^2 are obtained using a regular pertubation method. The details of the solution are presented in the Appendix A. The asymptotic solution for the relative viscosity is

$$\eta_r = \eta_\phi + \eta_s - PeC_h - Pe^2\left(\frac{3}{2}\frac{C_h^2}{\eta_\phi + \eta_s} + C_m\right) + \mathcal{O}(Pe^3) \ , \tag{5.19}$$

where

$$C_h = \frac{K_c\overline{\phi}_h(\eta_\phi + \eta_s - 1)}{5} \ . \tag{5.20}$$

Here, $\eta_\phi = 1 + 2.5\overline{\phi}_h$ and η_s is given by (5.8). The asymptotic solution for the wall viscosity as a function of the wall Péclet number is

$$\eta_w = \eta_\phi + \eta_s - \frac{5}{2}Pe_w C_h - Pe_w^2\left(\frac{21}{8}\frac{C_h^2}{\eta_\phi + \eta_s} + \frac{3C_m}{2}\right) + \mathcal{O}(Pe_w^3) \ . \tag{5.21}$$

The numeric and asymptotic solutions are compared in the inset of Figure 5.12. A very good agreement is observed up to $Pe = 1$. As can be seen in the expression (5.19), the correction order Pe is proportional to K_c. If $K_c = 0$, the first non-null correction is of order Pe^2 and depends on the magnetic parameters. Therefore, at low Péclet numbers, the particle segregation is the main mechanism of viscosity reduction.

5.2.8 Influence of the mean volume fraction

The ordinary suspension's viscosity is given by Einstein's viscosity in the low volume fraction regime, and is linear with $\overline{\phi_h}$. The magnetoviscous effect in is also nearly linear with $\overline{\phi_h}$, as can be seen in the asymptotic solutions (5.7) and (5.13). Therefore, in the absence of hydrodynamic dispersion, the relative viscosity increase is approximately proportional to the mean volume fraction. If the hydrodynamic dispersion is introduced, the relative viscosity will decrease with increasing K_c, as can be seen in Figure 5.13. This reduction is more significant at moderate volume fractions, and very small at low volume fraction. Therefore, a slightly negative concavity is observed in the relative viscosity curve. This result is expected since the hydrodynamic migration term scales with $\overline{\phi}_h^2$.

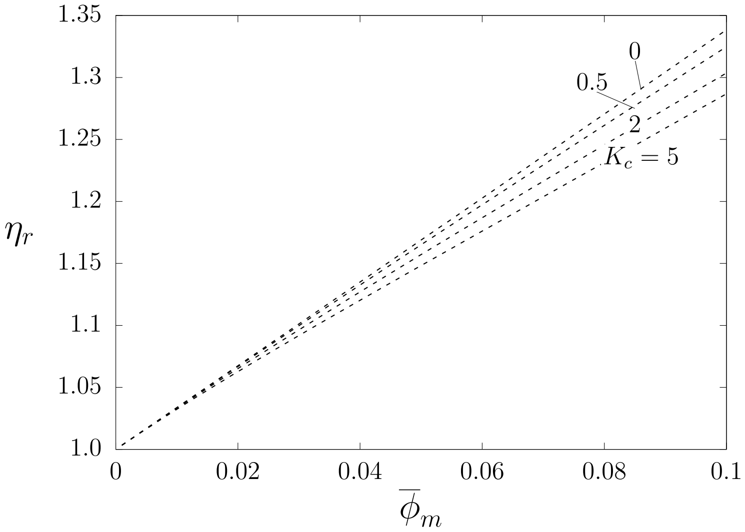

Figure 5.13 – Relative viscosity as a function of the mean magnetic volume fraction for various values of K_c. $\alpha_o = 5$, $Pe = 5$, $\lambda = 1$, $\overline{\phi}_h/\overline{\phi}_m = 1$, $K_c/K_\eta = 0.66$.

5.3 Model for smooth spheroidal particles

In this section we consider a model for a ferrofluid composed of smooth spheroidal particles with hydrodynamic dispersion, as given by the system (3.55) The down-gradient diffusivity K_c is estimated by the correlations (2.97) and (2.98) of Cunha and Hinch (1996), extended to non-spherical particles. The governing system of equations was solved numerically and the relative viscosity increase was computed for various conditions of the non-dimensional parameters.

5.3.1 Shear-thinning effect

Firstly, consider the effect of the non-sphericity in the stress tensor alone, without the presence of the hydrodynamic dispersion. Figure 5.14a compares the relative viscosity increase as a function of Péclet for a model of spherical particles and a model of spheroids, both with the down-gradient diffusivity coefficient set to $K_c = 0$. The viscosity increase for spheroids is much larger since this shape produces greater resistance to shear in comparison to spheres. The difference is much larger for small Péclet numbers.

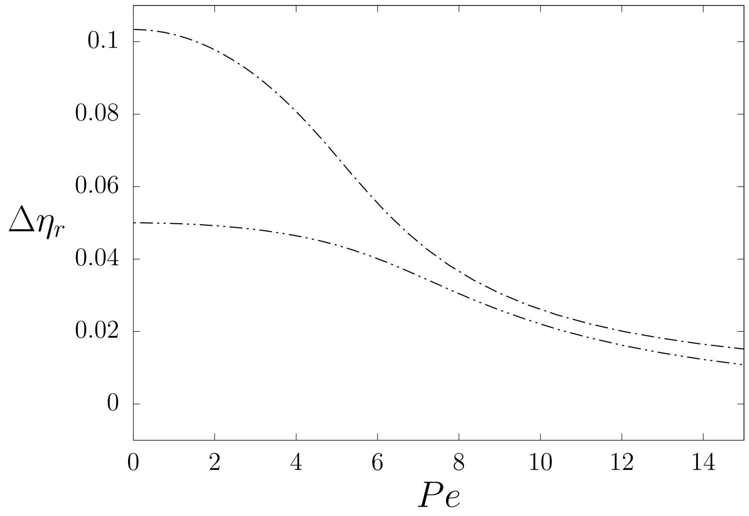

(a) $- \cdot \cdot -$ Spherical and $- \cdot -$ spheroidal particles ($\beta = 1.5$) without hydrodynamic dispersion.

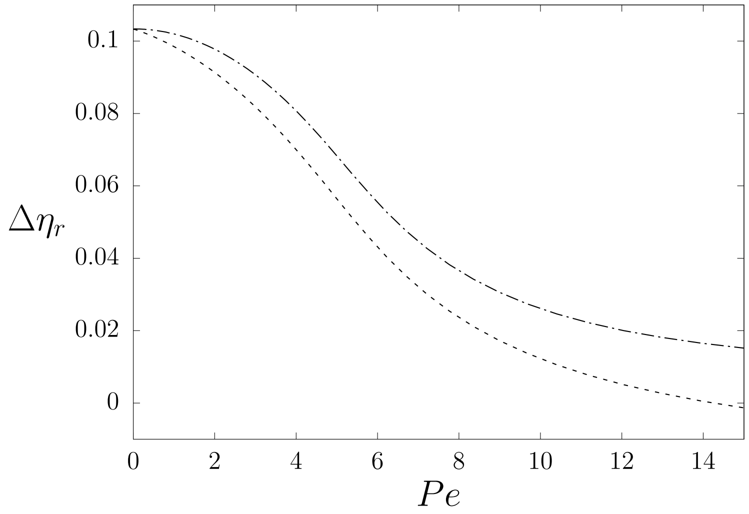

(b) Ellipsoidal particles - - - with and $- \cdot -$ without hydrodynamic dispersion.

Figure 5.14 – Relative viscosity increase as a function of the global Péclet number. $\alpha_o = 5$, $\lambda = 1$, $\overline{\phi}_h = \overline{\phi}_m = 0.05$.

Now, we observe only the effect the hydrodynamic dispersion for the model of spheroidal particles. Figure 5.14b presents the relative viscosity increase as function of Péclet for a model of spheroidal particles with the down-gradient diffusivity K_c set to 0 and with K_c given by the correlations of Cunha and Hinch (1996). The results show that the hydrodynamic dispersion intensifies the shear-thinning behavior of the suspension. The influence of the hydrodynamic dispersion is more significant at large Péclet numbers.

For the following results, the full model is considered, in which the non-spherical shape influences both the stress tensor and the hydrodynamic dispersion. Figure 5.15 presents the shear-thinning effect for various values of the aspect ratio β. For weak flows (low Pe), the viscous dissipation increases with β. In this regime, the concentration profile is nearly uniform and the spheroidal shape produces a higher viscous dissipation. On the other hand, for strong flows (high Pe) the behavior is inverted, and the viscous dissipation decreases with β. In this condition, the shear-induced dispersion created by the non-spherical particles reduces the wall concentration. The concentration reduction is sufficient to overcome the resistance associate with the particle's shape, and the net result is a viscosity reduction.

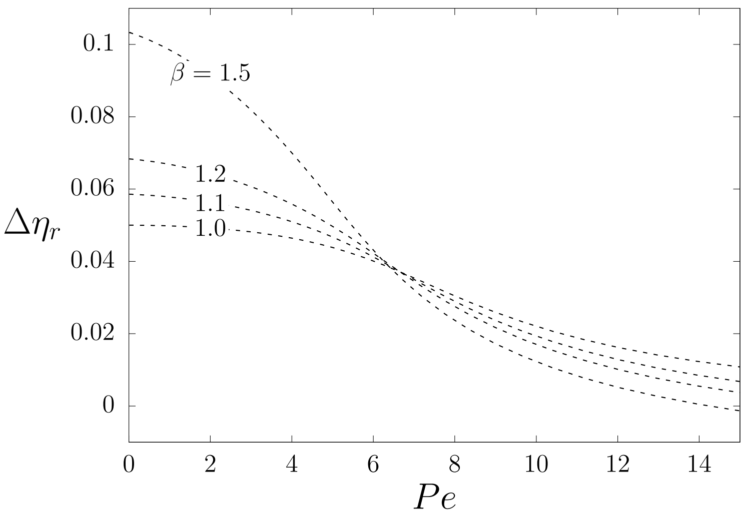

Figure 5.15 – Relative viscosity increase as a function of the global Péclet number for various values of β. $\alpha_o = 5$, $\lambda = 1$, $\overline{\phi}_h = \overline{\phi}_m = 0.05$, K_c given by equation (2.98), $K_c/K_\eta = 0.66$.

The change of regime accordingly to the Peclet number can also be seen in Figure 5.16, which presents the relative viscosity increase as a function of the aspect ratio. At high Pe, the slope of the curve becomes negative, indicating that the hydrodynamic dispersion is the dominant mechanism.

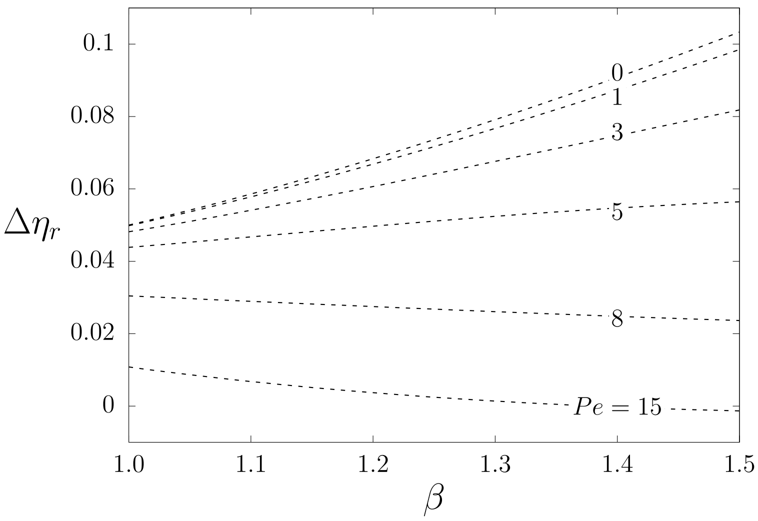

Figure 5.16 – Relative viscosity increase as a function of the aspect ratio β for various values of Pe. $\alpha_o = 5$, $\lambda = 1$, $\overline{\phi}_h = \overline{\phi}_m = 0.05$, K_c given by equation (2.98), $K_c/K_\eta = 0.66$.

The wall viscosity presents a behavior similar to the relative viscosity, with only quantitative differences, as can be seen in Figure 5.17.

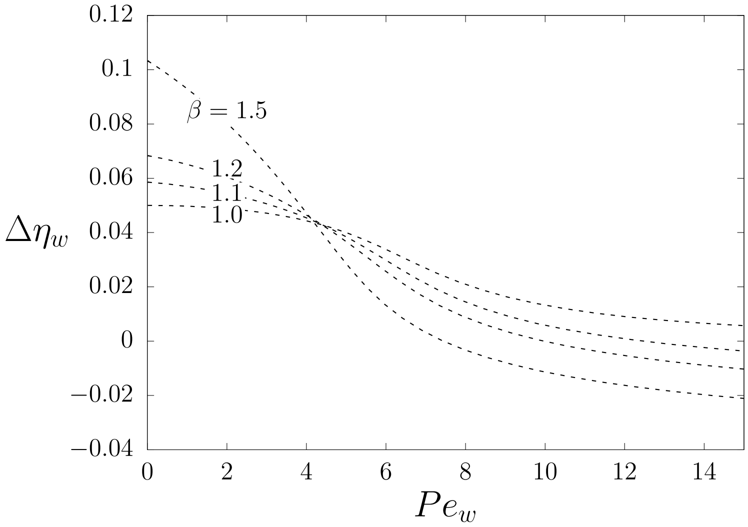

Figure 5.17 – Wall viscosity increase as a function of the wall Péclet number for various values of β. $\alpha_o = 5$, $\lambda = 1$, $\overline{\phi}_h = \overline{\phi}_m = 0.05$, K_c given by equation (2.98), $K_c/K_\eta = 0.66$.

The volume fraction and magnetization profiles for spheroidal particles are very similar to the results for spheres. Therefore, the plots for these quantities are not presented.

5.3.2 Critical Péclet number

Figures 5.15 and 5.16 have two clear regions: a low Péclet region, where the viscosity increases with β, and a high Péclet region, where the viscosity decreases with β. In the low Péclet regime the magnetoviscous effect dominates while the hydrodynamic dispersion dominates in the high Pećlet regime. The transition does not occur at a single Péclet value, but rather at a small interval. Nevertheless, we may define a critical Péclet number Pe_c for which the derivate of η_r with respect to β at $\beta = 1$ is null, *i.e.*

$$\left.\frac{\partial \eta_r}{\partial \beta}\right|_{\beta=1, Pe_c} = 0 \ . \tag{5.22}$$

Since there is no analytical expression for this derivative, it was numerically computed using a small step in β. The dependence of Pe_c with the global Langevin parameter and the mean volume fraction was investigated, as seen in Figure 5.18. A lower critical Peclet number indicates that the hydrodynamic dispersion effect is stronger compared to the magnetoviscous effect.

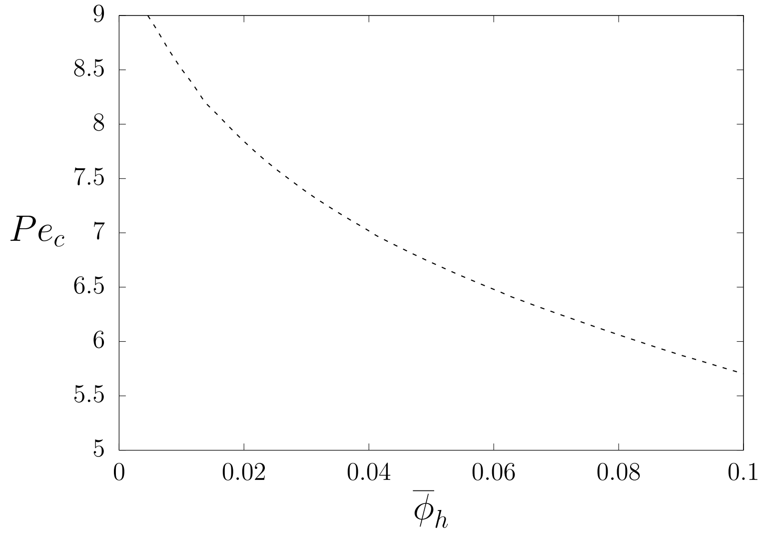

(a) $\alpha_o = 5$

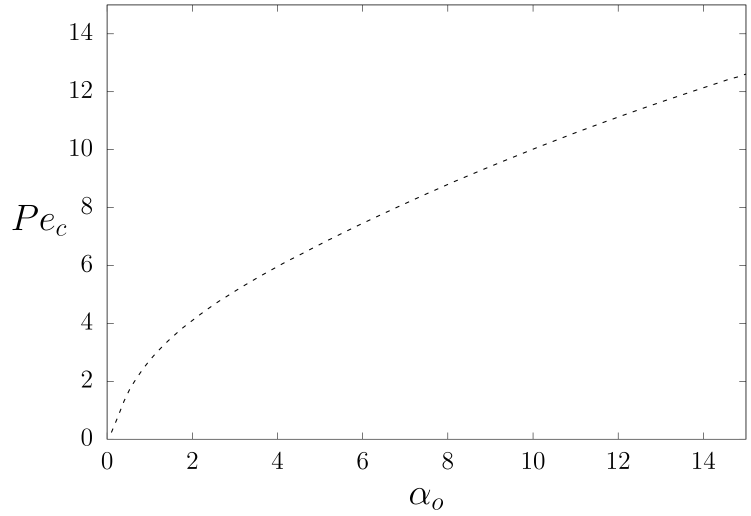

(b) $\overline{\phi}_h = 0.05$

Figure 5.18 – Critical Péclet number as a function of the (a) mean hydrodynamic volume fraction and of the (b) global Langevin parameter. $\lambda = 1$, $\overline{\phi}_h = \overline{\phi}_m$, K_c given by equation (2.98), $K_c/K_\eta = 0.66$.

The critical Péclet number has a monotonically increasing behavior with α_o, as is presented in Figure 5.18b. Since the magnetoviscous effect increases with the applied field, a stronger flow will be needed to produce a sufficiently intense particle migration.

Since the hydrodynamic dispersion is an effect order $\overline{\phi}_h^2$, while the magnetoviscous effect is of order $\overline{\phi}_h$, the critical Péclet number decreases with the mean volume fraction. At the limit of $\overline{\phi}_h \to 0$, the critical Péclet number is expected to go asymptotically to infinite. However, the very low magnetoviscous response at this region makes the numerical calculations very time expensive.

5.3.3 Magnetoviscous effect

The balance between the resistance to shear and the particle's segregation is also dependent on the field intensity. At small Péclet numbers, the shear-induced dispersion is not relevant and the concentration profile is nearly homogeneous. In this condition, the magnetoviscous effect, as present in Figure 5.19a, increases with the global Langevin parameter α_o. For strong fields, the particles are nearly locked in the field orientation, and the viscous dissipation is greatly increased.

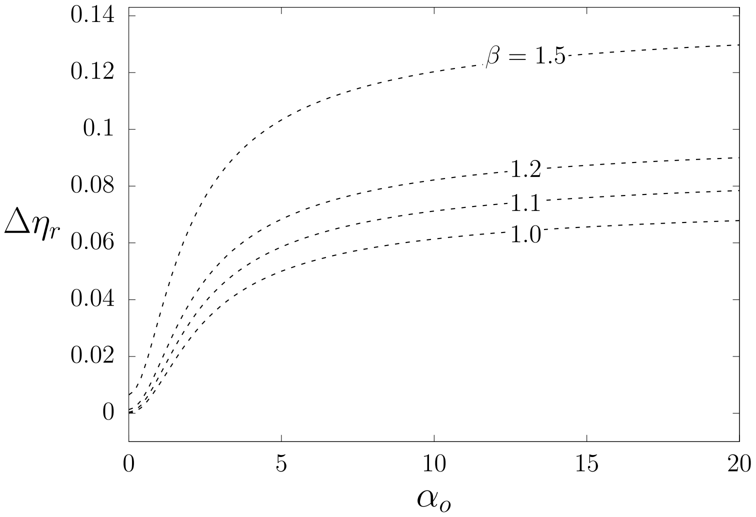

(a) $Pe = 0$

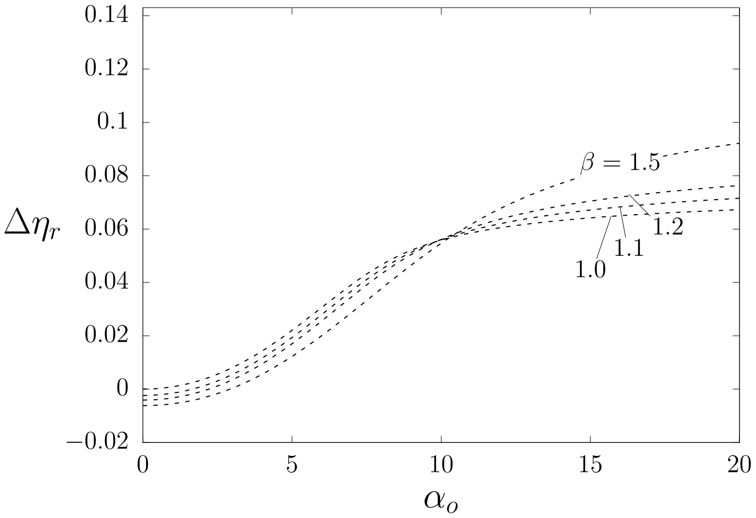

(b) $Pe = 10$

Figure 5.19 – Relative viscosity increase as a function of the global Langevin parameter for various values of ε. $\lambda = 1$, $\overline{\phi}_h = \overline{\phi}_m = 0.05$, K_c given by equation (2.98), $K_c/K_\eta = 0.66$.

For large Péclet numbers, a non-homogeneous concentration profile is produced. In the weak field regime, the segregation effect dominates and the viscosity decreases with β. However, for strong fields, the shape's resistance to shear overcomes the segregation and the net result is a viscosity increase with β.

5.3.4 Normal stress difference

The normal stress difference is a measure of the anisotropic and non-linear response of a suspension. The first normal stress difference was calculated at the capillary wall for various values of the non-dimensional parameters. The non-dimensional first normal stress difference is defined as $N_1 = (\sigma_{zz} - \sigma_{rr})/\eta_o\dot{\gamma}$. Using the stress tensor expression (2.78) and the expressions (B.3), the following expression for N_1 is obtained.

$$N_1 = 5\phi_h \left[\frac{2\psi_4 \mathcal{L}_2 H_{er} H_{ez}}{H_e^2} - \frac{\psi_3 \mathcal{L}_4 H_{er} H_{ez} (H_{ez}^2 - H_{er}^2)}{H_e^4} \right] . \tag{5.23}$$

For spheres ($\beta = 1$), the suspension is isotropic and the normal stress difference is null. As the particles become non-spherical, N_1 assumes a positive value. The dependence of N_1 with the global Langevin parameter is presented in Figure 5.20. At small applied fields, the particles are nearly randomly orientated and the normal stress difference is very small. N_1 presents a growth with α_o^2, as can be seen in the inset of Figure 5.20. Although analytical solutions for N_1 are not available, this dependence can be predicted with a scale analysis. From the asymptotic solutions (5.6) and (5.12) in the absence of hydrodynamic dispersion, it can be seen that the H_{er} and H_{ez} are approximately $\mathcal{O}(\alpha_o^0)$. The high-order Langevin functions $\mathcal{L}_2$ and $\mathcal{L}_4$. At small values of α_o, the asymptotic limits are $\mathcal{L}_2 \sim \alpha_o^2$ and $\mathcal{L}_4 \sim \alpha_o^4$. Therefore, the dependence of N_1 in the limit of low fields is dictated by $\mathcal{L}_2$, leading to a relation of $N_1 \sim \alpha_o^2$. For large values of α_o, the slope of the curve switches and the first normal stress difference decays to 0. This behavior at high fields occurs because the first normal stress difference is approximately proportional to H_{er}. As the fluid approaches saturation, the effective field fully aligns with the longitudinal direction and the radial component vanishes.

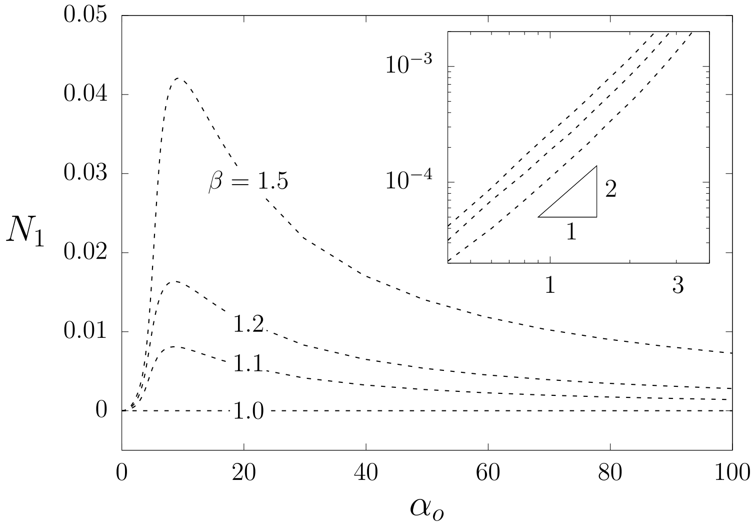

Figure 5.20 – First normal stress difference at the wall as a function of the global Langevin parameter for various values of β. *Inset:* Low global Langevin parameter region. $Pe = 5$, $\lambda = 1$, $\overline{\phi}_h = \overline{\phi}_m = 0.05$, K_c given by equation (2.98), $K_c/K_\eta = 0.66$.

Concerning the influence of the wall Péclet number (*i.e.* the flow intensity), the normal stress difference is small for very low or very high Pe_w, reaching a maximum at moderate flows (Fig. 5.21). The dependence of N_1 with the Péclet number is dictated by the effective field components H_{er} and H_{ez}. At small Péclet numbers, the asymptotic solutions (5.6) predict that $H_{ez} \sim 0$ and $H_{er} \sim Pe$, resulting in a dependence of the normal stress difference of $N_1 \sim Pe$. The numerical results agree with this relation, as can be seen in the inset of Figure 5.21. The increase in N_1 at the low Péclet region was experimentally observed in the works of Odenbach et al. (1999) and Pereira (2019).

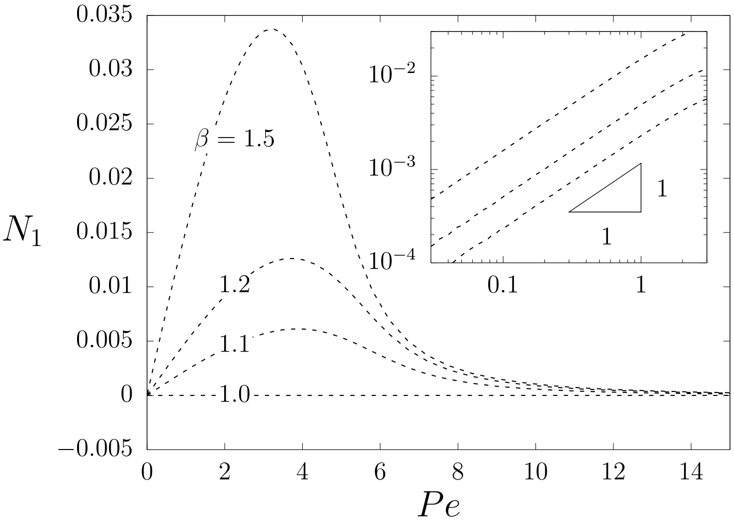

Figure 5.21 – First normal stress difference at the wall as a function of the wall Péclet number for various values of β. *Inset:* Low wall Péclet number region. $\alpha_o = 5$, $\lambda = 1$, $\overline{\phi}_h = \overline{\phi}_m = 0.05$, K_c given by equation (2.98), $K_c/K_\eta = 0.66$.

The results for the volume fraction profile and the magnetization profile for the smooth spheroids model are not presented since they are very similar to the results for spherical particles (Figures 5.7 and 5.9).

6 Experimental Methods

In this section, the experimental methods adopted are described. The experimental setup consists of a capillary viscometer equipped with a solenoid coil that provides a uniform magnetic field. The measured hydrodynamic quantities are the flow rate and the pressure drop, while the measured magnetic quantity is the electric current applied to the solenoid. From these parameters, the viscosity and the non-dimensional physical parameters are calculated. A parallel plate rheometer is also used for calibration and comparison with a simple shear flow.

6.1 Capillary Viscometer

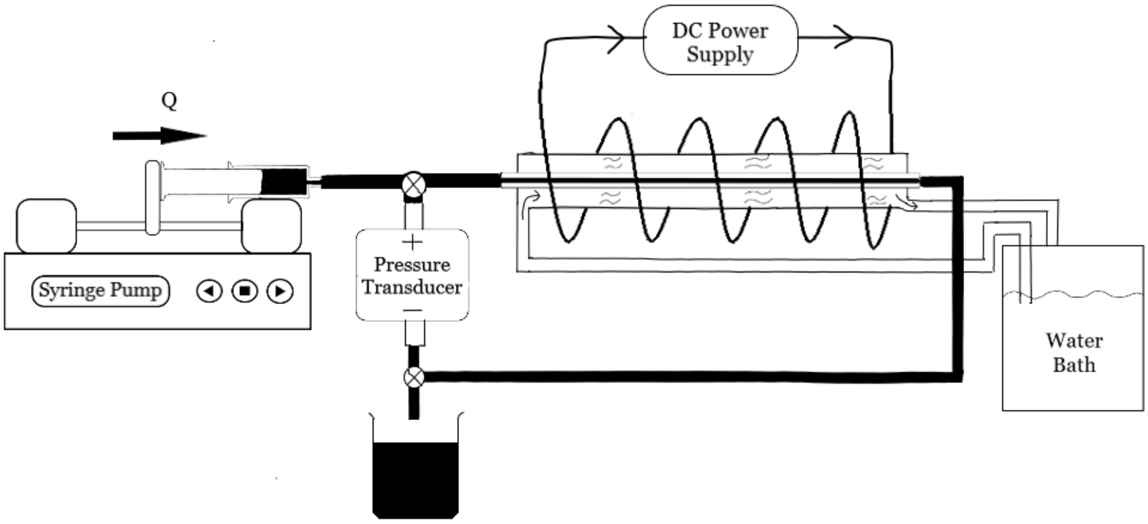

Figure 6.1 – Diagram of the capillary viscometer.

The capillary viscometer used to investigate the tube flow consists of capillary tubes, syringes, a syringe pump, a solenoidal coil, a power supply, a pressure transducer, a data acquisition system, and a thermal bath. The experimental setup is located at the Laboratory of Microhydrodynamics and Rheology - MicroReo/VORTEX, at the University of Brasília. The diagram in the Figure 6.1 illustrates the experimental setup. The syringe pump supplies the capillary tube with a constant flow rate of magnetic fluid. The pressure transducer measures the pressure difference between the inlet and the outlet of the tube.

The transducer's reading is sent to a data acquisition system, which collects and stores the data. The auxiliary tubes and connections are sufficiently large in order to not affect the pressure reading. A capillary tube is inserted in the gap of a solenoid coil, which provides a nearly uniform longitudinal magnetic field. Water is circulated around the tube to maintain the measurement temperature constant. This water is pumped and cooled with a thermal bath.

6.1.1 Capillary tubes

The capillary tubes are glass-made by the *Hildenberg* manufacturer. The tube length is L = 150 mm, the external diameter is 3 mm and the inner diameter is 1000 μm. The high aspect ratio ensures the unidirectional flow condition. The inner diameter accuracy is of ± 50 μm.

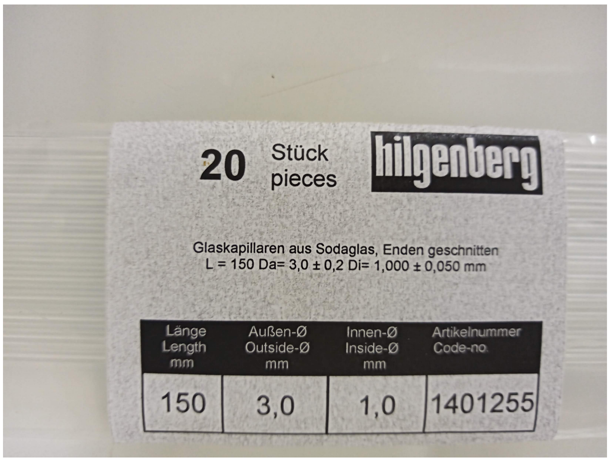

20 Stück pieces hilgenberg

Glaskapillaren aus Sodaglas, Enden geschnitten
L = 150 Da= 3,0 ± 0,2 Di= 1,000 ± 0,050 mm

Länge Length mm	Außen-Ø Outside-Ø mm	Innen-Ø Inside-Ø mm	Artikelnummer Code-no.
150	3,0	1,0	1401255

Figure 6.2 – Glass capillary tubes from *Hildenberg*.

6.1.2 Syringe pump

The flow rate is controlled by a syringe pump from *Cole & Parmer*, model KDS 101 (Fig. 6.3). The flow rate range depends on the syringe used. For a 5 ml syringe, the flow rate range is from 0.01 to $14,000 \mu l$/min. The flow rate accuracy is of ±1 % and the precision is of ±0,1 %.

6.1.3 Pressure transducer

The pressure difference between the tube's entrance and exit is measured by the variable reluctance pressure transducer DP-15 from *Valydine* (Fig. 6.4). It consists of a magnetically permeable diaphragm clamped between two stainless steel blocks. Each one has an inductance coil. When different pressures are applied to the diaphragm sides, it deflects. This deflection increases the inductance of one coil and decreases that of the

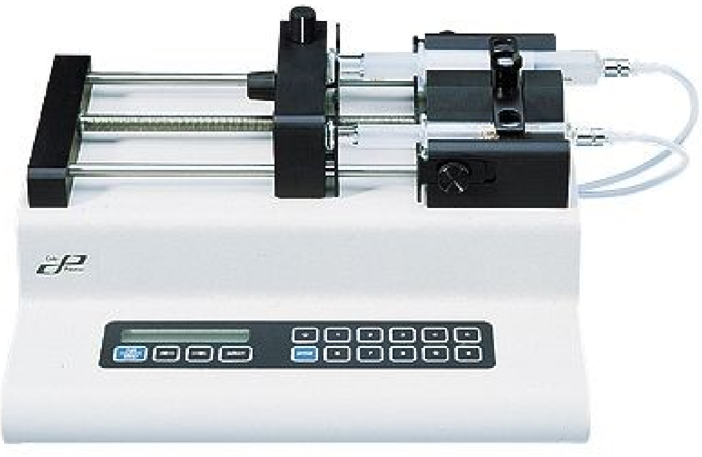

Figure 6.3 – Syringe pump from *Cole & Parmer*, model KDS 101.

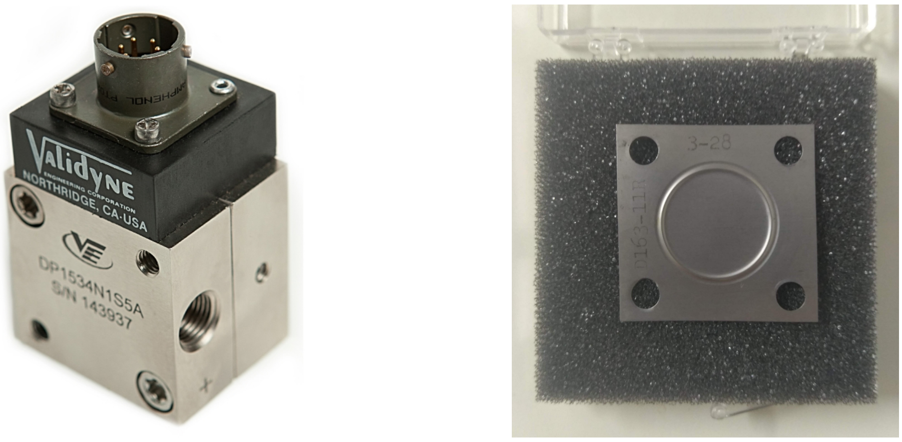

(a) Transducer body

(b) Pressure membrane

Figure 6.4 – Variable reluctance pressure transducer DP-15 from *Validyne*.

other. An AC bridge converts the inductance difference into an AC signal. Finally, the data acquisition system rectifies and amplifies the AC signal into a DC voltage proportional to the pressure difference. The pressure range is defined by the diaphragm used. In this work, the diaphragms number 26 and 42 were used, with a maximum pressure difference of 26 and 1040 mmHg respectively. The transducer accuracy is 0.25% of the full scale. The transducer's cavities were filled with glycerol to prevent the entrance of ferrofluid, which could affect the instruments reading.

6.1.4 Solenoid

The uniform longitudinal magnetic field in the tube was generated by two solenoid coils in series. Each solenoid is made of a thick coil from enameled cooper wire, with 2400 turns and 64 mm length, manufactured by *AZEHEB* (Fig.6.5). The DC current is supplied by the DC power supply MPC 3005 from *Milipa*. The axial magnetic field generated by

(b) Power supply

(a) Solenoid coil

Figure 6.5 – (a) Solenoid coil from enameled cooper wire and (b) DC power supply.

the solenoid coils is given by

$$H_o = f_e \frac{N_v I}{L} \, , \tag{6.1}$$

where N_v is the number of turns, I is the electric current, L is the length and f_e is an experimental correction factor. The maximum current that can be applied by the power supply is 1.20 A, with an accuracy of ±0.02 A. The correction factor f_e was calibrated with a curve of the measured magnetic field against the applied electric current. The axial magnetic field was measured with the Gaussmeter *F.W. Bell 5060*, which has an accuracy of 2 %. At high electric currents, the solenoid suffers an intense heating, therefore a fan is used for cooling.

6.1.5 Thermal bath

Since the fluid's viscosity is highly sensible to a temperature variation, the capillary tube was inserted in another larger silicon tube in which water is circulated. The water temperature and flux rate are controlled by the thermal bath ECO SILVER RE 415 from *LAUDA* manufacturer (Fig. 6.6). The water temperature was set to $T = 25,00 \pm 0,02^oC$.

6.2 Rotational Rheometer

The rotational rheometer Physica MCR 301 from *Anton Paar* (Fig. 6.7) was used to perform simple shear measurements on the magnetic fluids samples. It uses the parallel plate geometry flow, in which the fluid is placed between two parallel disks, one fixed and the other rotating at an angular velocity Ω. The rheometer measures the torque T required to shear the fluid. For a Newtonian fluid, the viscosity can be calculated using the relation

$$\eta = \frac{2Th}{\pi \Omega R^4} \, , \tag{6.2}$$

Figure 6.6 – Thermal bath from *LAUDA*.

Figure 6.7 – Rheometer Physica MCR 301 from *Anton Paar*.

where h is the gap between the plates and R is the disk radius. The shear rate at the border of the disk is simply $\dot{\gamma}_R = R\Omega/h$. In the case of a non-Newtonian fluid, a relation similar to the Weissenberg-Rabinowitsch equation (3.19) can be obtained for the parallel plate geometry. The viscosity η_R at the border of the disk is given by (Bird et al., 1987)

$$\eta_R(\dot{\gamma}_R) = \frac{T}{2\pi R^3 \dot{\gamma}_R}\left(3 + \frac{d\ln|T|}{d\ln|\dot{\gamma}_R|}\right) . \tag{6.3}$$

In a parallel plate geometry there is a shear rate gradient in the radial direction. A shear-induced particle migration could be expected towards the center. However, the shear rate gradient is oriented in the vorticity direction, which has a much lower diffusivity coefficient. Besides, Krishnan et al. (1996) proposed that a curvature-induced migration would balance the migration by shear-rate gradient and produce a nearly null net flux. In fact, Chow et al. (1994) experimentally verified that no noticeable concentration gradient is observed even after long time experiments. Therefore, the parallel plate geometry is appropriate to study a homogeneous suspension rheometry.

The rheometer Physica MCR 301 requires only a small amount of fluid sample (≈ 0.2 ml). An uniform magnetic field can be applied by the magneto-rheological device MDR 70/1T from *Anton Paar*. The field is perpendicular to the disks (parallel to the velocity gradient) and can reach values up to 1 Tesla. The rotating disk has a diameter of 20 mm. A thermal bath from *LAUDA* is used to control the fluid temperature and cool the magnetic coil.

6.3 Magnetic fluid samples

The ferrofluid sample used in this work is the fluid APG 1134 manufactured by *FerroTec*. The magnetic particles are made from magnetite and have a mean magnetic diameter of $d_m = 10$ nm and a solid saturation magnetization of $M_d = 440$ kA/m. The properties of the ferrofluid are described in the Table 3. Based on the estimates by Ilg and Odenbach (2009), we assume a ratio between the hydrodynamic and the magnetic diameters of $d_h/d_m = 1.2$. The capillary viscometer requires up to 20 ml of fluid. Since a large volume of ferrofluid was not available, the same sample was recirculated and used for all measurements.

Table 3 – Ferrofluid sample properties. Data provided by the manufacture *FerroTec*.

Product	M_s (kA/m)	ϕ_m	η_ϕ (cP) (27^oC)	ρ (g/ml) (25^oC)	Base fluid
APG 1134	17,5	3,9 %	1000	1,07	Hydrocarbon

Experiments were also conducted for the samples EFH 1 and EFH 3 from *FerroTec*, but these fluids presented poor stability and poor resistance to water and humidity.

6.4 Uncertainty analysis

The experimental results for the viscosity, the shear rate, and the magnetic field are subjected to random and systematic uncertainties. The uncertainty of the applied magnetic field can be calculated applying the Taylor expansion method to the expression 6.1,

$$\delta H_o = \pm\sqrt{|\delta H_{Gau}|^2 + f_e\frac{N_v}{L}|\delta I|^2}\ . \tag{6.4}$$

where δH_{gau} is the Gaussmeter accuracy. The most significant source of error is the electric current uncertainty ($\delta I = \pm 0,02$ A). The uncertainty of the magnetic field is propagated to the global Langevin parameter using the expression,

$$\delta\alpha_o = \pm \left| \frac{\mu_o m}{kT} \delta H_o \right| \ . \tag{6.5}$$

The uncertainty in the wall shear rate can be calculated from the expression (3.19),

$$\delta\dot{\gamma}_w = \dot{\gamma}_w \sqrt{\left(\frac{\delta Q}{Q}\right)^2 + \left(3\frac{\delta d}{d}\right)^2} \ . \tag{6.6}$$

The uncertainty associated with the non-linear correction in equation (3.19) can be neglected. The main source of error is the diameter accuracy, which propagates into an uncertainty of 10 % for the shear rate. However, the diameter accuracy has only a fixed systematic component, since the same capillary is used for all experiments. Therefore, this contribution can be omitted when comparing different results for the capillary viscometer, but must be considered in comparisons with the rotational rheometer. The shear-rate uncertainty propagates to the wall Péclet number with the expression

$$\delta Pe_w = \pm Pe_w \left| \frac{\delta\dot{\gamma}_w}{\dot{\gamma}_w} \right| \ . \tag{6.7}$$

Accordingly to the expression (3.20), the uncertainty of the wall viscosity is influenced by the uncertainty of the pressure reading, the flow rate and the capillary diameter,

$$\delta\eta_w = \pm\eta_w \sqrt{\left|\frac{\delta p}{\Delta p}\right|^2 + \left|\frac{\delta Q}{Q}\right|^2 + \left|4\frac{\delta d}{d}\right|^2} \ . \tag{6.8}$$

Again, the main source of error is the diameter accuracy due to its high value ($\delta d = \pm 3\%\ d$) and the high sensibility generated by the fourth order exponent. The resulting viscosity uncertainty is of 15 %. In order to reduce this value, the results are divided by the measured ordinary suspension viscosity η_ϕ and the same capillary is used for all measurements. In this manner, the systematic error due to the diameter is canceled and the resulting uncertainty is simplified to

$$\delta\left(\frac{\Delta\eta_w}{\eta_\phi}\right) = \pm\frac{\eta_w}{\eta_\phi} \sqrt{\left|\frac{\delta p}{\Delta p}\right|^2 + \left|\frac{\delta Q}{Q}\right|^2} \ . \tag{6.9}$$

6.5 Calibration of the system

In this section, the calibration and verification procedures for the experimental setup are described.

6.5.1 Calibration curve for the magnetic field

The axial magnetic field produced by the solenoids was calibrated using a Gaussmeter with a Hall probe. For each electric current applied to the coils, the magnetic field

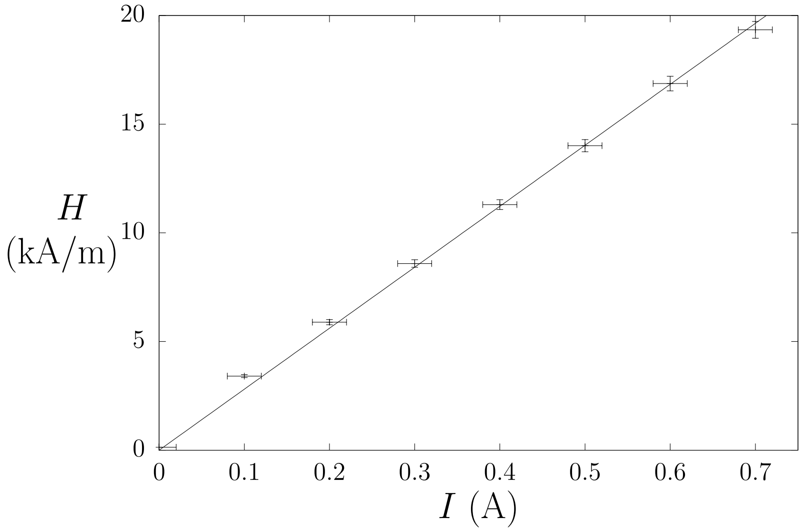

Figure 6.8 – Axial magnetic field produced by the solenoids as a function of the applied electric current.—— Linear regression.

was measured and the data was plotted into the Figure 6.8. Based on the expression (6.1), a linear regression was applied to the data and the correction factor f_e was estimated as 0.75.

6.5.2 Calibration with a stable newtonian fluid

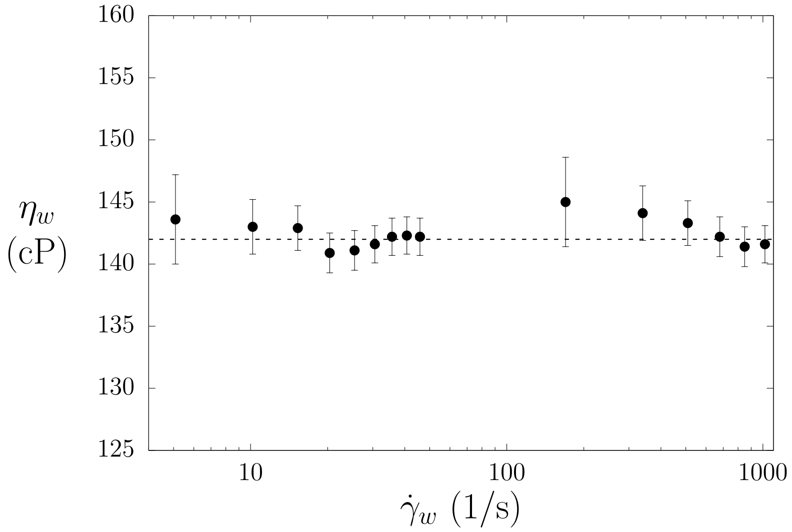

Figure 6.9 – Wall viscosity of mineral oil as a function of the wall shear rate. ● Capillary viscometer, - - - Mean value $\eta = 142$ cP. $T = 25^oC$.

In order to verify the accuracy of the capillary viscometer, the viscosity of a stable Newtonian fluid (mineral oil) was measured as a function of the shear rate. Figure 6.9 shows that all of the viscosity measurements agree with the mean value ($\eta = 142$ cP) within the experimental uncertainty.

6.6 Experimental procedure

The experimental procedure consists of the following steps:

- The thermal bath temperature is set to $T = 25^oC$ and the system equilibrates its temperature for 10 min;
- With no flow imposed, a zero-calibration is performed;
- The syringe pump applies a constant flow rate and the pressure transducer collects the pressure reading every second. The Figure 6.10 presents a typical time evolution of the pressure reading. Due to the system's relaxation, a transient reading is observed. The transient time varies from 1 to 50 min depending on the setup parameters. After the pressure reaches the plateau, the readings are collected for another 10 min and a time average is taken for this region;

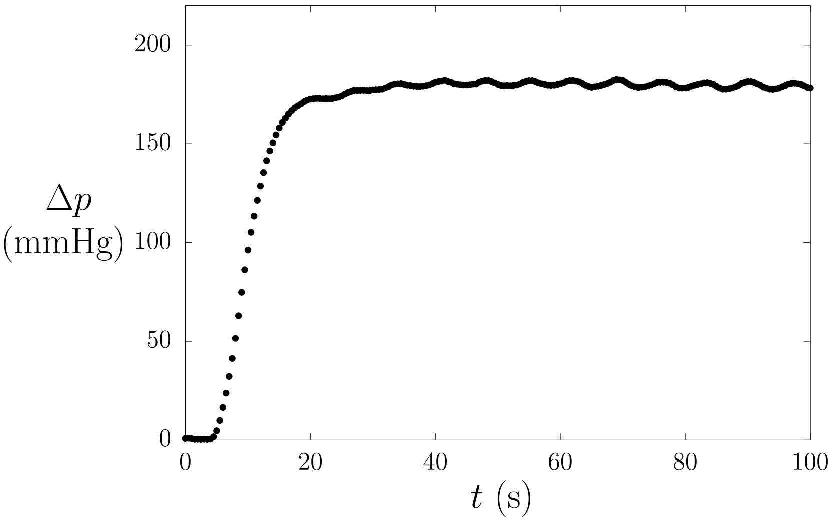

Figure 6.10 – Time evolution of the pressure transducer reading for the fluid EFH 3 with a flow rate of 1000 μl/min and without an applied field.

- The procedure is repeated for different values of flow rate and applied magnetic field;
- The wall shear rate, the relative and the wall viscosity are calculated using the expressions (3.19),(3.15) and (3.20).

7 Experimental Results

In this section, the experimental results for the ferrofluid APG 1134 are presented. The wall viscosity was measured with a capillary viscometer as a function of the global Langevin parameter and the wall Péclet number. The measurements are compared with the numerical results in order to validate the theoretical models. Also, a comparison with the rotational rheometer results is made. The rheometer and the capillary setups differ by the direction of the applied field with respect to the flow. The rheometer experiments were conducted in collaboration with the Ph.D. student Igor D. O. Pereira. The non-dimensional parameters corresponding to the measuring conditions are presented in the table 4. The value obtained for the ordinary suspension viscosity $\eta_\phi(\overline{\phi}_h)$ was 848 cP. Since the carrier fluid viscosity was not available, it was estimated using Einstein's formula, resulting in a value of $\eta_o = 724$ cP. All measurements were carried at a temperature of 25^oC. The low Reynolds number ensures the unidirectionality condition. The dipolar interaction parameter is not sufficiently high to induce significant inter-particle forces. However, if a diameter dispersion is considered, these forces may be strong for a fraction of large particles.

Table 4 – Physical non-dimensional parameters for the experiments.

Parameter	**Definition**	**Values**
Global Langevin parameter	$\alpha_o = \dfrac{4\mu_o \pi a_m^3 M_d H_o}{3kT}$	$0 - 2.4$
Péclet number	$Pe = \dfrac{4\pi\eta_o a_h^3 \dot{\gamma}_c}{kT}$	$10^{-3} - 1$
Mean magnetic volume fraction	$\overline{\phi}_m = \overline{n} v_m$	0.039
Mean hydrodynamic volume fraction	$\overline{\phi}_h = \overline{n} v_h$	0.069
Dipolar interaction parameter	$\lambda = \dfrac{\mu_o \pi a_m^3 M_d^2}{18kT}$	1.3
Langevin initial susceptibility	$\chi_i = 8\phi_m \lambda$	0.4
Reynolds number	$Re_d = \dfrac{\rho U d}{\eta_o}$	$0 - 0.03$

7.1 Verification of the stability of the ferrofluid

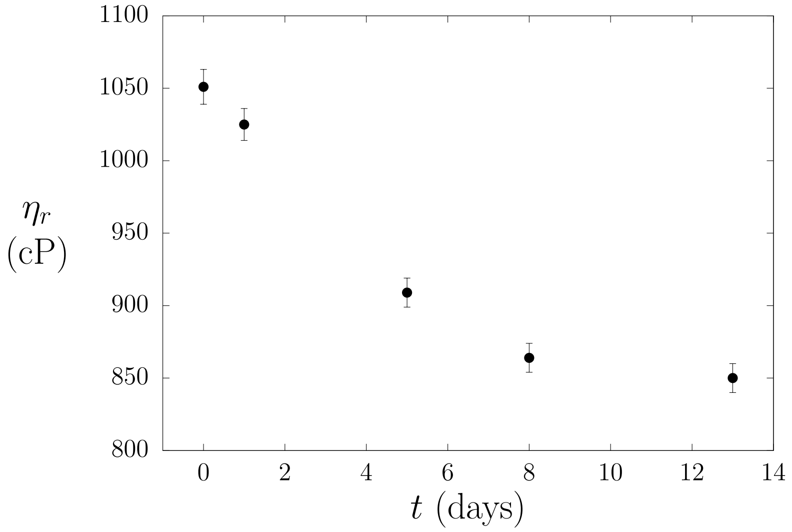

Figure 7.1 – Relative viscosity of the ferrofluid APG 1134 as a function of the days after the first measure.● Capillary viscometer, $Pe = 0.013$,$\alpha_o = 0$.

A test was conducted to verify the stability of the ferrofluid under long periods of shear. Within a single measurement time (up to 1 hour), the sample did not present a viscosity variation. However, in a time window of some days, the sample's viscosity decreased significantly after many measurements. This thixotropic behavior is probably a consequence of the break-up of structures due to the shear. Figure 7.1 presents the relative viscosity for the same sample at a fixed shear rate measured on different days. This data does not correspond to a single continuous measurement, but rather different measurements conducted on successive days. Also, due to the viscometer configuration, each fluid portion is not in a constant shear, but rather circulates between the capillary tube (shearing region) and the reservoir (rest region) throughout the experiment.

After about 13 days, the viscosity variation was within the experimental uncertainty. To avoid the thixotropic effects, the measurements used in this work were taken after this period.

7.2 Newtonian behavior in the absence of field

The wall viscosity of the fluid APG 1134 was measured for various values of the wall Péclet number and without an applied field. The results were compared with the measurements for the rheometer. Although both experimental setups have a small uncertainty for the relative variations of the viscosity, its absolute value has a large systematic uncertainty due to the high sensibility to the geometric parameters (the capillary diameter d and the rheometer disk radius R). Since only the viscosity variations are relevant in this work, the ordinary suspension viscosity $\eta_\phi(\overline{\phi}_h)$ in the limit of low Pe was assumed to be equal for both setups.

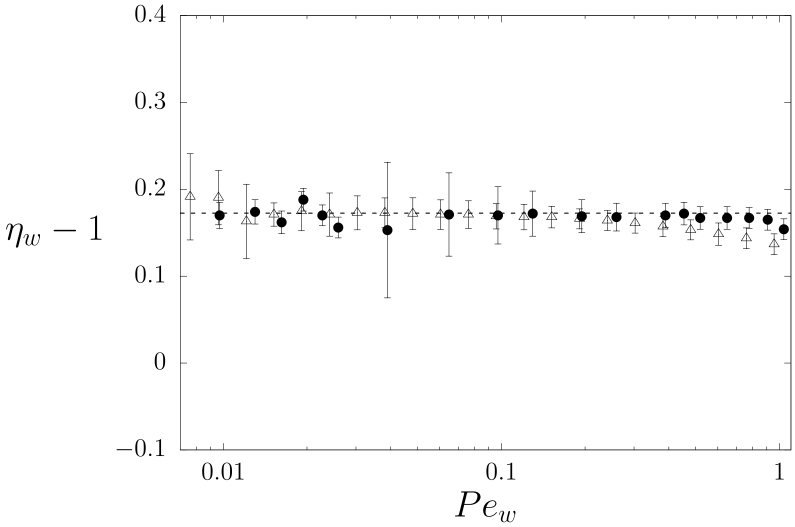

Figure 7.2 – Wall viscosity increase as a function of the wall Péclet number for the ferrofluid APG 1134. - - - Newtonian plateau, ● Capillary viscometer, △ Rotational rheometer. $\alpha_o = 0$.

A typical ferrofluid presents a Newtonian behavior in the absence of field. Figure 7.2 shows that the viscosity is independent of the shear rate for most of the Péclet range. For higher values Péclet number ($> 0,5$), a small shear-thinning effect is observed in both experimental setups. This viscosity reduction is probably due to the commercial additive present in the APG 1134. The viscosities measured by both experimental setups agree within the experimental uncertainty, indicating that no significant hydrodynamic dispersion can be observed for this Péclet number range and in the absence of an applied field.

7.3 Comparison between the capillary viscometer and the rotational rheometer

The capillary viscometer and the rotational rheometer were used to measure the magnetoviscous effect for various values of the global Langevin parameter and the wall Péclet number. The viscosity results are presented as the magnetic increment $\Delta\eta_m$, *i.e.*, the non-dimensional wall viscosity subtracted by the viscosity in the absence of field and for the same shear rate ($\Delta\eta_m(\alpha_o, Pe_w) = \eta(\alpha_o, Pe_w) - \eta(0, Pe_w)$).

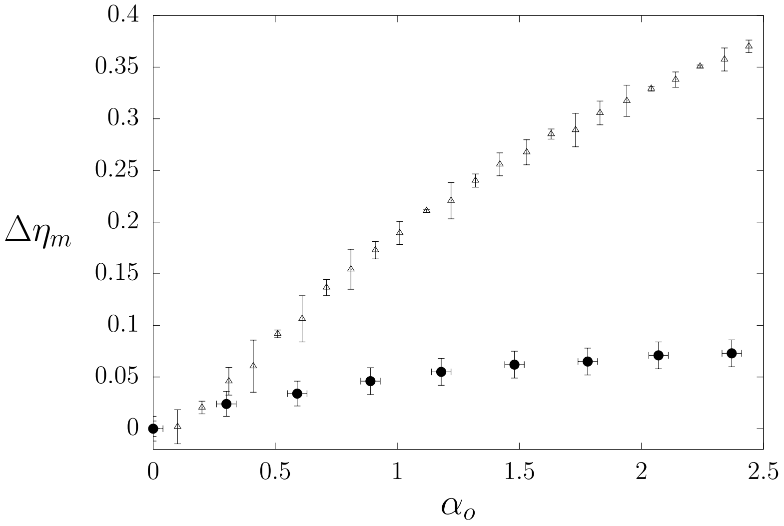

(a) $Pe_w = 0.026$

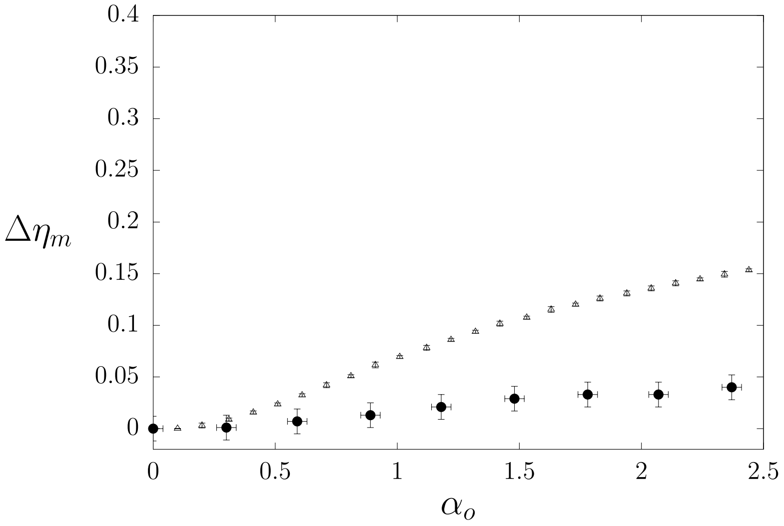

(b) $Pe_w = 0.91$

Figure 7.3 – Magnetic increment of the wall viscosity as a function of the global Langevin parameter. ● Capillary viscometer, △ Rotational rheometer.

The capillary viscometer and the rotational rheometer differ in the direction of the applied field (parallel to the velocity and the velocity gradient, respectively) and in the direction of the gradient of shear (parallel to velocity gradient and the vorticity, respectively). Figures 7.3 and 7.4 present the magnetic increment of the wall viscosity as a function of the global Langevin parameter and wall Péclet number, respectively. Although the qualitative behavior was similar, the magnetic increments measured by the rheometer were about 5 times larger than the respective values obtained by the capillary setup. The largest difference is observed for a strong field and a weak flow. The numerical results presented in the chapter 5 indicate that the shear-induced dispersion is weak at small Péclet numbers (For $Pe = 0.1$, the viscosity reduction is of order 10^{-3}). In this regime, the Brownian diffusion produces a nearly uniform concentration profile, even for very anisotropic or rough particles. Therefore, the difference between the experimental setups cannot be due to the hydrodynamic dispersion and must be a consequence of the applied field direction. An applied magnetic field parallel to the velocity gradient results in a much larger magnetoviscous effect. This anisotropic response is typical for prolate particles or chain-like aggregates (Ilg and Odenbach, 2009). The nominal dipolar interaction parameter $\lambda = 1.3$ is not large enough to allow for significant inter-particle forces. However, a large diameter dispersion would lead to a considerable fraction of particles to have a large diameter and therefore a large value of λ. These particles would be able to form chain aggregates and produce this anisotropic behavior. The experimental work from Odenbach and Raj (2000) previously investigated the effects of a diameter dispersion on the magnetoviscous effect.

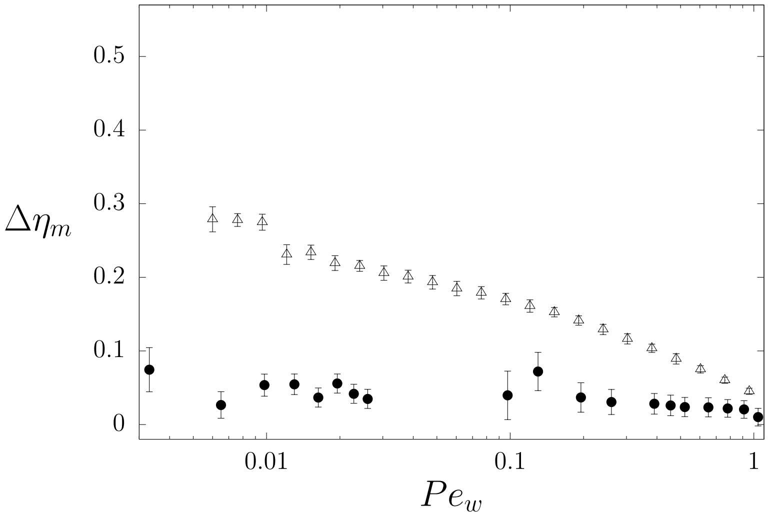

(a) $\alpha_o = 1.18$

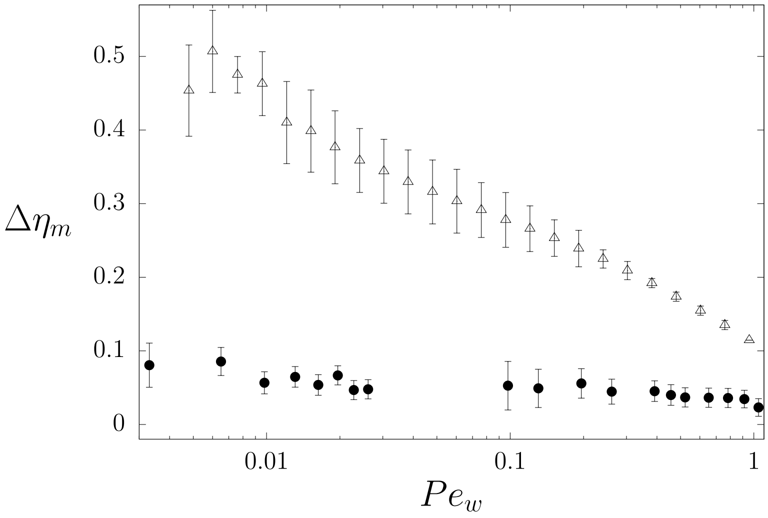

(b) $\alpha_o = 2.37$

Figure 7.4 – Magnetic increment of the wall viscosity as a function of the wall Péclet number. ● Capillary viscometer, △ Rotational rheometer.

A strong shear-thinning behavior is observed in Figure 7.4 for both experimental setups. The results are more evident for the rheometer measurements, for which the magnetic increments are larger. A similar result was also observed in the work of Pereira

(2019) for rotational rheometer measurements. The author sustained that the ferrofluid's viscosity obeyed a modified Hershel-Buckley law, with an infinite viscosity plateau. The numerical models presented in the chapter 5 do predict a shear-thinning effect. However, the viscosity reduction is only significant for high Péclet number ($Pe > 1$), which is not the case for the experimental results in this work. Particle simulations from Rosa and Cunha (2019, 2020) verified a large shear-thinning effect at low-moderate Péclet numbers due to the break-up of chains. This numerical results are in consonance with the experimental data in Figure 7.4. A theoretical model of a maximum chain length for a given shear rate was discussed by Zubarev and Iskakova (1995), Ilg and Hess (2003) and Odenbach and Thurm (2002).

7.4 Comparison between the experimental and numerical results

The capillary viscometer measurements were compared with the numerical results of the theoretical models adopted in this work. For the Péclet number range used in the experiment (Pe up to 1), the theoretical models do not predict a significant shear-thinning effect neither due to the shear-induced migration neither due to the dominance of the hydrodynamic torque over the magnetic torque. In this regime, the viscosity is mainly a function of the global Langevin parameter α_o and the aspect ratio β in the case of smooth spheroidal particles, and a function only of α_o for rough spherical particles. Therefore, it is sufficient to compare the experimental measurements with the numerical predictions for smooth spheroidal particles, since the rough spherical particles model corresponds to the case of $\beta = 1$.

In the Figure 7.5, the magnetic increment of the relative viscosity is presented as a function of α_o for various values of Pe. The viscosity increases with the field intensity and is higher for smaller Péclet numbers. Using only the aspect ratio β as the fitting parameter, the numerical results were compared with the experimental data. A very good agreement is observed for most Péclet numbers. For a small Péclet number, a large value of β was obtained (for $Pe = 0.013$, $\beta = 1.55$), while for a moderate Péclet number, a value of β close to the spherical shape presented a better agreement (for $Pe = 0.91$, $\beta = 1.05$). The chain-aggregates formed in suspension could be interpreted as an equivalent spheroidal particle. A larger value of β indicates that the chains are longer or that a greater fraction of the total particles forms aggregates. The decrease in the value of β with an increase of Pe suggests that there is an aggregate break-up induced by shear.

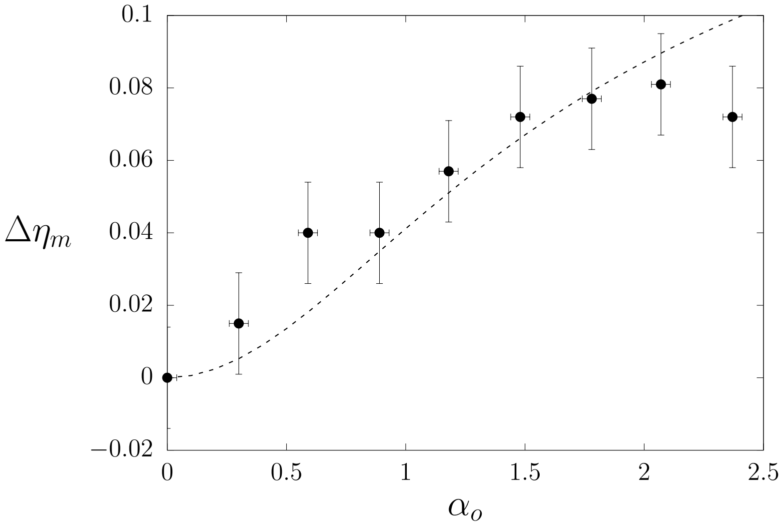

(a) $Pe = 0.013$, $\beta = 1.55$

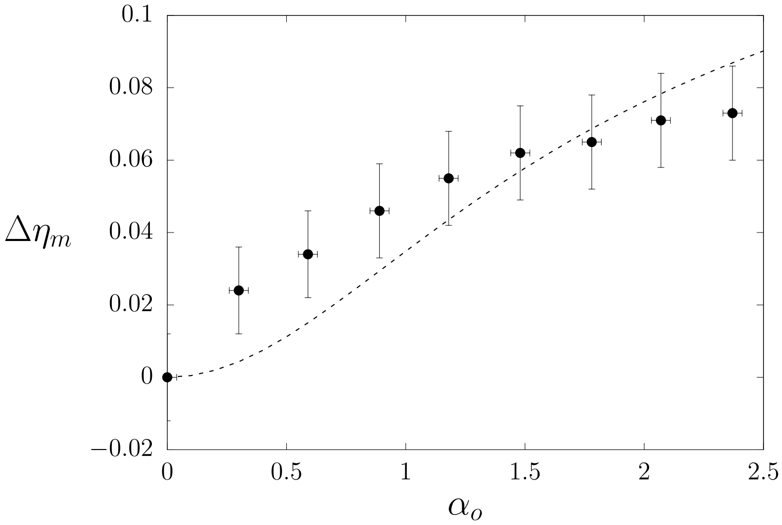

(b) $Pe = 0.026$, $\beta = 1.45$

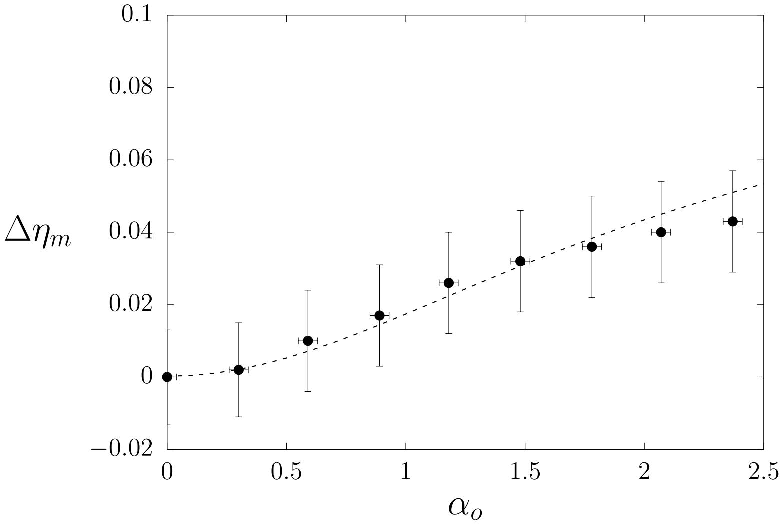

(c) $Pe = 0.45$, $\beta = 1.10$

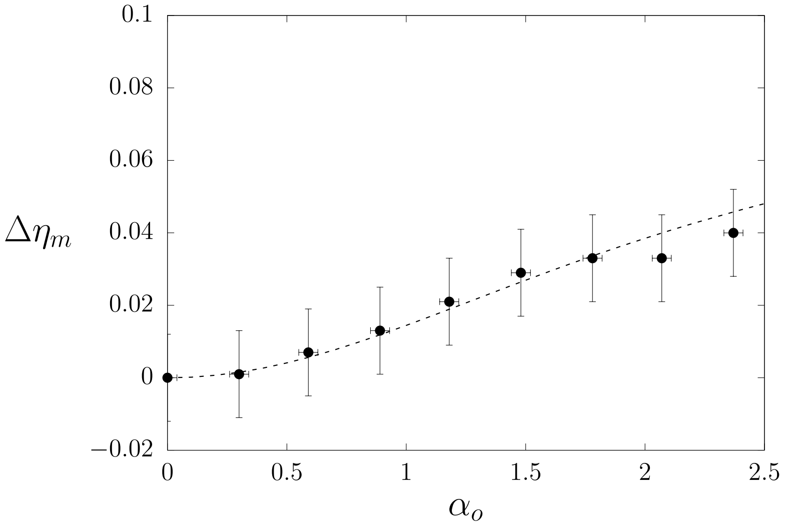

(d) $Pe = 0.91$, $\beta = 1.05$

Figure 7.5 – Magnetic increment of the relative viscosity as a function of the global Langevin parameter. - - - Numerical results for smooth spheroidal particles, ● Capillary viscometer.

The experimental data for the capillary viscometer indicates a shear-thinning behavior of the ferrofluid in the presence of a field, as shown in the Figure 7.6. The theoretical model for smooth spheroidal particles can not predict the experimental data for a single value of β. For moderate Péclet number (close to 1), the results agree with the limiting case of spherical particles ($\beta = 1$). However, for small Pe, the measured viscosities are higher than the numerical predictions, suggesting that particle chains are formed in weak flows.

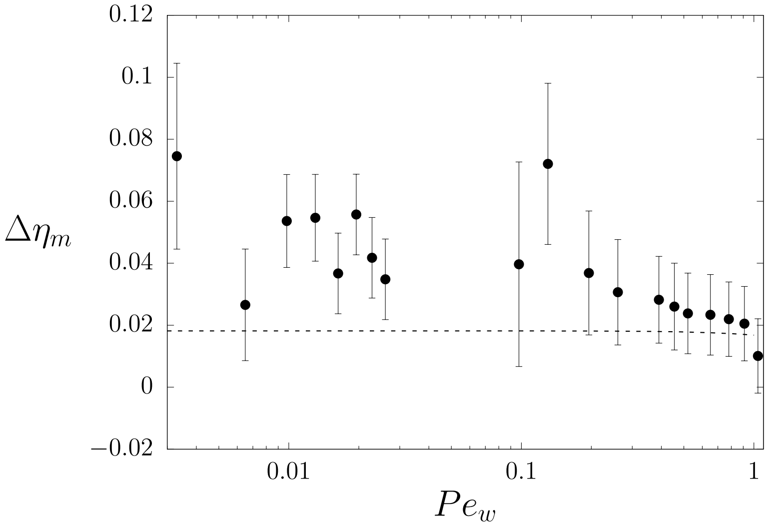

(a) $\alpha_o = 1.18$

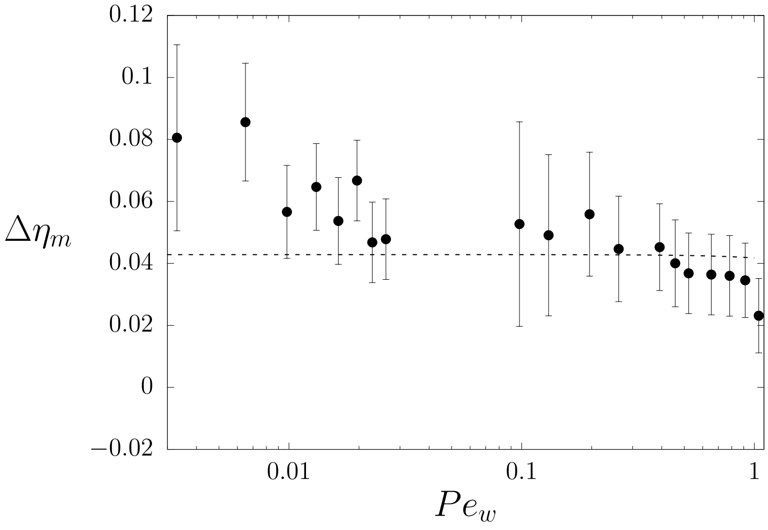

(b) $\alpha_o = 2.37$

Figure 7.6 – Magnetic increment of the wall viscosity as a function of the wall Péclet number.- - - Numerical results for smooth spherical particles ($\beta = 1$), ● Capillary viscometer.

8 Final Considerations

The present work performed a theoretical and experimental investigation of the flow of a dilute ferrofluid in a capillary tube. The focus of the study was on the influence of a shear-induced dispersion on the rheological response of the magnetic suspension under the action of a longitudinal applied magnetic field. The shear-induced dispersion was assumed to be originated on the particle's rugosity or non-sphericity, and the diffusivity coefficients were estimated with the correlations of Cunha and Hinch (1996). The *stresslet* and the magnetization relaxation equations for spheroidal particles were obtained, respectively, from the model of Kröger and Sellers (1995) and a modified model of Shliomis (2001). The theoretical models were solved numerically with an integration routine in the radial domain. Asymptotic solutions were obtained in the limits of low and high Péclet numbers. The experimental measurements were performed in a capillary viscometer setup and a rotating parallel-disks rheometer.

The main conclusions indicated by the numerical results are the following:

- The main non-dimensional physical parameters were identified to be the Péclet number and the global Langevin parameter, which are non-dimensional measures of the shear rate and the applied field, respectively;
- The one-dimensional governing system of equations was successfully solved with a numerical routine and the magnetization profile, the volume fraction profile, the relative viscosity, and the wall viscosity were computed for various values of the parameters;
- Asymptotic solutions in the limits of a low or a high Péclet number in the absence of hydrodynamic dispersion, or in the limit a low Péclet number with hydrodynamic dispersion, validate the numerical routine;
- The ferrofluid presents an increase in the viscosity (magneto-viscous effect) with the application of a magnetic field and a strong shear-thinning response with the increase of the shear intensity;
- The shear-induced dispersion is mainly influenced by the diffusivity coefficient and the Péclet number. At weak flows, the Brownian motion dominates and produces a homogeneous concentration profile. For strong flows, the dispersive fluxes by

concentration gradient and by shear rate gradient prevail and balance each other. The latter flux produces a particle migration towards the center of the tube. The global effect is a reduction in the viscosity of the suspension. The dispersive flux by viscosity gradient was found to be very weak in the dilute regime;

- For a suspension of rough spherical particles, the down-gradient diffusivity coefficient and the global Langevin parameter were found to have nearly uncorrelated effects on the rheological response of the fluid. The change in the suspension viscosity was approximately a superposition of the effects from the hydrodynamic dispersion and the applied field;

- For a suspension of smooth spheroidal particles, the aspect ratio affected both the volume fraction profile and the torque balance on the particles. According to the shear rate intensity, different behaviors were observed. At small Péclet numbers, the hydrodynamic dispersion is small and the magnetic torque dominates over the hydrodynamic torque. The increase in the non-sphericity produces a higher viscous dissipation. At large Péclet numbers, the magnetic torque can not balance the hydrodynamic torque and the magnetoviscous effect is small. The non-sphericity induces a large segregation of particles towards the center and the global result is a viscosity reduction with the aspect ratio. The critical Péclet number associated with the transition was computed. It was found the critical Péclet number increases with the global Langevin parameter and decreases with the mean volume fraction. Finally, the suspension of spheroidal particles presented a non-null normal stress difference, indicating the anisotropic and non-linear rheological response of the fluid.

The main conclusions indicated by the experimental data are the following:

- The commercial ferrofluid APG 1134 presented a thixotropic behavior for its ordinary viscosity after many experiments. This effect is not associated with an applied field and is probably a consequence of an irreversible break-up of structures due to shear;

- The experimental measurements for the capillary viscometer and the rotational rheometer indicated that the ferrofluid viscosity increases with the field intensity and decreased with the shear rate. Although the qualitative behavior was similar, the rotational rheometer obtained a magnetic increment about 5 times larger than the capillary setup. Therefore, the applied magnetic field orientation relative to the flow plays an important role in the rheological response of a ferrofluid;

- A strong shear-thinning effect was observed even for moderate Péclet numbers. The theoretical models can not predict this behavior, since the hydrodynamic torque on the particles would only overcome the magnetic torque for high Pe. The break-up of chain-like aggregates is a possible cause for the shear-thinning effect;

- The theoretical model for smooth spheroidal particles can successfully predict the magnetoviscous effect measured by the capillary viscometer if the aspect ratio β is used as a fitting parameter for each Péclet number;
- The experimental measurements conducted in this work were not conclusive for the influence of shear-induced dispersion in quadratic flows. The difference in the applied field direction imposes a limitation to the comparison of the two experimental setups used. Possible pairs of viscometers that could overcome this limitation are the following: a concentric cylinders and a capillary viscometers, both with an applied field parallel to the velocity, or, a parallel disks rheometer and a Hele-Shaw cell viscometer, both with an applied field parallel to the velocity gradient. Also, the high Péclet numbers required for the shear-induced dispersion to overcome the Brownian diffusion are difficult to obtain for magnetic particles with 10 nm of diameter. However, particles designed for magnetic drug delivery have typically a hydrodynamic diameter of $100 - 200$ nm. A Péclet number of 10 could easily be achieved in this case. Also, since the magnetic phase is only a fraction of the composition of the particles, the magnetic interparticle forces would not be very strong.

Finally, we make some suggestions for future works:

- Perform experiments with a ferrofluid composed of particles with a diameter of a few hundreds of nanometers;
- Investigate the viscous response of a suspension of magnetic spheroids using direct particle simulations to compute the orientation distributions;
- Investigate the capillary flow of a ferrofluid with a hydrodynamic dispersion originated in the dipole-dipole forces between particles;
- Investigate the effects of a hydrodynamic dispersion on a model for semi-dilute and concentrated ferrofluids;
- Investigate the effects of a hydrodynamic dispersion in capillary flow of a magneto-rheological fluid (micron-sized particles);
- Compare the viscous response of a ferrofluid in simple and quadratic flows using a pair of experimental setups with the same applied field orientation (*e.g.*, a concentric cylinders and a capillary viscometers, both with an applied field parallel to the velocity, or, a parallel disks rheometer and a Hele-Shaw cell viscometer, both with an applied field parallel to the velocity gradient).

Bibliography

Acrivos, A., G. Batchelor, E. Hinch, D. Koch, and R. Mauri
1992. Longitudinal shear-induced diffusion of spheres in a dilute suspension. *Journal of Fluid Mechanics*, 240:651–657. Quoted on page 5.

Al-Jamal, K. T., J. Bai, J. T.-W. Wang, A. Protti, P. Southern, L. Bogart, H. Heidari, X. Li, A. Cakebread, D. Asker, et al.
2016. Magnetic drug targeting: preclinical in vivo studies, mathematical modeling, and extrapolation to humans. *Nano Letters*, 16(9):5652–5660. Quoted on page 1.

Alexiou, C., R. J. Schmid, R. Jurgons, M. Kremer, G. Wanner, C. Bergemann, E. Huenges, T. Nawroth, W. Arnold, and F. G. Parak
2006. Targeting cancer cells: magnetic nanoparticles as drug carriers. *European Biophysics Journal*, 35(5):446–450. Quoted on page 1.

Alvariño, P. F., J. S. Jabardo, J. P. Agras, and J. G. Del Valle
2015. Self-diffusion assessment in laminar developed flow of nanofluids in microchannels. *International Journal of Thermal Sciences*, 98:113–123. Quoted on page 5.

Aris, R.
2012. *Vectors, Tensors and the Basic Equations of Fluid Mechanics*, Dover Books on Mathematics. Dover Publications. Quoted 2 times on pages 7 and 8.

Bacri, J.-C., R. Perzynski, M. I. Shliomis, and G. I. Burde
1995. “negative-viscosity” effect in a magnetic fluid. *Physical Review Letters*, 75(11):2128. Quoted 2 times on pages 3 and 4.

Bae, D. H., W. J. Han, C. Y. Gao, Y. Z. Dong, and H. J. Choi
2018. Preparation and magnetorheological response of triangular-shaped single-crystalline magnetite particle-based magnetic fluid. *IEEE Transactions on Magnetics*, 54(11):1–4. Quoted on page 24.

Barnes, H. A., J. F. Hutton, and K. Walters
1989. *An introduction to rheology*, volume 3. Elsevier. Quoted on page 26.

Barthès-Biesel, D.
2012. *Microhydrodynamics and complex fluids.* CRC Press. Quoted 2 times on pages 18 and 19.

Biemfohr, S., T. Looby, S. Biemfohr, and D. Leighton

1993. Measurement of the shear-induced coefficient of self-diffusion in dilute suspensions. In *Flow of Particulates and Fluids: Proceedings, Joint DOE/NSF Workshop on Flow of Particulates and Fluids*, Pp. 207–232. Quoted on page 24.

Bird, R. B., R. C. Armstrong, and O. Hassager

1987. *Dynamics of polymeric liquids. Vol. 1: Fluid mechanics.* New York, NY: John Wiley and Sons Inc. Quoted 2 times on pages 29 and 68.

Bossis, G., S. Lacis, A. Meunier, and O. Volkova

2002. Magnetorheological fluids. *Journal of Magnetism and Magnetic Materials*, 252:224–228. Quoted on page 1.

Brady, J. F. and G. Bossis

1988. Stokesian dynamics. *Annual Review of Fluid Mechanics*, 20(1):111–157. Quoted 2 times on pages 16 and 21.

Breedveld, V. and A. J. Levine

2003. Shear-induced diffusion in dilute suspensions of charged colloids. *Soft Materials*, 1(2):235–244. Quoted on page 4.

Brenner, H. and D. W. Condiff

1974. Transport mechanics in systems of orientable particles. iv. convective transport. *Journal of Colloid and Interface Science*, 47(1):199–264. Quoted 2 times on pages 19 and 96.

Butter, K., P. H. Bomans, P. M. Frederik, G. J. Vroege, and A. Philipse

2003. Direct observation of dipolar chains in ferrofluids in zero field using cryogenic electron microscopy. *Journal of Physics: Condensed Matter*, 15(15):S1451. Quoted on page 24.

Charles, S. W.

2002. The preparation of magnetic fluids. In *Ferrofluids*, Pp. 3–18. Springer. Quoted on page 24.

Chow, A. W., S. W. Sinton, J. H. Iwamiya, and T. S. Stephens

1994. Shear-induced particle migration in couette and parallel-plate viscometers: Nmr imaging and stress measurements. *Physics of Fluids*, 6(8):2561–2576. Quoted on page 69.

Cunha, F. R.

2012. Fundamentos da hidrodinâmica de fluidos magnéticos. In *Turbulência*, B. S. Carmo, G. R. S. Assi, J. R. Meneghini, J. A. P. Aranha, and E. V. Volpe, eds., volume 8, chapter 7, Pp. 257–339. São Paulo: ABCM. Quoted 3 times on pages 2, 9, and 13.

Cunha, F. R. and E. J. Hinch

1996. Shear-induced dispersion in a dilute suspension of rough spheres. *Journal of Fluid Mechanics*, 309:211–223. Quoted 8 times on pages 4, 5, 22, 23, 24, 56, 57, and 82.

Cunha, F. R. and Y. D. Sobral

2004. Characterization of the physical parameters in a process of magnetic separation and pressure-driven flow of a magnetic fluid. *Physica A: Statistical Mechanics and its Applications*, 343:36–64. Quoted on page 2.

Cunha, L. H. P., I. R. Siqueira, F. R. Cunha, and T. F. Oliveira

2020. Effects of external magnetic fields on the rheology and magnetization of dilute emulsions of ferrofluid droplets in shear flows. *Physics of Fluids*, 32(7):073306. Quoted on page 4.

De Vicente, J., D. J. Klingenberg, and R. Hidalgo-Alvarez

2011. Magnetorheological fluids: a review. *Soft Matter*, 7(8):3701–3710. Quoted on page 1.

Drazer, G., J. Koplik, B. Khusid, and A. Acrivos

2002. Deterministic and stochastic behaviour of non-brownian spheres in sheared suspensions. *Journal of Fluid Mechanics*, 460:307–335. Quoted on page 4.

Eckstein, E. C., D. G. Bailey, and A. H. Shapiro

1977. Self-diffusion of particles in shear flow of a suspension. *Journal of Fluid Mechanics*, 79(1):191–208. Quoted 2 times on pages 4 and 5.

Felderhof, B. U.

2000. Magnetoviscosity and relaxation in ferrofluids. *Physical Review E*, 62(3):3848. Quoted 2 times on pages 3 and 17.

Gitter, K. and S. Odenbach

2011. Experimental investigations on a branched tube model in magnetic drug targeting. *Journal of Magnetism and Magnetic Materials*, 323(10):1413–1416. Quoted on page 1.

Gontijo, R. G., S. Malvar, Y. D. Sobral, and F. R. Cunha

2016. The influence of a magnetic field on the mechanical behavior of a fluid interface. *Meccanica*, Pp. 1–19. Quoted on page 2.

Grant, I. S. and W. R. Phillips

2013. *Electromagnetism.* John Wiley & Sons. Quoted on page 9.

Hinch, E. J.

1991. *Perturbation methods.* Cambridge university press. Quoted on page 43.

Hudson, S. D.

2003. Wall migration and shear-induced diffusion of fluid droplets in emulsions. *Physics of fluids*, 15(5):1106–1113. Quoted on page 4.

Ilg, P., E. Coquelle, and S. Hess
2006. Structure and rheology of ferrofluids: simulation results and kinetic models. *Journal of Physics: Condensed Matter*, 18(38):S2757. Quoted on page 4.

Ilg, P. and S. Hess
2003. Nonequilibrium dynamics and magnetoviscosity of moderately concentrated magnetic liquids: a dynamic mean-field study. *Zeitschrift für Naturforschung A*, 58(11):589–600. Quoted 2 times on pages 3 and 78.

Ilg, P. and M. Kröger
2002. Magnetization dynamics, rheology, and an effective description of ferromagnetic units in dilute suspension. *Physical Review E*, 66(2):021501. Quoted 3 times on pages 4, 18, and 96.

Ilg, P. and S. Odenbach
2009. Ferrofluid structure and rheology. In *Colloidal Magnetic Fluids*, Pp. 1–77. Springer. Quoted 2 times on pages 69 and 77.

Jeffery, G. B.
1922. The motion of ellipsoidal particles immersed in a viscous fluid. *Proceedings of the Royal Society of London. Series A, Containing papers of a mathematical and physical character*, 102(715):161–179. Quoted on page 18.

Kim, J. M., S. G. Lee, and C. Kim
2008. Numerical simulations of particle migration in suspension flows: Frame-invariant formulation of curvature-induced migration. *Journal of Non-Newtonian Fluid Mechanics*, 150(2-3):162–176. Quoted on page 5.

Klokkenburg, M., B. H. Erné, J. D. Meeldijk, A. Wiedenmann, A. V. Petukhov, R. P. Dullens, and A. P. Philipse
2006. In situ imaging of field-induced hexagonal columns in magnetite ferrofluids. *Physical Review Letters*, 97(18):185702. Quoted 3 times on pages x, 24, and 25.

Koh, C. J., P. Hookham, and L. G. Leal
1994. An experimental investigation of concentrated suspension flows in a rectangular channel. *Journal of Fluid Mechanics*, 266:1–32. Quoted on page 5.

Krishnan, G. P., S. Beimfohr, and D. T. Leighton
1996. Shear-induced radial segregation in bidisperse suspensions. *Journal of Fluid Mechanics*, 321:371–393. Quoted 3 times on pages 5, 23, and 68.

Kröger, M. and H. S. Sellers
1995. Viscosity coefficients for anisotropic, nematic fluids based on structural theories of suspensions. *The Journal of Chemical Physics*, 103(2):807–817. Quoted 3 times on pages 19, 82, and 96.

Lac, E. and D. Barthès-Biesel

2008. Pairwise interaction of capsules in simple shear flow: Three-dimensional effects. *Physics of Fluids*, 20(4):040801. Quoted on page 4.

Leighton, D. and A. Acrivos

1987a. Measurement of shear-induced self-diffusion in concentrated suspensions of spheres. *Journal of Fluid Mechanics*, 177:109–131. Quoted 3 times on pages 4, 5, and 24.

Leighton, D. and A. Acrivos

1987b. The shear-induced migration of particles in concentrated suspensions. *Journal of Fluid Mechanics*, 181:415–439. Quoted 2 times on pages 4 and 22.

Lopez, M. and M. D. Graham

2007. Shear-induced diffusion in dilute suspensions of spherical or nonspherical particles: Effects of irreversibility and symmetry breaking. *Physics of Fluids*, 19(7):073602. Quoted on page 4.

Lübbe, A. S., C. Alexiou, and C. Bergemann

2001. Clinical applications of magnetic drug targeting. *Journal of Surgical Research*, 95(2):200–206. Quoted on page 1.

Martsenyuk, M. A., Y. L. Raikher, and M. I. Shliomis

1973. On the kinetics of magnetization of suspensions of ferromagnetic particles. *Zh. Eksp. Teor. Fiz*, 65:834–841. Quoted 5 times on pages 3, 4, 17, 18, and 20.

McTague, J. P.

1969. Magnetoviscosity of magnetic colloids. *The Journal of Chemical Physics*, 51(1):133–136. Quoted on page 2.

Müller, H. W. and M. Liu

2002. Ferrofluid dynamics. In *Ferrofluids*, Pp. 112–123. Springer. Quoted on page 17.

Odenbach, S.

2009. *Colloidal magnetic fluids: basics, development and application of ferrofluids*, volume 763. Springer. Quoted 3 times on pages 1, 2, and 4.

Odenbach, S. and K. Raj

2000. The influence of large particles and agglomerates on the magnetoviscous effect in ferrofluids. *Magnetohydrodynamics*, 36(4):312–319. Quoted 2 times on pages 3 and 77.

Odenbach, S., T. Rylewicz, and H. Rath

1999. Investigation of the weissenberg effect in suspensions of magnetic nanoparticles. *Physics of Fluids*, 11(10):2901–2905. Quoted 2 times on pages 4 and 63.

Odenbach, S. and S. Thurm

2002. Magnetoviscous effects in ferrofluids. In *Ferrofluids*, Pp. 185–201. Springer. Quoted on page 78.

Patel, R., R. V. Upadhyay, and R. V. Mehta

2003. Viscosity measurements of a ferrofluid: comparison with various hydrodynamic equations. *Journal of Colloid and Interface Science*, 263(2):661–664. Quoted on page 3.

Pereira, I. D. O.

2019. Rheology of ferrofluids in shear flows. Master's thesis, Department of Mechanical Engineering, University of Brasilia. Quoted 2 times on pages 63 and 77.

Phillips, R. J., R. C. Armstrong, R. A. Brown, A. L. Graham, and J. R. Abbott

1992. A constitutive equation for concentrated suspensions that accounts for shear-induced particle migration. *Physics of Fluids A: Fluid Dynamics*, 4(1):30–40. Quoted 5 times on pages 5, 22, 23, 24, and 48.

Raj, K. and R. Moskowitz

1990. Commercial applications of ferrofluids. *Journal of Magnetism and Magnetic Materials*, 85(1-3):233–245. Quoted on page 1.

Rinaldi, C., A. Chaves, S. Elborai, X. T. He, and M. Zahn

2005. Magnetic fluid rheology and flows. *Current Opinion in Colloid & Interface Science*, 10(3-4):141–157. Quoted 3 times on pages 1, 2, and 16.

Rosa, A. P., G. C. Abade, and F. R. Cunha

2017. Computer simulations of equilibrium magnetization and microstructure in magnetic fluids. *Physics of Fluids*, 29(9):092006. Quoted on page 4.

Rosa, A. P. and F. R. Cunha

2019. The influence of dipolar particle interactions on the magnetization and the rotational viscosity of ferrofluids. *Physics of Fluids*, 31(5):052006. Quoted 2 times on pages 4 and 78.

Rosa, A. P. and F. R. Cunha

2020. Shear rate dependence of viscosity and normal stress differences in ferrofluids. *Journal of Magnetism and Magnetic Materials*, 499:166184. Quoted 2 times on pages 4 and 78.

Rosa, A. P., R. G. Gontijo, and F. R. Cunha

2016. Laminar pipe flow with drag reduction induced by a magnetic field gradient. *Applied Mathematical Modelling*, 40(5-6):3907–3918. Quoted on page 2.

Rosensweig, R. E.

2013. *Ferrohydrodynamics*. Courier Corporation. Quoted 3 times on pages 2, 10, and 14.

Roure, G. A. and F. R. Cunha

2018. Hydrodynamic dispersion and aggregation induced by shear in non-brownian magnetic suspensions. *Physics of Fluids*, 30(12):122002. Quoted 3 times on pages 4, 5, and 24.

Russel, W. B., W. Russel, D. A. Saville, and W. R. Schowalter

1991. *Colloidal dispersions.* Cambridge university press. Quoted on page 22.

Schumacher, K. R., I. Sellien, G. S. Knoke, T. Cader, and B. A. Finlayson

2003. Experiment and simulation of laminar and turbulent ferrofluid pipe flow in an oscillating magnetic field. *Physical Review E*, 67(2):026308. Quoted on page 3.

Schwartz, M.

1972. *Principles of Electrodynamics.* New York: Dover. Quoted 2 times on pages 11 and 13.

Shliomis, M. I.

1971. Effective viscosity of magnetic suspensions. *Zh. Eksp. Teor. Fiz*, 61:2411–2418. Quoted 4 times on pages 3, 15, 17, and 44.

Shliomis, M. I.

2001. Ferrohydrodynamics: Testing a third magnetization equation. *Physical Review E*, 64(6):060501. Quoted 4 times on pages 3, 17, 20, and 82.

Sinzato, Y. Z. and F. R. Cunha

2020. Modeling and experiments of capillary flow of non-symmetric magnetic fluids under uniform field. *Journal of Magnetism and Magnetic Materials*, Pp. 166–867. Quoted 2 times on pages 42 and 43.

Subramanian, G. and J. F. Brady

2006. Trajectory analysis for non-brownian inertial suspensions in simple shear flow. *Journal of Fluid Mechanics*, 559:151–203. Quoted on page 4.

Truesdell, C. A.

1992. *A first course in rational continuum mechanics*, volume 1. Academic Press. Quoted on page 12.

Wang, Y., R. Mauri, and A. Acrivos

1998. Transverse shear-induced gradient diffusion in a dilute suspension of spheres. *Journal of Fluid Mechanics*, 357:279–287. Quoted on page 4.

Zahn, M.

2001. Magnetic fluid and nanoparticle applications to nanotechnology. *Journal of Nanoparticle Research*, 3(1):73–78. Quoted on page 1.

Zarraga, I. E. and D. T. Leighton Jr
2002. Measurement of an unexpectedly large shear-induced self-diffusivity in a dilute suspension of spheres. *Physics of Fluids*, 14(7):2194–2201. Quoted 3 times on pages 5, 22, and 24.

Zubarev, A. Y. and L. Y. Iskakova
1995. On the theory of physical properties of magnetic fluids with chainy aggregates. *Zhurnal Ehksperimental'noj i Teoreticheskoj Fiziki*, 107(5):1534–1551. Quoted 2 times on pages 4 and 78.

Appendixes

A Low Péclet number asymptotic solutions in the presence of hydrodynamic dispersion

Simplified governing equations:

$$\begin{cases} Gr - 16(1+2.5\phi_h)\dot{\gamma} - 8\dfrac{\phi_h\alpha_o^2}{Pe}\dfrac{\chi_o}{\chi_i}H_{er}(1+\chi_e H_{ez}) = 0 \\ \dot{\gamma}H_{ez} - \dfrac{2}{Pe}(1+\chi_o)H_{er} - \dfrac{\alpha_o^2}{3Pe}\dfrac{\chi_o}{\chi_i}H_{er}H_{ez}(1+\chi_o H_{ez}) = 0 \\ \dot{\gamma}H_{er} - \dfrac{2}{Pe}(1-H_{ez}) - \dfrac{\alpha_o^2}{3Pe}\dfrac{\chi_o}{\chi_i}H_{er}^2(1+\chi_o H_{ez}) = 0 \\ \left(\dfrac{2}{3Pe} + K_c\phi_h 2r\right)\dfrac{d\phi_h}{dr} + 2\phi_h^2 K_c = 0 \ , \\ \dfrac{du}{dr} = -8\dot{\gamma} \ . \end{cases} \tag{A.1}$$

Polynomial expansion:

$$\begin{cases} G = G_0 + PeG_1 + Pe^2G_2\mathcal{O}(Pe^3) \ , \\ u = u_0 + Peu_1 + Pe^2u_2 + \mathcal{O}(Pe^3) \ , \\ \dot{\gamma} = \dot{\gamma}_0 + Pe\dot{\gamma}_1 + Pe^2\dot{\gamma}_2\mathcal{O}(Pe^3) \ , \\ \tilde{H}_{er} = \tilde{H}_{er0} + Pe\tilde{H}_{er1} + Pe^2\tilde{H}_{er2}\mathcal{O}(Pe^3) \ , \\ H_{ez} = H_{ez0} + PeH_{ez1} + Pe^2H_{ez2}\mathcal{O}(Pe^3) \ . \end{cases} \tag{A.2}$$

where $\tilde{H}_{er} = H_{er}/Pe$.

Equilibrium solution:

$$\begin{cases} G_0 = 32(1+2.5\overline{\phi}_h) + \dfrac{3}{2}\overline{\phi}_h\dfrac{\alpha_o^2\chi_o}{6\chi_i + \alpha_o^2\chi_o} \\ \dot{\gamma}_0(r) = 2r \\ \phi_{h0}(r) = \overline{\phi}_h \\ \tilde{H}_{er0}(r) = \dfrac{6\chi_i}{(1+\chi_o)(6\chi_i + \alpha_o^2\chi_o)}r \\ H_{ez0}(r) = 1 \end{cases} \tag{A.3}$$

Correction order Pe:

$$\begin{cases} G_1 = -\dfrac{K_c\overline{\phi}_h}{5}(G_0 - 32) \\ \dot{\gamma}_1(r) = -K_c\overline{\phi}_h\dfrac{G_0 - 32}{G_0}\left(\dfrac{12r}{5} - 6r^2\right) \\ \phi_{h1}(r) = K_c\overline{\phi}_h^2(1 - 3r) \\ \tilde{H}_{er1}(r) = \dfrac{\dot{\gamma}_1(r)}{(1+\chi_o)}\dfrac{3\chi_i}{(6\chi_i + \alpha_o^2\chi_o)}r \\ H_{ez1}(r) = 0 \end{cases} \tag{A.4}$$

Correction order Pe^2:

$$\begin{cases} G_2 = -\dfrac{3}{50}\dfrac{[K_c\overline{\phi}_h(G_0 - 32)]^2}{G_0} - \dfrac{4}{3}\overline{\phi}_h\alpha_o^2\dfrac{\chi_o}{\chi_i}\left(\dfrac{6\chi_i}{6\chi_i + \alpha_o^2\chi_o}\right)^4\dfrac{1 + 2\chi_o}{(1+\chi_o)^2} \\ \phi_{h2}(r) = -3K_c^2\overline{\phi}_h^3\left(2r - \dfrac{9r^2}{2} - \dfrac{5}{384}\right) \\ \dot{\gamma}_2(r) = \dfrac{2G_2}{G_0}r - \dfrac{\dot{\gamma}_1\phi_{h1}}{\overline{\phi}_h}\dfrac{G_0 - 32}{G_0} - \dfrac{\dot{\gamma}_0\phi_{h2}}{\overline{\phi}_h}\dfrac{G_0 - 32}{G_0} - \dfrac{8r^3}{3G_0}\overline{\phi}_h\alpha_o^2\dfrac{\chi_o}{\chi_i}\left(\dfrac{6\chi_i}{6\chi_i + \alpha_o^2\chi_o}\right)^4\dfrac{1 + 2\chi_o}{(1+\chi_o)^2} \\ \tilde{H}_{er2}(r) = \dfrac{\dot{\gamma}_2(r)}{(1+\chi_o)}\dfrac{3\chi_i}{(6\chi_i + \alpha_o^2\chi_o)}r + \dfrac{(6\chi_i)^3(6\chi_i(1+\chi_o) - \alpha_o^2\chi_o^2)}{(1+\chi_o)^2(6\chi_i + \alpha_o^2\chi_o)^4}r^3 \\ H_{ez2}(r) = -\dfrac{36\chi_i^2}{(1+\chi_o)(6\chi_i + \alpha_o^2\chi_o)^2}r^2 \end{cases} \tag{A.5}$$

B Geometric and order functions for ellipsoidal particles

B.1 Geometric functions

Consider the ellipsoid aspect ratio as β. The geometric functions ψ_i are given by (Brenner and Condiff, 1974; Ilg and Kröger, 2002)

$$\begin{cases} \psi_0(\beta) = \dfrac{2(\beta^2+1)^2}{3\beta^2(2\beta^2\nu - \nu - 1)} \ , \\ \psi_1(\beta) = \dfrac{8(\beta^2-1)^2}{5\beta^2(3\nu + 2\beta^2 - 5)} \ , \\ \psi_2(\beta) = \psi_1(\beta)\left[\dfrac{[\beta^2(\nu+1)-2](3\nu+2\beta^2-5)}{4[\nu(2\beta^2-1)-1](\beta^2+2-3\beta^2\nu)} - 1\right] \ , \\ \psi_3(\beta) = -\psi_1(\beta)\left[1 - \dfrac{2\beta^2+1-(4\beta^2-1)\nu}{4(2\beta^2+1)\nu - 12}\right] - 2\psi_2(\beta) \ , \\ \psi_4(\beta) = \dfrac{2(\beta^2-1)^2}{5\beta^2(2\beta^2\nu - \nu - 1)} \ , \end{cases} \tag{B.1}$$

where ν is given by

$$\nu = \frac{\cosh^{-1}(\beta)}{\beta\sqrt{\beta^2-1}} \tag{B.2}$$

B.2 Orientation moments

Consider the unit vector $\hat{\boldsymbol{n}} = \boldsymbol{m}/m$ as the orientation of the particle's magnetic dipole and $\hat{\boldsymbol{e}}_M = \boldsymbol{M}/M = \boldsymbol{H}_e/H_e$ as the orientation of the magnetization. The orientation moments (or orientation tensors) are given by (Kröger and Sellers, 1995; Ilg and Kröger, 2002),

$$\begin{cases} \langle n_i \rangle = \mathcal{L}_1 \hat{e}_{Mi} \ , \\ \langle n_i n_j \rangle = \dfrac{\mathcal{L}_2 \langle n_i \rangle \langle n_j \rangle}{\mathcal{L}_1^2} + \dfrac{1-\mathcal{L}_2}{3} \delta_{ij} \ , \\ \langle n_i n_j n_k n_l \rangle = \dfrac{\mathcal{L}_4 \langle n_i \rangle \langle n_j \rangle \langle n_k \rangle \langle n_l \rangle}{\mathcal{L}_1^4} + \dfrac{7 - 10\mathcal{L}_2 + 3\mathcal{L}_4}{105} (\delta_{ij}\delta_{kl} + \delta_{ik}\delta_{jl} + \delta_{il}\delta_{jk}) + \\ \dfrac{\mathcal{L}_2 - \mathcal{L}_4}{7\mathcal{L}_1^2} (\delta_{ij} \langle n_k \rangle \langle n_l \rangle + \delta_{ik} \langle n_j \rangle \langle n_l \rangle + \delta_{kj} \langle n_i \rangle \langle n_l \rangle + \delta_{il} \langle n_j \rangle \langle n_k \rangle + \delta_{jl} \langle n_i \rangle \langle n_k \rangle + \delta_{kl} \langle n_i \rangle \langle n_j \rangle) \ , \end{cases} \tag{B.3}$$

where $\mathcal{L}_i$ are high order Langevin functions given by: $\mathcal{L}_0 = 1$, $\mathcal{L}_1 = \coth(\alpha_e) + 1/\alpha_e$ and, for $i \geq 2$, $\mathcal{L}_i = \mathcal{L}_{i-2} - (2i-1)\mathcal{L}_{i-1}/\alpha_e$.

C Objectivity of the constitutive models

In accordance to the principle of material frame-indifference, the constitutive models be given by objective quantities, *i. e.* that obey the transformation rule (2.38). In this appendix, the objectivity of the magnetization equation (2.67) is demonstrated. Firstly, some useful relations are presented. Consider the following reference change,

$$x'_i = c_i + Q_{ik}(x_k - x_{ok}) \ , \tag{C.1}$$

where $\boldsymbol{c}$ is a time-dependent vector, $\boldsymbol{x}_o$ is the initial position, and $\boldsymbol{Q}$ is a time-dependent orthogonal second-order tensor. The following relations can be derived for the velocity $\boldsymbol{u}$ and the velocity gradient $\nabla\boldsymbol{u}$,

$$u'_i = Q_{ik}u_k + \dot{c}_i + \dot{Q}_{ik}(x_k - x_{ok}) \ , \tag{C.2}$$

and

$$(\nabla'\boldsymbol{u}')_{ij} = \frac{\partial u'_j}{\partial x'_i} = Q_{ik}\frac{\partial u_l}{\partial x_k}Q_{lj} + Q_{ik}\dot{Q}_{jk} \ . \tag{C.3}$$

From the velocity gradient, the referential transformations for the deformation rate and rotation tensor, $\boldsymbol{E}$ and $\boldsymbol{W}$, can be calculated as follows,

$$E'_{ij} = \frac{1}{2}\left[\frac{\partial u'_j}{\partial x'_i} + \frac{\partial u'_i}{\partial x'_j}\right] = \frac{1}{2}\left[Q_{ik}\left(\frac{\partial u_l}{\partial x_k} + \frac{\partial u_k}{\partial x_l}\right)Q_{lj} + Q_{ik}\dot{Q}_{jk} + \dot{Q}_{ik}Q_{jk}\right] \ , \tag{C.4}$$

and

$$W'_{ij} = \frac{1}{2}\left[\frac{\partial u'_j}{\partial x'_i} - \frac{\partial u'_i}{\partial x'_j}\right] = \frac{1}{2}\left[Q_{ik}\left(\frac{\partial u_l}{\partial x_k} - \frac{\partial u_k}{\partial x_l}\right)Q_{lj} + Q_{ik}\dot{Q}_{jk} - \dot{Q}_{ik}Q_{jk}\right] \ . \tag{C.5}$$

Applying the identity $(\dot{Q_{ik}Q_{jk}}) = Q_{ik}\dot{Q}_{jk} + \dot{Q}_{ik}Q_{jk} = 0$, the relations can be simplified to

$$E'_{ij} = \frac{1}{2}\left[Q_{ik}\left(\frac{\partial u_l}{\partial x_k} + \frac{\partial u_k}{\partial x_l}\right)Q_{lj}\right] = Q_{ik}E_{kl}Q_{jl} \ , \tag{C.6}$$

and

$$W'_{ij} = \frac{1}{2}\left[Q_{ik}\left(\frac{\partial u_l}{\partial x_k} - \frac{\partial u_k}{\partial x_l}\right)Q_{lj} + 2Q_{ik}\dot{Q}_{jk}\right] = Q_{ik}W_{kl}Q_{jl} + Q_{ik}\dot{Q}_{jk} \ . \tag{C.7}$$

Comparing these relations to the material frame-indifference principle 2.38, it can be concluded that the deformation rate tensor $\boldsymbol{E}$ is objective while the rotation tensor $\boldsymbol{W}$ is not.

C.1 Magnetization relaxation equation

In this section, we demonstrate the objectivity of the magnetization relation equation (2.67). Firstly, it is more convenient to rewrite this equation using the dual relation, $\boldsymbol{\xi} \times \boldsymbol{M} = -2\boldsymbol{W} \cdot \boldsymbol{M}$,

$$\frac{D\boldsymbol{M}}{Dt} = -\boldsymbol{W} \cdot \boldsymbol{M} - \frac{\mu_o}{6\eta_o \phi_h} \boldsymbol{M} \times (\boldsymbol{M} \times \boldsymbol{H}) + \frac{1}{\tau} (\boldsymbol{M}_o - \boldsymbol{M}) \ , \tag{C.8}$$

We rewrite the equation in the transformed reference frame using Einstein's notation,

$$\frac{DM'_i}{Dt'} = -W'_{ik} M'_k - \frac{\mu_o}{6\eta_o \phi'_h} M'_k (H'_k M'_i - M'_k H'_i) + \frac{1}{\tau'} (M'_{oi} - M'_i) \ , \tag{C.9}$$

The local and equilibrium magnetizations, and the magnetic field are assumed to be objective quantities, as well as the volume fraction and the relaxation time. The material derivative is invariant to a reference transformation. Rewriting in terms of the non-transformed quantities results that

$$\begin{aligned}\frac{D}{Dt}(Q_{il} M_l) &= -(Q_{im} W_{ml} Q_{kl} + Q_{im} \dot{Q}_{km}) Q_{kn} M_n \\ &\quad - \frac{\mu_o}{6\eta_o \phi_h} Q_{km} M_m (Q_{kn} H_n Q_{il} M_l - Q_{in} H_n Q_{kl} M_l) + \frac{Q_{il}}{\tau} (M_{ol} - M_l) \ . \end{aligned}\tag{C.10}$$

Further simplifying the expression results that,

$$\begin{aligned} Q_{il} \frac{DM_l}{Dt} &= Q_{il} \left(-W_{lk} M_k - \frac{\mu_o}{6\eta_o \phi_h} M_k (H_k M_l - M_k H_l) + \frac{1}{\tau} (M_{ol} - M_l) \right) \\ &\quad - [\dot{Q}_{il} + Q_{im} Q_{kl} \dot{Q}_{km}] M_l \ . \end{aligned}\tag{C.11}$$

Notice that $\dot{Q}_{il} + Q_{im} Q_{kl} \dot{Q}_{km} = \dot{Q}_{il} - Q_{im} Q_{km} \dot{Q}_{kl} = \dot{Q}_{il} - \delta_{ik} \dot{Q}_{kl} = \dot{Q}_{il} - \dot{Q}_{il} = 0$. Finally, the result is

$$Q_{il} \frac{DM_l}{Dt} = Q_{il} \left(-W_{lk} M_k - \frac{\mu_o}{6\eta_o \phi_h} M_k (H_k M_l - M_k H_l) + \frac{1}{\tau} (M_{ol} - M_l) \right) \ . \tag{C.12}$$

We conclude that all of the terms from the magnetization relaxation equation are objective quantities. The objectivity of the equations (2.70) and (2.72) can be demonstrated in a similar manner.